V.V. Bogoroskii (Ed.)

The Physics of ICE

Trudy
Vol. 295

V.V. Bogorodskii, Editor

THE PHYSICS OF ICE

(Fizika l'da)

Translated from Russian

Translated by IPST staff

Table of Contents

EDITOR'S PREFACE

The present volume is a collection of the most significant reports read at the Symposium on Ice Physics which was held at the Arctic and Antarctic Scientific Research Institute in June 1968.

The reports can be classified in two main groups. The first group deals with the measurements of the electromagnetic properties and parameters of various types of ice, including description of the measurement techniques applied under field and laboratory conditions. This group also covers reports on radar probing and sounding of Arctic glaciers, in particular the glaciers of the Severnaya Zemlya Archipelago. Because of the marked differences in the temperature conditions between Arctic and Antarctic glaciers, the radar methods orginally developed for the conditions of the Antarctica had to be revised before they could be applied to Arctic ice. Experimental and theoretical determinations of the temperature of the daytime surface of glaciers using thermosensitive IR detectors, radiation thermometers, and centimeter radiometers also fall under this category. The entire cycle of radiophysical measurements led to the development of new powerful and flexible methods of studying the properties of ice and measuring ice thickness. Appropriate technical tools are now available for radiophysical glaciology, including radar units for ice thickness measurements, radiation thermometers, and radiometers.

The second group encompasses research work done on the mechanical properties of ice, using a variety of acoustic methods. This category includes theoretical, methodological, and experimental studies. Reports with a definite theoretical bias are those by D. B. Dianov, V. P. Gavrilo, A. V. Gusev, and A. E. Kolesnikov and also by A. V. Prokof'eva. Other reports mainly deal with the experiments carried out under field and laboratory conditions.

Both the radiophysical and the acoustical direction open wide new horizons for glaciologists and oceanographers. The simultaneous growth and application of these disciplines yields highly valuable and mutually complementary results on the physical characteristics of ice. There are also future plans for the application of other electrophysical methods of research.

All critical comments and suggestions from the readers will be most welcome.

Two Russian acronyms are used throughout this book:

AANII stands for Arkticheskii i Antarkticheskii Nauchno-Issledovatel'skii Institut—The Arctic and Antarctic Scientific-Research Institute, the sponsoring organization of the present collection.

SP stands for Severnyi Polyus—North Pole—a Soviet designation adopted for various drifting polar stations in the Arctic Ocean.

V. V. Bogorodskii and B. A. Fedorov

RADAR PROBING OF SEVERNAYA ZEMLYA GLACIERS

Systematic radar studies of Arctic glaciers were carried out in 1963 by glaciologists from Great Britain and the USA. These studies were largely made possible by the earlier results of A. Waite and S. Schmidt /1/, who had analyzed the errors of radar altimeters and presented some results of radar probing of a Greenland glacier with a SCR-718 altimeter in 1959 — 1960. The first airborne radar measurements of ice thickness in the Arctic (Ellesmere Island) were carried out by a British team /2/; a group from USA carried out radar probing of a Greenland glacier in the same year /3/.

In 1963 — 1964, Soviet scientists launched a systematic project of radar measurements of the Antarctic ice near Mirnyi. Since then, all the Soviet antarctic expeditions have been working on this project. This is partly due to the excellent equipment available to the Antarctic expeditions, and also to the fact that each Soviet expedition to the Antarctic invariably includes scientists of a wide spectrum of specializations. Consequently, there was no difficulty in organizing frequent radar measurements under a variety of conditions, including comparison of radar probing findings with seismic and well logging data. The technique of airborne radar measurements was perfected to a considerable degree on these expeditions.

An opportunity for radar probing of glaciers in the Soviet Arctic first presented itself in 1968. The SEVER-20 Arctic Expedition which operated in September — October 1968 included an airborne radiophysical team engaged on various applications of radiophysical methods for hydrometeorological measurements. One of the authors of the present paper participated in the work of this team; his task was to develop a technique of airborne radar probing of glaciers under the specific Arctic conditions.

The technical procedure for airborne radar probing of Antarctic surface glaciers was described in detail in /4/. Two principal aims were pursued: measurements of the continental ice thickness (which, in combination with barometric levelling, made it possible to chart the bedrock topography) and measurements of the attenuation of radar signals under a variety of glacio-logical and temperature conditions. Measurements of the thickness of outlet glaciers and shelf ice in the Antarctic have largely remained sporadic, without any definite program and aim. The published technique therefore applies to ice thickness measurements and determination of the continental subglacial topography in the following general cases: 1) very extended ice areas without any clear markers; 2) very thick ice and low temperatures, especially far from the coastal area. The first of these two conditions is highly unfavorable for identifying aircraft position, and the second condition leads to heavy requirements from the radar equipment for probing to

1

maximum depth. Airborne radar probing techniques in the Antarctic have thus been applied on a small scale only.

The glaciers in the Arctic are substantially smaller, with numerous markers in the periglacial zone; there is thus no difficulty of position identification in airbrone surveys. Moreover, the glaciers are relatively thin (thickness not exceeding 1000 m), so that fairly unsophisticated short-pulse equipment will ensure adequate accuracy in measuring the propagation time of the radar signal in the glacier. The regional glaciological conditions and the meteorological features of the various test areas in the Arctic should be carefully selected in relation to the particular time of year (absence of thawed water in the surface layer of the glaciers ensures a longer range of radar probing, other conditions being equal; low-altitude flying is relatively safe in sunny weather, with minimum wind). Moreover, maximum cooperation between the flying crew and the scientific team is absolutely essential. For these reasons, the airborne probing at this stage was of tentative experimental nature. Because of limited runs and difficult meteorological conditions, not all the typical glaciers in the test area were studied with the same thoroughness.

The measurements were carried out for the glaciers of the following islands in the Severnaya Zemlya Archipelago: Shmidt, Komsomolets, Pioner, Oktyabrskaya Revolyutsiya. The glacier on the Ushakov Isl. in the Kara Sea, to the northwest of the Severnaya Zemlya Archipelago, was also included in the survey (see Figure 1).

A radar transmitter with the following parameters was used:

frequency $f = 100\,\text{MHz}$;

pulse power $P_p = 5 - 7$ watt;

pulse length $\tau = 0.3\,\mu\text{sec}$;

receiver sensitivity $P_r = 5 \cdot 10^{-15}$ watt.

A radar unit with similar parameters proved quite successfull in the Antarctic: it probed to depths of over 1000 m, gave reliable measurements of a "wet" giant iceberg of 250 − 300 m thickness and outlet glaciers up to 400 − 500 m thick from an aircraft. Since we did not expect glaciers thicker than 400 m in the Arctic, a radar station of this kind was considered quite suitable.

Separate receiving and transmitting antennas were used; the antennas were mounted on the fuselage of the LI-2 aircraft, at a distance of about 2 m from each other. This arrangement was not quite satisfactory: direct "leakage" of the signal between the two antennas increased the blind area of the radar, but it did not affect the results of thickness measurements appreciably. The aircraft altitude above the glacier surface was measured with the same radar, since the LI-2 is not equipped with an alternative radio altimeter. Barometric measurements fixed the relative position of the air—ice, air—rock, and ice—rock interfaces in relation to the sea level: a VD-10 barometric aircraft altimeter was used to this end.

The radar screen was photographed with ARFA-51 camera.

Since the methodological results are of strictly particular interest, they are not considered here in detail. We should only note that the best time of the year for radar surveys is apparently spring (March, April, and early May); the sunny weather is highly suitable for low-altitude flights above the glaciers, whereas the thawing is not pronounced in the glaciers of this region in March and April and the absorption of electromagnetic energy in ice is still relatively low.

Shmidt Glacier

Akademiya
Nauk
Glacier

Pioner
glacier

Rusanov
glacier

Al'banov
glacier

N
S

Ushakov
glacier

b
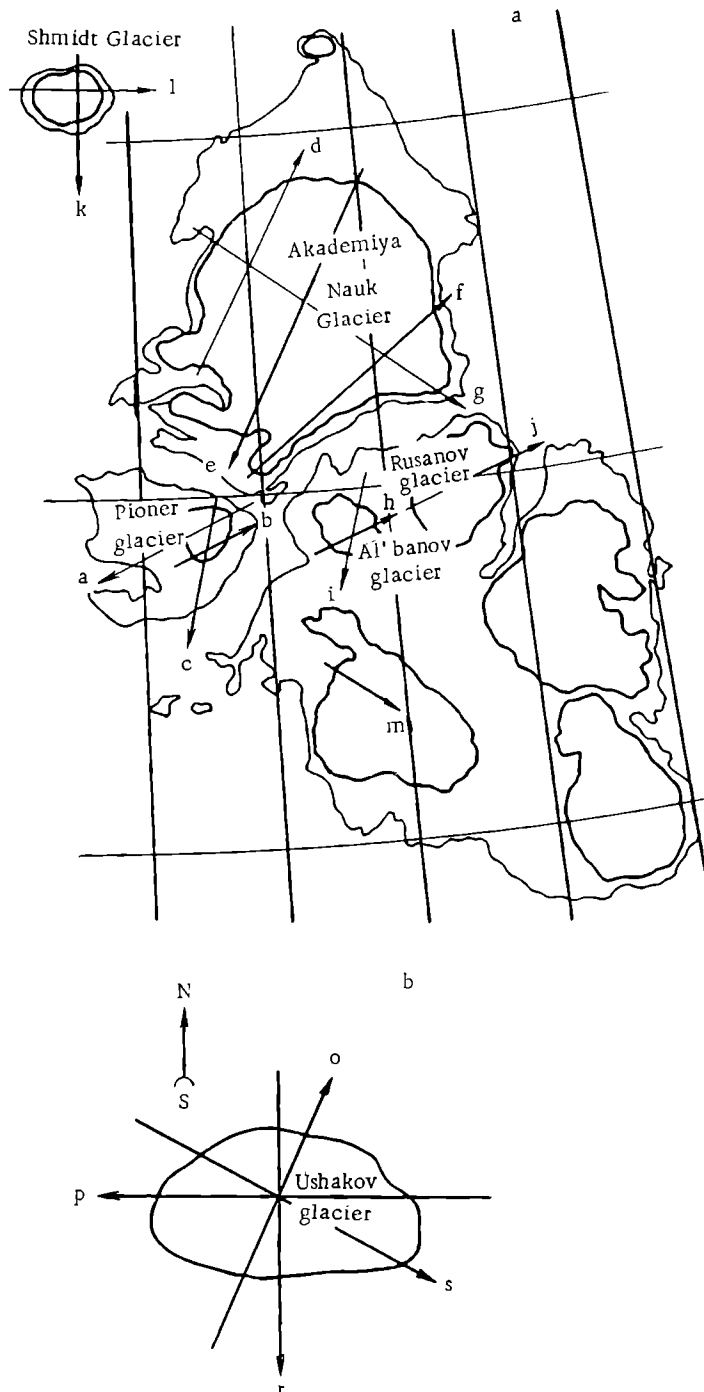
FIGURE 1. A map of the test area:

a) flight routes over Pioner, Akademiya Nauk, Al'banov, Rusanov,
Shmidt, and Vavilov glaciers, for which the glacier sections have
been constructed; b) flight routes over the Ushakov glacier.

3

The results of ice thickness measurements (in meters) are listed in Table 1. The same tables gives the number of the measurement point; the measurement time (minutes, seconds) along each route;* flight altitude according to the barometric altimeter, in meters; flight height above the glacier surface according to radar data, in meters; notes to each table specify the flight velocity in each case. These results are highly tentative, since lack of photogrammetic data prevented exact identification of the flight route positions in relation to the local topography and the barometric readings were not taken quite simultaneously with the photographic recording of the radar pulses. Moreover, the flight velocity is not constant over a given route because of the effect of glacier winds.** Nevertheless, these results provide some indication of the subglacial topography and characterize the position of the bedrock (relative to the sea level) with an error which is roughly estimated as being between -7 and $+3\%$ of the glacier thickness.

Measurements of the attenuation of radar signals show that the losses of electromagnetic energy in the glacier due to absorption did not exceed at the relevant time the corresponding absorption losses for a continental Antarctic glacier in the coastal zone (within $10-15$ km off the coast).

In calculating the ice thickness, we used a figure of $167 \, \text{m}/\mu\text{sec}$ for the propagation velocity of electromagnetic waves in ice /4/. Once the electrical parameters of ice become known with sufficient accuracy, the results of thickness measurements can be improved.

Bibliography

1. W a i t e, A. H. Ice Depth Soundings with Ultra-High Frequency Radio Waves in the Arctic and Antarctic; and Some Observed Over-Ice Altimeter Errors. — Fort Monmouth, N. J., U. S. Army Signal Research and Development Laboratory. 1960.
2. E v a n s, S. and G. R o b i n.— Nature, 210, No. 5039. 1966.
3. E v a n s, S.— The Polar Record, 13, No. 85. 1967.
4. B o g o r o d s k i i, V. V. Fizicheskie metody issledovaniya lednikov (Physical Methods of Studying Glaciers).— Leningrad, Gidrometeoizdat. 1968.

---

* The measurements along route a did not begin at the glacier edge. The identification of the flight route was based on the highest point of the glacier surface.
** For this reason the table gives the measurement time, and not the distance. Since the flight velocity is variable (the table gives the two velocity readings with the aircraft entering and leaving the glacier), the time-to-distance conversion is obviously inaccurate.

TABLE 1.

Measurement number	Time, hrs min	Flight altitude from barometric altimeter, m	Flight altitude according to radar, m	Ice thickness, m
Pioner glacier, 9 October 1968, route a				
1	0 00	480	305	—
2	0 15	—	290	—
3	0 30	—	275	—
4	0 45	—	265	230
5	1 00	660	265	274
6	1 15	—	270	295
7	1 30	—	270	322
8	1 45	—	260	338
9	2 00	700	275	344
10	2 15	—	285	327
11	2 30	—	295	294
12	2 45	—	290	249
13	3 00	520	290	190
14	3 15	480	335	112

Note. Initial flight velocity 200 km/hr. Terminal flight velocity 220 km/hr.

		Pioner glacier, 9 October 1968, route b		
1	0 00	—	315	92
2	0 15	—	300	145
3	0 30	—	290	196
4	0 45	600	290	235
5	1 00	—	300	268
6	1 15	—	305	305
7	1 30	715	295	327
8	1 45	710	275	333
9	2 00	—	275	327
10	2 15	—	280	319
11	2 30	—	285	299
12	2 45	665	300	268
13	3 00	—	315	230
14	3 15	—	300	190
15	3 30	—	300	148
16	3 45	510	310	106
17	4 00	—	315	56
18	4 15	—	310	30
19	4 30	—	295	30
20	4 45	360	320	—

Note. Initial flight velocity 200 km/hr. Terminal flight velocity 220 km/hr. Flight altitude from barometric altimeter read 15 sec before the beginning of measurements was 420 m.

5

TABLE 1 (continued)

Measurement number	Time, hrs min	Flight altitude from barometric altimeter, m	Flight altitude according to radar, m	Ice thickness, m

Pioner glacier, 9 October 1968, route c

Measurement number	Time, hrs min	Flight altitude from barometric altimeter, m	Flight altitude according to radar, m	Ice thickness, m
1	0 00	350	315	14
2	0 15	—	325	31
3	0 30	—	310	56
4	0 45	—	300	90
5	1 00	465	285	126
6	1 15	—	280	157
7	1 30	—	300	193
8	1 45	—	295	227
9	2 00	615	300	246
10	2 15	—	285	260
11	2 30	—	280	277
12	2 45	—	270	286
13	3 00	650	290	286
14	3 15	—	275	275
15	3 30	—	285	246
16	3 45	—	280	202
17	4 00	525	295	129
18	4 15	430	330	39

Note. Initial flight velocity 180 km/hr. Terminal flight velocity 200 km/hr.

Akademiya Nauk glacier, 9 October 1968, route d

Measurement number	Time, hrs min	Flight altitude from barometric altimeter, m	Flight altitude according to radar, m	Ice thickness, m
1	0 00	620	465	—
2	0 15	—	440	—
3	0 30	—	420	—
4	0 45	—	400	—
—	1 00	600	—	—
5	1 15	—	—	—
6	1 30	—	400	—
7	1 45	—	400	—
8	2 00	580	400	—
9	2 15	—	410	118
10	2 30	—	455	132
11	2 45	—	445	210
12	3 00	635	450	218
13	3 15	—	430	241
14	3 30	—	415	269
15	3 45	—	400	—
16	4 00	680	370	325
17	4 15	—	355	339
18	4 30	—	335	361
19	4 45	—	320	375
20	5 00	680	305	395
21	5 15	—	300	364
22	5 30	—	250	364
23	5 45	—	250	364
24	6 00	685	250	—
27	7 00	710	200	420
28	7 15	—	200	420
31	8 00	720	—	—
32	8 15	—	200	420

TABLE 1 (continued)

Measurement number	Time, hrs min	Flight altitude from barometric altimeter, m	Flight altitude according to radar, m	Ice thickness, m
Akademiya Nauk glacier, 9 October 1968, route d (continued)				
33	8 30	—	200	420
34	8 45	—	200	420
35	9 00	725	200	420
36	9 15	—	200	392
37	9 30	770	230	375
38	9 45	—	250	364
39	10 00	765	270	353
40	10 15	—	320	—
41	10 30	—	330	—
42	10 45	—	330	375
43	11 00	765	335	406
44	11 15	—	330	—
45	11 30	—	330	344
46	11 45	—	335	328
47	12 00	760	340	—
48	12 15	—	345	300
49	12 30	—	345	269
50	12 45	—	350	264
51	13 00	700	335	227
52	13 15	—	310	185
53	13 30	—	300	151
54	13 45	—	315	146
55	14 00	555	350	101
56	14 15	—	295	103
—	14 22	530	—	—

Note. Mean flight velocity 210 km/hr.

Akademiya Nauk glacier, 9 October 1968, route e

Measurement number	Time, hrs min	Flight altitude from barometric altimeter, m	Flight altitude according to radar, m	Ice thickness, m
1	0 00	620	400	70
2	0 15	—	365	106
3	0 30	—	305	179
4	0 45	—	295	238
5	1 00	755	300	246
6	1 15	—	320	—
7	1 30	—	320	252
8	1 45	—	325	333
9	2 00	755	325	378
10	2 15	—	320	370
11	2 30	—	300	364
12	2 45	—	275	—
13	3 00	825	255	—
14	3 15	—	250	403
15	3 30	—	250	408
16	3 45	—	250	414
17	4 00	930	260	420
18	4 15	—	270	426
19	4 30	—	300	437
20	4 45	—	300	420
21	5 00	930	300	431
22	5 15	—	300	431
23	5 30	—	300	420
24	5 45	—	280	437

TABLE 1 (continued)

Measurement number	Time, hrs min	Flight altitude from barometric altimeter, m	Flight altitude according to radar, m	Ice thickness, m
Akademiya Nauk glacier, 9 October 1968, route e (continued)				
25	6 00	950	270	442
26	6 15	—	260	459
27	6 30	—	270	465
28	6 45	—	250	487
29	7 00	970	240	482
33	8 00	1040	—	—
35	8 30	—	230	599
37	9 00	1050	230	577
41	10 00	1065	—	—
43	10 30	—	230	—
45	11 00	1060	—	—
49	12 00	1025	—	—
50	12 15	—	230	—
53	13 00	1010	—	—
56	13 45	—	250	—
57	14 00	970	—	—
60	14 45	—	250	—
61	15 00	925	—	—
65	16 00	860	300	—
69	17 00	785	—	—
70	17 15	—	300	—
72	18 00	785	300	448
74	18 30	—	300	392
75	18 45	—	300	—
76	19 00	765	300	—
77	19 15	—	300	420
78	19 30	—	300	—
79	19 45	—	300	—
80	20 00	735	300	392
81	20 15	—	300	—
82	20 30	—	300	336
83	20 45	—	300	—
84	21 00	620	300	280
85	21 15	—	300	280
86	21 30	—	270	280
87	21 45	—	280	269
88	22 00	565	285	171
89	22 15	—	330	168
90	22 30	—	345	210
91	22 45	—	410	—
92	23 00	575	405	193
93	23 15	—	420	—
94	23 30	—	435	—
95	23 45	—	425	—
96	24 00	570	440	—
97	24 15	—	455	—
98	24 30	—	500	34
99	24 45	—	510	22
100	25 00	565	525	—
101	25 15	—	535	—
102	25 30	540	575	—

Note. Initial flight velocity 200 km/hr. Terminal flight velocity 220 km/hr. Frames Nos. 88 through 100 obtained above a crevissed glacier. Barometric flight altitude reading taken 1 min before the beginning of measurements, 540 m.

TABLE 1 (continued)

Measurement number	Time. hrs min	Flight altitude from barometric altimeter, m	Flight altitude according to radar, m	Ice thickness, m
Akademiya Nauk glacier, 9 October 1968, route f				
1	0 00	620	320	—
2	0 15	—	315	255
3	0 30	—	310	269
4	0 45	—	300	302
5	1 00	660	295	350
6	1 15	—	280	403
7	1 30	—	290	426
8	1 45	—	300	403
9	2 00	760	290	408
10	2 15	—	280	403
11	2 30	—	270	426
12	2 45	—	270	442
13	3 00	810	260	470
14	3 15	—	270	459
15	3 30	—	300	408
16	3 45	—	300	392
17	4 00	800	340	—
18	4 15	—	340	467
19	4 30	—	370	—
20	4 45	—	390	442
21	5 00	700	370	—
22	5 15	—	330	431
23	5 30	—	300	420
24	5 45	—	300	392
25	6 00	620	300	336
26	6 15	—	300	—
27	6 30	—	280	330
28	6 45	—	270	408
29	7 00	550	250	420
30	7 15	—	240	426
31	7 30	—	230	319
32	7 45	—	210	—
33	8 00	530	200	325
34	8 15	—	240	314
35	8 30	—	270	325
36	8 45	—	300	—
37	9 00	580	300	336
38	9 15	—	340	274
—	9 22	—	—	353
39	9 30	—	400	420
40	9 45	—	380	330
41	10 00	600	400	224
42	10 15	—	400	196
43	10 30	—	430	173
44	10 45	—	470	129
45	11 00	580	515	—
46	11 15	—	470	106
47	11 30	—	470	101
48	11 45	—	470	101
49	12 00	570	530	—
50	12 15	—	530	179
51	12 30	—	530	213
52	12 45	—	530	112
53	13 00	560	545	165
54	13 15	560	555	126

Note. Initial velocity 200 km/hr. Frames Nos. 22—28 and Nos. 48, 52, 53, 54 obtained over crevisses.

TABLE 1 (continued)

Measurement number	Time, hrs min	Flight altitude from barometric altimeter, m	Flight altitude according to radar, m	Ice thickness, m
		Al'banov glacier, 10 October 1968, route h		
1	0 00	590	340	33
2	0 15	—	280	104
3	0 30	—	265	182
4	0 45	640	245	204
5	1 00	—	250	227
6	1 15	—	265	266
7	1 30	—	280	274
8	1 45	720	290	291
9	2 00	—	305	300
10	2 15	—	310	314
11	2 30	—	300	319
12	2 45	740	300	—
13	3 00	—	300	302
14	3 15	—	300	347
15	3 30	—	305	344
16	3 45	730	310	336
17	4 00	—	330	302
18	4 15	—	355	260
19	4 30	—	415	185
20	4 45	700	460	140
21	5 00	—	535	64
22	5 15	—	565	75
23	5 30	730	600	0

Note. Flight velocity 200—210 km/hr.

Measurement number	Time, hrs min	Flight altitude from barometric altimeter, m	Flight altitude according to radar, m	Ice thickness, m
		Rusanov glacier, 10 October 1968, route j		
1	0 00	900	720	—
2	0 15	—	640	—
3	0 30	—	600	—
4	0 45	—	555	238
5	1 00	985	540	280
6	1 15	—	500	314
7	1 30	—	480	358
8	1 45	—	450	364
9	2 00	970	430	392
10	2 15	—	415	395
11	2 30	—	405	406
12	2 45	—	405	433
13	3 00	1000	400	437
14	3 15	—	395	—
15	3 30	—	380	—
16	3 45	—	400	448
17	4 00	1010	400	437
18	4 15	—	400	420
19	4 30	—	400	—
20	4 45	—	400	403
21	5 00	1015	400	420
22	5 15	—	410	358
23	5 30	—	400	336
24	5 45	—	370	—
25	6 00	1045	360	274
26	6 15	—	350	269

TABLE 1 (continued)

Measurement number	Time, hrs min	Flight altitude from barometric altimeter, m	Flight altitude according to radar, m	Ice thickness, m
Rusanov glacier, 10 October 1968, route j (continued)				
27	6 30	—	305	—
28	6 45	—	350	336
29	7 00	1085	350	280
30	7 15	—	330	213
31	7 30	—	365	288
32	7 45	—	380	235
33	8 00	1100	400	258
34	8 15	—	430	252
35	8 30	—	490	193
36	8 45	—	500	190
37	9 00	1150	545	—
38	9 15	—	665	143
39	9 30	—	880	123
40	9 45	—	980	92
41	10 00	1190	1000	—
42	10 15	—	1030	—
43	10 30	—	1080	—
44	10 45	—	1100	—
45	11 00	1200	1150	84
46	11 15	—	1150	84
47	11 30	—	1150	—
48	11 45	—	1150	—
—	12 00	1190	—	—

Note: Flight velocity 200—210 km/hr. Frames Nos. 38 through 48 obtained over crevisses.

Ushakov glacier, 15 October 1968, route o

Measurement number	Time, hrs min	Flight altitude from barometric altimeter, m	Flight altitude according to radar, m	Ice thickness, m
1	0 00	370	370	0
2	0 15	380	360	—
3	0 30	400	370	—
4	0 45	425	365	87
5	1 00	445	390	84
6	1 15	470	405	75
7	1 30	470	410	84
8	1 45	480	400	84
9	2 00	470	400	78
10	2 15	465	380	92
11	2 30	470	390	92
12	2 45	475	390	112
13	3 00	480	340	151
14	3 15	495	350	219
15	3 30	535	355	216
16	3 45	565	345	230
17	4 00	575	340	246
18	4 15	595	340	252
19	4 30	600	350	—
20	4 45	610	350	241
21	5 00	605	350	230
22	5 15	565	340	207
23	5 30	545	340	187
24	5 45	520	350	151
25	6 00	465	360	92
26	6 15	435	410	45

Note. Initial flight velocity 200 km/hr. Terminal flight velocity 225 km/hr.

TABLE 1 (continued)

Measurement number	Time, hrs min	Flight altitude from barometric altimeter, m	Flight altitude according to radar, m	Ice thickness, m
Ushakov glacier, 15 October 1968, route p

Measurement number	Time, hrs min	Flight altitude from barometric altimeter, m	Flight altitude according to radar, m	Ice thickness, m
1	0 00	535	530	0
2	0 15	545	485	70
3	0 30	555	460	106
4	0 45	600	420	151
5	1 00	610	425	182
6	1 15	610	410	—
7	1 30	615	400	—
8	1 45	625	400	168
9	2 00	635	400	168
10	2 15	630	400	—
11	2 30	635	400	—
12	2 45	630	400	185
13	3 00	620	400	196
14	3 15	605	410	162
15	3 30	565	435	162
16	3 45	555	450	126
17	4 00	530	430	118
18	4 15	510	445	98
19	4 30	500	430	84
20	4 45	480	425	—
21	5 00	465	415	—
22	5 15	455	420	45
23	5 30	430	430	—

Note. Flight velocity approximately constant, 210 km/hr.

Shmidt glacier, 15 October 1968, route k

Measurement number	Time, hrs min	Flight altitude from barometric altimeter, m	Flight altitude according to radar, m	Ice thickness, m
1	0 00	450	430	—
2	0 15	490	410	—
3	0 30	515	360	92
4	0 45	530	330	174
5	1 00	570	295	—
6	1 15	—	280	280
7	1 30	610	260	291
8	1 45	—	280	252
9	2 00	670	300	—
10	2 15	—	320	252
11	2 30	660	350	—
12	2 45	—	370	185
13	3 00	630	400	—
14	3 15	—	430	—
15	3 30	605	440	157
16	3 45	—	465	98
17	4 00	580	450	140
18	4 15	—	445	Two reflected signals 92 and 137 m
19	4 30	555	445	87
20	4 45	—	450	78
21	5 00	545	435	112
22	5 15	—	435	98
23	5 30	500	450	73
24	5 45	—	500	28
25	6 00	490	490	0

Note. Flight velocity 200—220 km/hr. Frame No. 18 reflects an abrupt change in the heights of the bedrock topography.

TABLE 1(continued)

Measurement number	Time, hrs min	Flight altitude from barometric altimeter, m	Flight altitude according to radar, m	Ice thickness, m
Shmidt glacier, 15 October 1968, route 1				
1	0 00	465	465	0
2	0 15	—	420	67
3	0 30	475	395	95
4	0 45	—	370	135
5	1 00	505	360	154
6	1 15	—	360	—
7	1 30	560	360	162
8	1 45	—	370	168
9	2 00	610	380	224
10	2 15	—	350	251
11	2 30	625	330	235
12	2 45	—	320	252
13	3 00	650	300	258
14	3 15	—	290	274
15	3 30	670	270	—
16	3 45	—	260	302
17	4 00	675	250	291
18	4 15	—	260	274
19	4 30	660	280	—
20	4 45	—	300	235
21	5 00	655	320	—
22	5 15	—	340	—
23	5 30	645	360	185
24	5 45	—	390	—
25	6 00	620	390	—
26	6 15	—	395	168
27	6 30	—	420	137
28	6 45	—	430	118
29	7 00	560	500	56
30	7 15	—	500	—

Note. Flight velocity 190—215 km/hr.

Akademiya Nauk glacier 15 October 1968, route g				
1	0 00	700	615	93
2	0 10	—	570	162
3	0 20	—	535	190
4	0 30	720	480	252
5	0 45	—	435	294
6	1 00	690	400	316
7	1 15	—	380	347
8	1 30	700	350	375
9	1 45	—	320	397
10	2 00	700	300	419
11	2 15	—	300	447
12	2 30	750	320	437
13	2 45	—	330	443
14	3 00	780	330	443
15	3 15	—	330	432
16	3 30	820	350	419
17	3 45	—	350	419
18	4 00	850	350	419
19	4 15	—	350	419
20	4 30	875	350	419
21	4 45	—	350	432
22	5 00	—	350	432

13

TABLE 1 (continued)

Measurement number	Time, hrs min	Flight altitude from barometric altimeter, m	Flight altitude according to radar, m	Ice thickness, m

Akademiya Nauk glacier, 15 October 1968, route g (continued)

Measurement number	Time, hrs min	Flight altitude from barometric altimeter, m	Flight altitude according to radar, m	Ice thickness, m
23	5 15	—	350	425
24	5 30	930	—	—
32	7 30	960	—	—
34	8 00	970	—	—
—	9 30	1000	—	—
—	10 00	1025	—	—
44	15 15	—	400	476
45	15 30	960	400	447
46	15 45	—	400	408
47	16 00	—	400	392
48	16 15	—	400	381
49	16 30	900	400	381
50	16 45	—	390	381
51	17 00	—	380	408
52	17 15	—	380	403
53	17 30	—	380	403
54	17 45	—	380	392
55	18 00	—	380	413
56	18 15	—	370	448
57	18 30	—	370	437
58	18 45	—	380	420
59	19 00	—	380	413
60	19 15	—	390	387
61	19 30	830	400	364
62	19 45	—	400	358
63	20 00	—	420	328
64	20 15	—	430	308
65	20 30	—	475	274
66	20 45	—	495	261
67	21 00	830	520	241
68	21 15	—	555	216
69	21 30	—	605	202
70	21 45	—	675	143
71	22 00	—	705	90

Note. Flight velocity varying from 215 km/hr (initial) to 230 km/hr (terminal).

Al'banov glacier, 15 October 1968, route i

Measurement number	Time, hrs min	Flight altitude from barometric altimeter, m	Flight altitude according to radar, m	Ice thickness, m
1	0 00	—	670	0
2	0 15	—	650	0
3	0 30	—	645	48
4	0 45	—	590	106
5	1 00	815	530	191
6	1 15	—	460	280
7	1 30	—	430	302
8	1 45	—	400	336
9	2 00	810	375	347
10	2 15	—	335	338
11	2 30	800	300	336
12	2 45	—	295	327
13	3 00	795	295	395
14	3 15	—	295	395
15	3 30	—	310	375
16	3 45	—	340	319

14

TABLE 1 (continued)

Measurement number	Time, hrs min	Flight altitude from barometric altimeter, m	Flight altitude according to radar, m	Ice thickness, m

Al'banov glacier, 15 October 1968, route i (continued)

17	4 00	—	345	322
18	4 15	—	370	280
19	4 30	—	390	246
20	4 45	—	430	185
21	5 00	790	490	112
22	5 15	—	605	31

Note. Flight velocity 200 km/hr.

Vavilov glacier, 15 October 1968, route m

1	0 00	740	475	42
2	0 15	—	395	101
3	0 30	—	345	123
4	0 45	—	305	176
5	1 00	760	325	254
6	1 15	—	325	243
7	1 30	900	315	260
8	1 45	—	310	305
9	2 00	950	305	344
10	2 15	—	325	422
—	2 30	1000	—	—

Note. Flight velocity 185 km/hr.

Ushakov glacier, 16 October 1968, route r

1	0 00	355	340	50
2	0 15	385	355	78
3	0 30	425	395	53
4	0 45	—	360	100
5	1 00	455	310	151
6	1 15	—	280	213
7	1 30	—	280	238
8	1 45	—	280	268
9	2 00	575	290	291
10	2 15	—	300	294
11	2 30	610	—	—
12	2 45	—	330	287
13	3 00	605	—	—
15	3 30	555	—	—
16	3 45	—	360	146
17	4 00	—	375	112
18	4 15	—	435	62
19	4 30	—	495	36
20	4 45	525	525	—

Note. Flight velocity 190—200 km/hr.

15

TABLE 1 (continued)

Measurement number	Time, hrs min	Flight altitude from barometric altimeter, m	Flight altitude according to radar, m	Ice thickness, m
Ushakov glacier, 16 October 1968, route s				
1	0 00	380	380	20
2	0 15	—	380	45
3	0 30	390	375	50
4	0 45	—	365	62
5	1 00	415	385	123
6	1 15	—	330	151
7	1 30	—	330	185
8	1 45	—	315	204
9	2 00	540	300	252
10	2 15	—	310	277
11	2 30	590	320	297
12	2 45	—	330	290
13	3 00	630	345	280
15	3 30	615	—	—
17	4 00	605	—	—
20	4 45	—	370	176
21	5 00	545	400	123
22	5 15	—	435	87
23	5 30	500	500	—

Note. Flight velocity 200—205 km/hr.

V. V. Bogorodskii, G. P. Khokhlov, B. A. Fedorov,
and G. V. Trepov

ELECTRICAL PARAMETERS OF THE MODELS OF MORAINIC LAYERS IN THE REGION OF THE ANOMALOUS DISPERSION OF ICE

Structural studies of glaciers, and particularly determination of the depth, thickness, and constitution of morainic formations, is of the greatest importance. Radio-physical methods of measurements are used on a progressively growing scale in this field /1/. Knowledge of the electrical properties of ice with various content and composition of moraines therefore acquires particular significance, and yet no published data are available on the subject.

Ice—rock mixtures may form under natural conditions for two different reasons: the freezing of a water-saturated rock and mechanical intermixing of rocks with snow or ice. The first mechanism is largely responsible for the formation of permafrost, whereas the second leads to the formation of moraines in alpine glaciers. Intermediate cases are also possible, whereby partial or complete thawing alternates with freezing of existing mixtures.

The electrical properties of rock-ice mixtures are best treated separately in the region of the anomalous dispersion of ice and in the radio-frequency region. The present paper is concerned with the electrical properties of rock—ice mixtures in the region of the anomalous dispersion of ice.

The measurements were carried out using Antarctic samples of granite, porphyritic hyalobasalt, and pyroxene andesite with indistinctly fluidal texture. The specific weights of the minerals were 2.68, 2.76, and 2.43 g/cm³, respectively. To prepare the test mixtures, the minerals were crushed and the sand was passed through 0.5 and 1.5 mm sieves. Then the sand was carefully washed and kept for a few weeks in distilled water, which was periodically changed. The permittivity of the powdered minerals with specific weight of about 1.8 g/cm³ is an almost linear function of frequency; it falls between 5.5 and 7 at 300 Hz and between 4.2 and 5 at 20 kHz. The dielectric loss angle of powdered granites, basalt, and andesite is respectively 0.185, 0.173, 0.145 at 300 Hz, 0.105, 0.125, 0.138 at 6.5 kHz, and 0.065, 0.82, and 0.112 at 20 kHz.

Two different methods of sample preparation were used, corresponding to the two different mechanisms of formation of ice—rock mixtures in nature.

The samples corresponding to the frozen mixture model were prepared at −20°C using a rubber washer placed on a metal plate. Powdered mineral was poured into the washer and then topped with distilled water. To ensure low concentrations of the mineral in the sample, the powder was placed on previously frozen ice layers. The capacitor electrodes were coated with

a layer of ice about 1 mm thick. When the electrodes and the sample froze through, the sample was rapidly bonded to the electrodes by a thin interlayer of water. The capacitor contained an MT-54 thermistor flush with one of the electrode surfaces. The temperature was measured with a resistance thermometer to within ±0.2°C. The capacitor was kept in a TKSI 0.1/70 thermostating chamber, and its parameters were measured with E8-2 bridge.
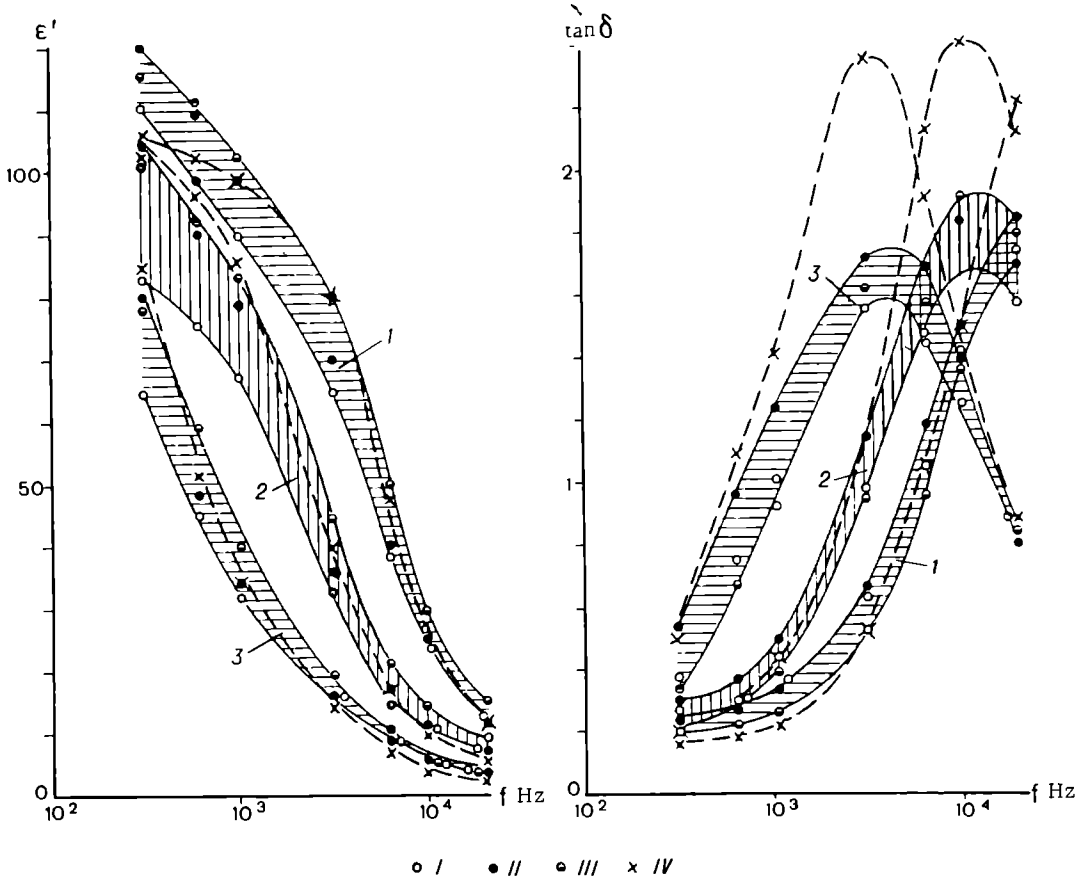
FIGURE 1. ε' and tan δ as a function of frequency for ice with mineral enclosures (frozen mineral powder) at various temperatures:

1) -5°C; 2) -15°C; 3) -30°C. I granite; II basalt; III andesite; IV layered ice.

Figure 1 plots the permittivity ε' and the loss angle tan δ as a function of frequency for frozen mixtures prepared by this method. The weight content of the minerals (the ratio of the weight P_m of the mineral in the sample to the total weight of the sample P_{tot}) was approximately constant: 33.2% for the ice—granite mixture, 32.5% for the ice—basalt mixture, and 33.2% for the ice—andesite mixture. Figure 1 also shows the characteristics of layered ice obtained by freezing successive layers in the capacitor. A reduction of the total ice content in the sample leads to a certain reduction in the loss angle of the mixture, but the permittivity remains close to that of pure ice. Further increase in the concentration of the mineral in the sample, however, leads to a marked increase in ε' (Figure 2). The loss angle also increases. These curves can be attributed to migration polarization effects associated with the presence of components with different electric

18

parameters in the sample and with partial washing out of the water-soluble components from the minerals. As the mineral concentration in the sample is increased, ε' and tan δ should first drop because of the reduction of the ice content and the initially weak contribution of the migration polarization (this is clear for curves corresponding to $-30°C$). As P_m/P_{tot} is further increased, the effect of migration polarization and the related losses overweigh the reduction of ε' and tan δ caused by the decrease of the ice volume.
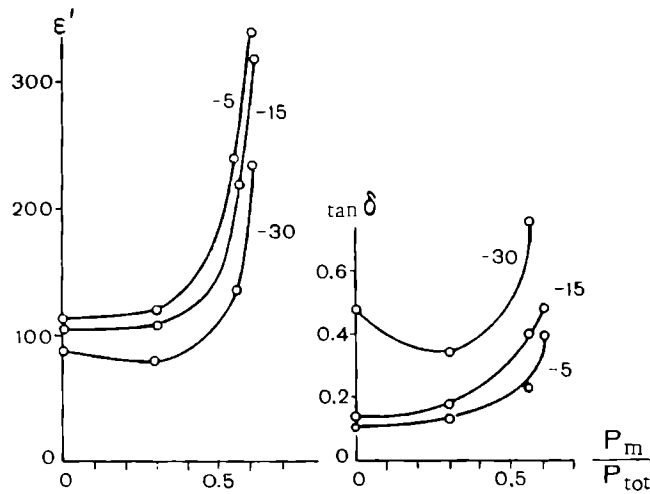
FIGURE 2. ε' and tan δ as a function of concentration for an ice — andesite mixture prepared by freezing (300 Hz frequency).
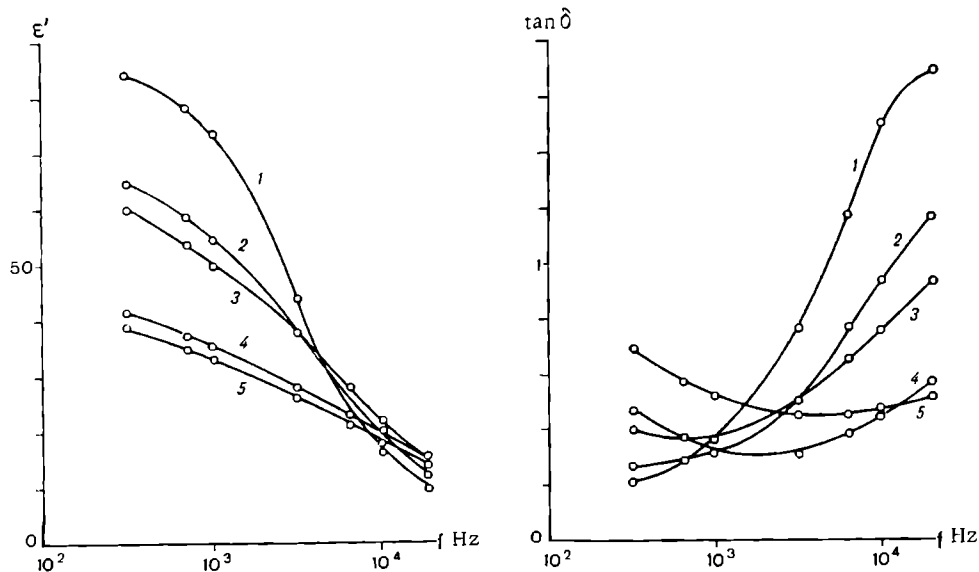
FIGURE 3. ε' and tan δ as a function of frequency for an ice — andesite mixture prepared by pressure forming with different P_m/P_{tot} :

1) ice; 2) 0.288; 3) 0.475; 4) 0.632; 5) 0.724. Temperature, $-10°C$.

19

Samples corresponding to a mixture of ice or snow with rocks were prepared in a different capacitor. Powdered mineral mixed with fine ice shavings (the ice was prepared from distilled water) was poured into the capacitor. The mixture was allowed to set at $-10°C$ under 300 atm pressure for $10-15$ min. The capacitor was then removed to the thermostating chamber for measurements. The frequency curves of ε' and tan δ obtained at $-10°C$ (Figure 3) and the dependence of ε' and tan δ on the weight concentration (or the volume concentration V_m/V_{tot}) (Figure 4) have no features in common with the curves in Figures 1 and 2. The permittivity of the mixture at low frequencies decreases with the increase in P_m/P_{tot}, but at 20 kHz, as in the previous case, the ε' of the mixture is higher than the ε' of ice. This is so because at high frequencies the permittivity of minerals is higher $(6-17)$ /2/ than the permittivity of ice. We see from Figure 4 that for medium concentrations of the mineral in the sample, migration polarization may develop, although its effect is very small.
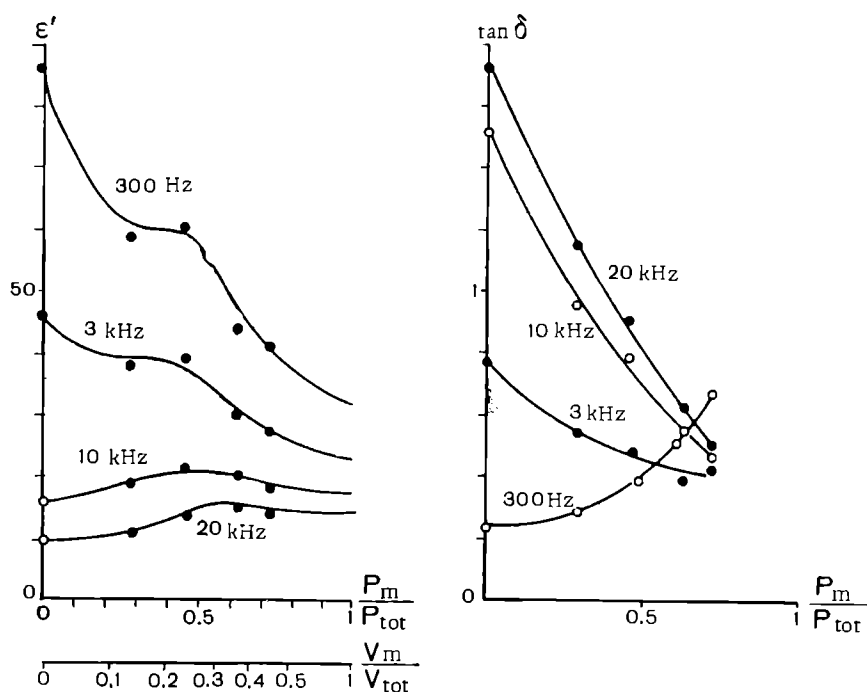
FIGURE 4. ε' and tan δ as a function of concentration for ice—andesite mixture prepared by pressure forming. Temperature, -10°C.

Comparison of the curves of permittivity and loss angle for ice—mineral mixtures prepared by two different methods shows that the electrical properties of mixtures in the region of the anomalous dispersion of ice are significantly different and depend on the method of preparation. The decisive factor is the presence of water in the mixture at some stage of its formation. The trend of the frequency curves suggests that in the radiofrequency region the electrical properties of mixtures will be independent of the method of preparation.

Bibliography

1. Bogorodskii, V. V. Fizicheskie metody issledovaniya lednikov
    (Physical Methods of Studying Glaciers).— Leningrad, Gidro-
    meteoizdat. 1968.
2. Veshev, A. V. Laboratornye issledovaniya zavisimosti dielektricheskoi
    pronitsaemosti i udel'noi elektroprovodnosti obraztsov gornykh
    porod ot chastoty elektromagnitnykh kolebanii (Laboratory Studies
    of the Dependence of the Permittivity and the Conductivity of
    Rock Samples of Electromagnetic Wave Frequency).— In: Geofizi-
    cheskie metody razvedki." VIRB. Moskva. 1955.

G. P. Khokhlov

INVESTIGATION OF THE ELECTRICAL CHARAC-TERISTICS OF SWEET ICE FOR VARIOUS TEXTURAL MODELS

Natural ice is characterized by definite texture and structure. If the effect of residual salinity is ignored, the electrical properties of ice are determined completely by the shape and orientation of the constituent crystals and also by the shape, orientation, and content of air inclusions. Elucidation of the effect of ice texture and structure on the electrical properties of ice is highly important for methodological reasons: considerable attention is generally devoted to measurement techniques, whereas the ice texture and structure are ignored (in some cases, e.g.. in measurements using a cylindrical capacitor, the ice structure is very difficult to determine). Therefore, some discrepancies in the results of different authors may be due not only to different measurement techniques but also to differences in the texture and structure of the ice samples used.

The present paper considers the effect of texture on the electrical properties in the region of the anomalous dispersion.

The measurements were carried out with E8-2 bridge which is adapted to remote measurements of the capacitance and conductance of capacitors to within about 0.2% between 100 Hz and 20 kHz. A G3-33 oscillator supplied the bridge. An oscillograph connected to the output of a U2-6 selective amplifier of $1 \mu V$ sensitivity was used as a null indicator. Plate capacitors with a guard ring were used in measurements. Nickel-plated brass electrodes were employed. The guard-ring electrode was 60 mm in diameter. A MT-54 thermistor was set flush with the surface of the other electrode; the thermistor was connected to an electrothermometer and ensured temperature measurements with an accuracy of $\pm 0.2°C$. The capacitor with the ice sample between the plates was kept in a TKSI 01/70 thermostating chamber.

Preparation of ice specimens with predetermined texture is an involved problem. However, the simplest textures can be obtained by fairly simple methods of varying the temperature and the rate of freezing, the concentration of gas in water, the temperature gradient, or by inducing icing, by freezing of crushed ice, etc.

Our problem was somewhat more complicated as we wished to obtain various textural models of distilled ice of constant purity. The constant purity was ensured by allowing water to freeze in carefully washed glass flasks of up to 8 liter volume. Before freezing, samples were withdrawn from each flask to determine the electrical conductivity of water; the constant of the cell used in these measurements was determined at 1 kHz relative to normal water of known conductivity /1/. At +25°C, the conductivity of water from the five flasks ranged between $3.7 \cdot 10^{-6}$ and $3.9 \cdot 10^{-6} (ohm \cdot cm)^{-1}$.
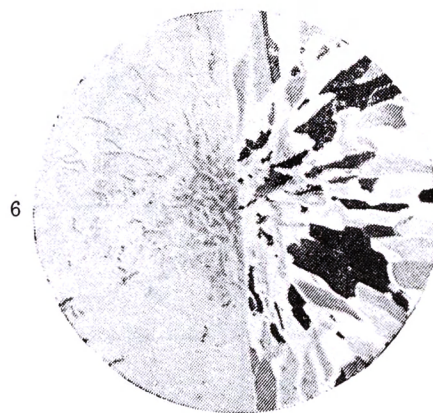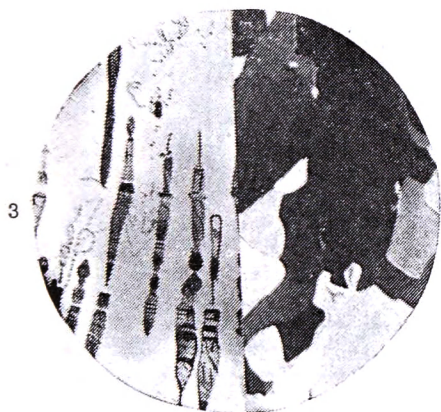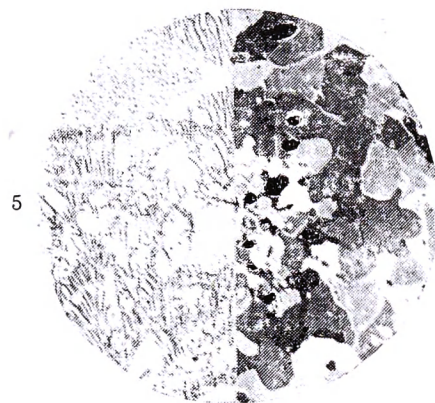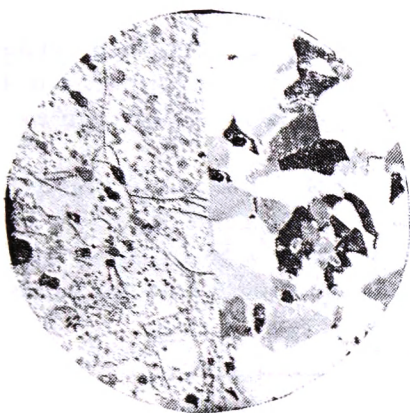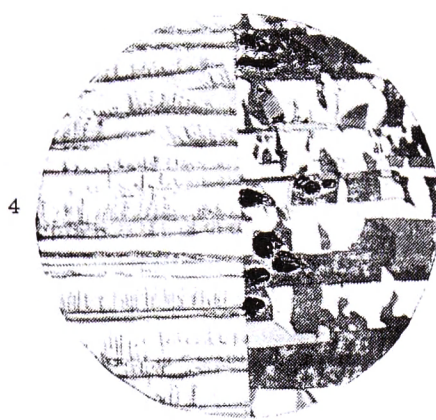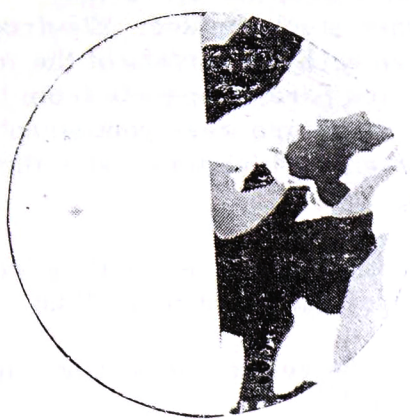
FIGURE 4. Photographs of ice texture and structure.

1) monolithic ice; 2) bubbly ice; 3) ice with tubular inclusions; 4) layered ice; 5) frozen conglomerate of crushed ice fragments; 6) ice of fan-shaped structure.

23

Plates 10−12 mm thick were cut from the ice slabs, and all further operations were carried out on a carefully washed steel surface. Electrodes extracted from warm distilled water were frozen onto the surface of the ice plates. After the measurements, the density of ice parallelepipeds from the samples was determined, and their texture and structure were photographed. The ice texture photographs (Figure 1) show the area which was under the guard-ring electrode during the measurements.

The following varieties of ice were obtained.

1) Monolithic ice without air inclusions. Specific weight $\rho = 0.915\,\text{g}/\text{cm}^3$.

2) Bubbly ice, with numerous spherical air inclusions not more than 2.5 mm in diameter, $\rho = 0.87\,\text{g}/\text{cm}^3$.

3) Ice with tubular air inclusions extending in the vertical direction, up to 3 mm in diameter and 3.5 cm long, $\rho = 0.89\,\text{g}/\text{cm}^3$.

4) Layered ice, obtained by successive freezing of surface layers, with preferentially filamental air inclusions, $\rho = 0.9\,\text{g}/\text{cm}^3$.

5) Ice corresponding to dynamometamorphic texture, prepared by freezing of crushed ice, $\rho = 0.9\,\text{g}/\text{cm}^3$.

6) Ice of fan-shaped structure, obtained from water frozen in a cylindrical beaker. This ice contained a small number of filamental air bubbles in the radial direction and minute bubbles (in the form of white froth) in the axial direction. $\rho = 0.91\,\text{g}/\text{cm}^3$.

Air impurities could only penetrate into the ice of dynamometamorphic texture, since ice in this case was crushed in a polyethylene bag. To avoid contamination of the layered ice with impurities, water was injected into the flask with a sterilized syringe. All the other ice modifications were prepared by freezing in a glass vessel.
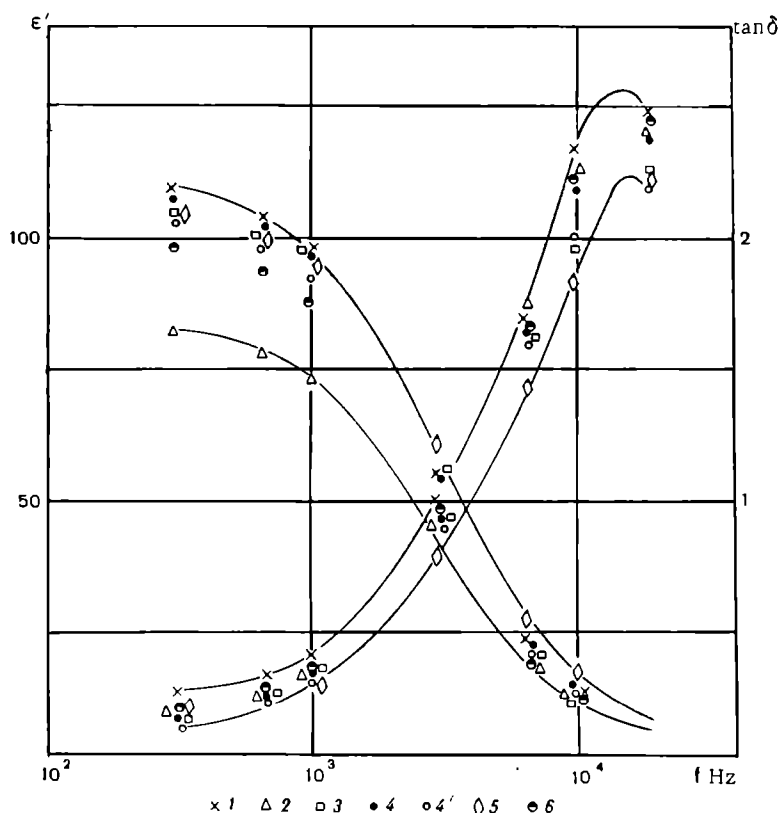
FIGURE 2. ε' and tan δ as a function of frequency, $t = -10°C$:

Legend as in Figure 1; 4) field perpendicular to layers; 4') field parallel to layers.

24
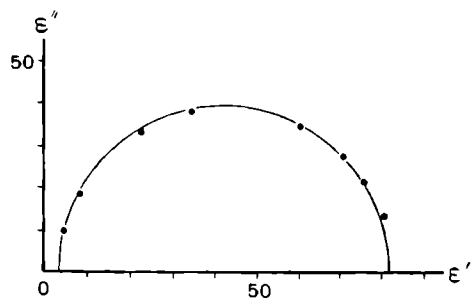
FIGURE 3. Cole—Cole plot for bubbly ice,
$t = 10°C.$
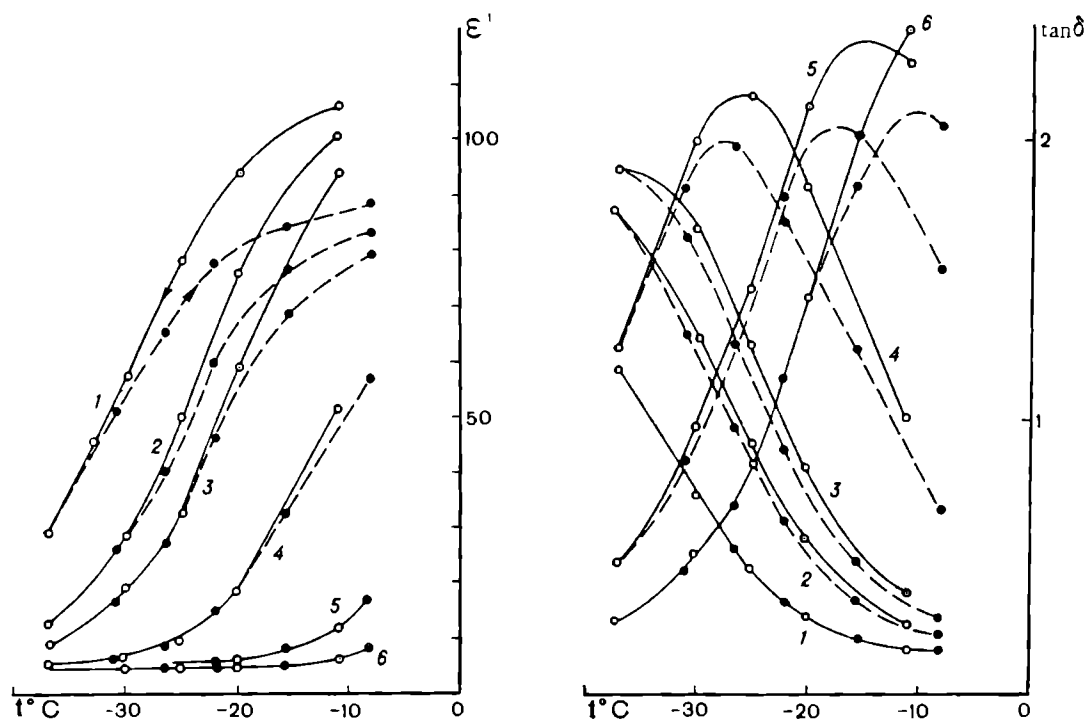
FIGURE 4. ϵ' and tan δ as a function of temperature (the temperature was first lowered until cracks appeared in the ice samples, and the measurements made with rising temperature):

1) 300 Hz; 2) 650 Hz; 3) 3 kHz; 4) 6.5 kHz; 5) 10 kHz; 6) 20 kHz.

The permittivity ε', the loss angle tan δ, and the loss factor ε'' were computed from the relations

$$\varepsilon' = \frac{C}{C_0},$$

$$\tan \delta = \frac{G}{2\pi f C}$$

$$\varepsilon'' = \varepsilon' \tan \delta,$$

where C and G are the measured capacitance and conductance of the ice-filled capacitor, C_0 is the geometrical capacitance of the capacitor.

Figure 2 plots the frequency curves of ε' and tan δ for the different ice samples. We see from the figures that textural differences produce a difference of up to 30 % in ε' and of up to 60 % in tan δ. Allowing for the accuracy of the bridge, the accuracy with which the geometrical capacitance is determined, and the accuracy of frequency measurements, we conclude that ε' and tan δ in these measurements are accurate to within 1 % and 1.5 %, respectively. The values of ε' and ε'' obtained for all the samples closely follow the Cole—Cole plot (Figure 3), which proves that the measurements are fairly accurate. For samples of identical structure, the reproducibility of measurements was no better than 4 %. Note that the formation of cracks in the specimen at low temperatures markedly influences the temperature curves of ε' and tan δ. This is evident from the temperature curves of ε' and tan δ (Figure 4) of layered ice (with the field at right angles to the direction of the layers) which were plotted by first reducing the temperature until cracks appeared in the specimen and then raising the temperature to the original level. This fact is particularly significant for assessing the state of ice in electrical measurements.

Bibliography

1. S o p a c h, E. D. Elektroprovodnost' kak metod opredeleniya solenosti morskikh vod (Electrical Conductivity as a Method of Determination of the Salinity of Sea Water).— Moskva, Gidrometeoizdat. 1958.

G. P. Khokhlov

MEASUREMENTS OF THE ELECTRICAL PROPERTIES
OF ICE WITH A TWO-WIRE LINE

Measurements of the electrical properties of ice require sufficiently simple and reliable measurement techniques. The permittivity and the conductivity of floating ice at radio frequencies can be determined using a pair of two-wire lines of different length. Two-wire lines generate a sufficiently extensive field inside the ice layer and make it possible to conduct measurements without contact electrodes /1/, using standard enamelled wires.

Figure 1 is a schematic diagram showing a pair of two-wire lines which may be placed on the ice surface separately, one next to the other, or so that one line is a direct continuation or part of the other. The capacitances of the first and the second lines are respectively given by

$$C_{meas1} = C_1 + C_{ice1} + C_1' + C_{ice1}',$$
$$C_{meas2} = C_2 + C_{ice2} + C_2' + C_{ice2}', \tag{1}$$

where C_1 and C_2 are the capacitances in air above the lines, ignoring the edge capacitances in air C_1' and C_2'; C_{ice1} and C_{ice2} are the capacitances in ice under the lines, ignoring the edge capacitances in ice C_{ice1}' and C_{ice2}'.

Seeing that for sufficiently long lines $C_1' = C_2'$ and $C_{ice1}' = C_{ice2}'$, we obtain from (1)

$$C_{meas1} - C_{meas2} = (C_1 - C_2) + (C_{ice1} - C_{ice2}).$$

Hence

$$\Delta C_{ice} = C_{ice1} - C_{ice2} = (C_{meas1} - C_{meas2}) - (C_1 - C_2). \tag{2}$$

The capacitances C_1 and C_2 can be determined as half the line capacitances in air using the relation for the capacitance of an infinite two-wire line:

$$C_1 = \frac{1}{2} 0.12 \frac{l_1}{\log \frac{2h}{d}},$$
$$C_2 = \frac{1}{2} 0.12 \frac{l_2}{\log \frac{2h}{d}}.$$

where d is the wire diameter in cm, h is the wire separation in cm.

Hence

$$C_1 - C_2 = 0.06(l_1 - l_2)\frac{1}{\log\frac{2h}{d}} . \tag{3}$$
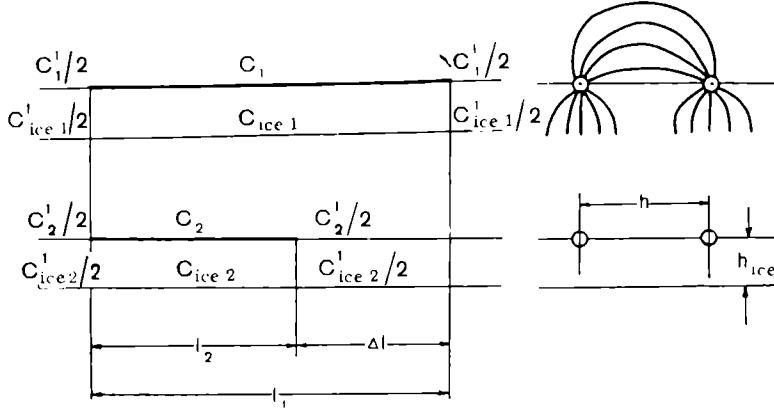
FIGURE 1. Two-wire lines above a conducting surface.

From (2) and (3) we have

$$\Delta C_{ice} = (C_{meas1} - C_{meas2}) - 0.06(l_1 - l_2)\frac{1}{\log\frac{2h}{d}} . \tag{4}$$

The permittivity of ice can be found from the relation

$$\varepsilon' = \frac{\Delta C_{ice}}{\Delta C_0} , \tag{5}$$

where ΔC_0 is the capacitance of a wire of length $\Delta l = l_1 - l_2$ at a distance h_{ice} above the conducting surface (since the capacitances of the two wires are connected in a series). As the edge capacitances are ignored, ΔC_0 may be computed from the expression for the capacitance of a single wire above a conducting surface:

$$\Delta C_0 = \frac{1}{2}0.24\frac{\Delta l}{\log\frac{4h_{ice}}{d}} . \tag{6}$$

From (4), (5), and (6) it follows that

$$\varepsilon' = \frac{(C_{meas\,1} - C_{meas\,2})\log\frac{2h}{d} - 0.06(l_1 - l_2)}{0.12(l_1 - l_2)\log\frac{2h}{d}}\log\frac{4h_{ice}}{d} . \tag{7}$$ *

By measuring the conductance of lines on an ice surface we can find the loss angle tan δ of the ice cover and its volume conductivity γ. Ignoring the conductance of the lines in the upper hemisphere, we obtain the following

* Here $C_{meas\,1}$ and $C_{meas\,2}$ are expressed in cm.

28

expressions for the measured conductance of the lines:

$$G_{meas1} = G'_{ice1} + G_{ice\ 1}.$$
$$G_{meas2} = G'_{ice2} + G_{ice\ 2}.$$

Since $G'_{ice\ 1} = G'_{ice2}$, we have $\Delta G_{meas} = G_{meas1} - G_{meas2} = G_{ice1} - G_{ice2}$, i.e., ΔG_{meas} is equal to the conductance of the line segment under the length Δl. Then

$$\tan \delta = \frac{\Delta G_{meas}}{2\pi f \Delta C_{ice}}, \quad \gamma = \frac{\varepsilon' f \tan \delta}{1.8 \cdot 10^{12}} \ (ohm \cdot cm)^{-1},$$

where f is the frequency.

The field patterns of a single wire and a two-wire line on a metallic surface, obtained by simulation with an electrically conducting paper /2/, show that already for $\frac{h}{h_{ice}} = 4 - 5$ the field of a single wire is equivalent to the field of each wire of the two-wire line, and the above computations apply.

To check this method, we built a tub with a duralumin bottom above which a pair of two-wire lines were stretched. Each wire could be disconnected by a toggle switch. The ice in the tub was frozen successively, layer by layer, so that it contained cracks and small air inclusions. Distilled water was used. The measurements were carried out at $-5°C$ with E12-1 bridge. The principal parameters of the long lines and the measurement results were as follows: $h = 10.2$ cm, $l_1 = 82$ cm, $h_{ice} = 2$ cm, $l_2 = 30$ cm, $d = 0.25$ cm, $C_{meas1} = 23.8$ pF, $C_{meas\ 2} = 11.5$ pF, $\varepsilon' = 2.907$.

In March 1969 the method was tested for the ice cover of Lake Ladoga, which was then 80 cm thick. The line parameters were as follows: $l_1 = 1240$ cm, $l_2 = 532$ cm, $h = 430$ cm, $d = 0.25$ cm, $C_{meas\ 1} = 298$ pF, $C_{meas\ 2} = 211.5$ pF. The permittivity was found to be $\varepsilon' = 3.11$. This result fits the published data (around 700 kHz), so that the theoretical assumptions used in the derivation of the relevant expressions seem to be applicable.

This method can be applied to determine the ice thickness if the permittivity is known. The expression for the ice thickness can be derived from (7),

$$\log h_{ice} = \frac{\varepsilon'}{a} + \log d - \log 4,$$

where

$$a = \frac{(C_{meas\ 1} - C_{meas\ 2}) \log \frac{2h}{d} - 0.06\ (l_1 - l_2)}{0.12\ (l_1 - l_2) \log \frac{2h}{d}}.$$

The method may also be applied to determine the electrical parameters of other solid, powdered, and liquid dielectrics.

Bibliography

1. Bogorodskii, V. V. and G. P. Khokhlov. Measurements of the Permittivity and Conductivity of Sea Ice without Contact Electrodes. — This collection, p. 77.
2. Ryazanov, G. Ya. Opyty i modelirovanie pri izuchenii elektromagnitnogo polya (Experiments and Simulation in Electromagnetic Fields). — Izdatel'stvo "Nauka", Moskva. 1966.

V. V. Bogorodskii, G. V. Trepov, and B. A. Fedorov

APPLICATION OF LASERS TO STUDIES OF ICE DYNAMICS

Doppler-shift laser systems are currently available for high-accuracy measurements of small displacements /1/. Laser experiments are thus of considerable importance for studying the dynamics of glaciers. In particular, Doppler-shift laser systems are suitable for rapid and reliable measurements of the surface velocities of glaciers.

In conventional measurements, the surface velocity of a moving glacier is determined from the displacement of reference markers on the glacier surface, which is measured by geodetic methods. The geodetic equipment is mounted on a relatively firm bedrock. If the equipment is mounted on the glacier, geodetic measurements will only give the relative velocities of adjoining surface areas of the glacier. Since geodetic measurements are not very sensitive, and the surface velocities of glaciers are small, this technique requires very long time periods — months and even years. The application of the Doppler-shift laser system markedly reduces the time of measurement of surface velocities (whether absolute or relative) at one point, bringing it down to a few seconds or at most tens of seconds.

The technique of laser measurements amounts to the following. A laser mounted on a bedrock outcrop emits continuous coherent radiation in the general direction of a marker with a reflector, mounted on the glacier. The light reflected from the marker hits an optical detector. A reference signal from the laser is delivered to the same detector through a special channel. Because of the space and time coherence of the reflected and the reference signals, beats will form at the optical detector input, the phase of the reflected signal varying continuously relative to the phase of the reference signal as the glacier slips. The optical detector output is proportional to the intensity of the incident light with double the beating frequency.

Let $A_0 e^{j\omega_0 t}$ be the reference signal, $A_1 e^{j(\omega_0 - \omega_D)t}$ the reflected signal; here $\omega_D = \omega_0 - \dfrac{2V}{C}$ is the angular Doppler frequency, and V is the velocity of approach of the marker to the transceiver (i. e., the velocity of the glacier toward the transceiver).

For reference and reflected signals of equal intensity, the input signal is expressed by

$$\dot{E} = A e^{j\omega_0 t} + A e^{j(\omega_0 + \omega_D)t} = A e^{j\omega_0 t}\left(1 + e^{j\omega_D t}\right) = A e^{j\left(\omega_0 - \frac{\omega_D}{2}\right)t}\left(e^{\frac{-j\omega_D}{2}t} + e^{j\frac{\omega_D}{2}t}\right).$$

or, in real-number notation,

$$E(t) = 2A \cos\omega_D t \cos\left(\omega_0 + \frac{\omega_D}{2}\right) t = A(t)\cos\left(\omega_0 + \frac{\omega_D}{2}\right) t,$$

where the factor $A(t) = 2A \cos\omega_D t$ represents the variation of the amplitude of the reflected signals.

The input power

$$P(t) = \frac{1}{2} A^2(t) = A^2(1 + \cos 2\omega_D t)$$

varies between 0 and $2A^2$ with frequency $2\omega_D$.

The Doppler frequencies for a laser in the green region of the optical spectrum and for various velocities of glacier motion are listed in the table below:

Glacier velocity		Doppler frequency, Hz	Double the Doppler frequency, Hz
m/year	mm/sec		
1.58	$5 \cdot 10^{-5}$	0.1	0.2
15.8	$5 \cdot 10^{-4}$	1	2
158	$5 \cdot 10^{-3}$	10	20

We see from the table that in the case of a slowly slipping glacier (1.58 m/year), 10 output beats can be recorded in 10 sec.

In principle, even smaller velocities of glaciers can be recorded, down to a few centimeters annually, so that the method can be applied to measure relative velocities with the marker and the detector mounted on the surface of the glacier.
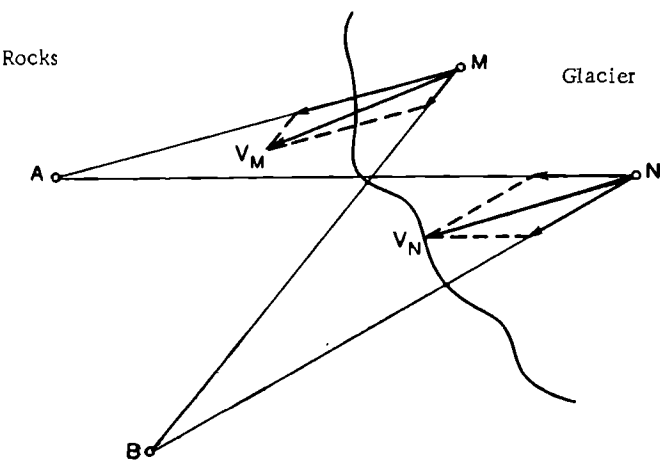
FIGURE 1. Charting the velocity of the glacier surface:

A and B   transceivers; M, N   points on the surface of the glacier.

This arrangement will yield a chart of the velocities of motion of individual points on the glacier surface by measuring the velocity components of each point with the aid of two separate transceivers mounted on bedrock outcrops (Figure 1). The velocity of each point is then found by vector addition of the two components.

The advantages of the method of laser measurements of glacier velocities (besides the exceptional reproducibility) include the easy detection of non-uniform motion of the glacier surface, associated with irregularities in the subglacial relief and with various glaciological and temperature factors.

A certain shortcoming of the method is the presence of seismic interference, which leads to incoherent vibrations of the receiver and the detector. In seismically quiet periods, however, the level of seismic noise is no more than $0.1 \cdot 10^{-3} - 0.2 \cdot 10^{-3}$ mm for detector-reflector separations of a few kilometers, and does not affect the normal operation of the system.

Bibliography

1. Birnbaum, G. Optical Masers. — New York, Academic Press. 1964.

M. N. Vitushkina

SOME EXPERIMENTAL RESULTS OF RADIOMETRIC PROBING OF GLACIERS

The approximate dependence of the antenna temperature at the radiometer receiver output on the electrical parameters of the medium and the viewing angle was established in /1/. The model of a plane-layered ice field was used to demonstrate that for viewing angles other than Brewster's angle, a semi-infinite crack with smooth vertical walls filling the main lobe of the antenna beam can be detected by a radiometric receiver with a sensitivity no worse than 1°K and a bandwidth of 1 Hz.

Moreover, the antenna temperature is expected to increase approximately by 6°K when this crak is viewed at 45° compared to the antenna temperature registered with an unbroken ice surface.

The present study had three principal aims:

1) development of a high-sensitivity radiometric receiver of small dimensions, small weight, and small power requirements;

2) simulation of broken and unbroken surfaces;

3) execution of measurements with targets lying close to natural cracks.

An S-range radiometer was designed. It comprised an antenna, a direct amplification radiometric receiver, and an output indicator.

The one-dish parabolic antenna with a horn ensured a sufficiently narrow beam with a low scattering coefficient in a wide frequency band. The direct amplification radiometric receiver used a simple modulation circuit, with a specially designed tunnel-diode microwave amplifier at the input. The radiometer sensitivity reached 0.7°K for output filter passband of 1 Hz. Special attention was paid to economic performance and small size. A standard potentiometer recorder was used as the output indicator.

The measurements were carried out under stationary conditions in various stations in summer 1967 and spring 1968.

The stationary measuring equipment comprised a parabolic antenna, a rotary mechanism, and a thermostated radiometer; the instruments were set up on an open platform at the top of a 5-m tower, to reduce the detection of heat radiation by the side lobes of the antenna. The rotary drive of the antenna made it possible to calibrate the radiometer using the radiation from the zenith and to alter the reception direction between altitude angles of -10 and $+120°$ in $2°$ intervals.

EXPERIMENTAL RESULTS AND DISCUSSION

Standard characteristics were provided by preliminary measurements of antenna temperatures for unbroken surfaces, such as planks, sawdust,

foam plastic, ice, and snow. To ensure comparable results independent of the particular surface used, the test materials were densely packed on a 3×6 m duralumin sheet at distances of 9 and 20 m from the antenna. This corresponds to viewing angles of 45 and 20°.
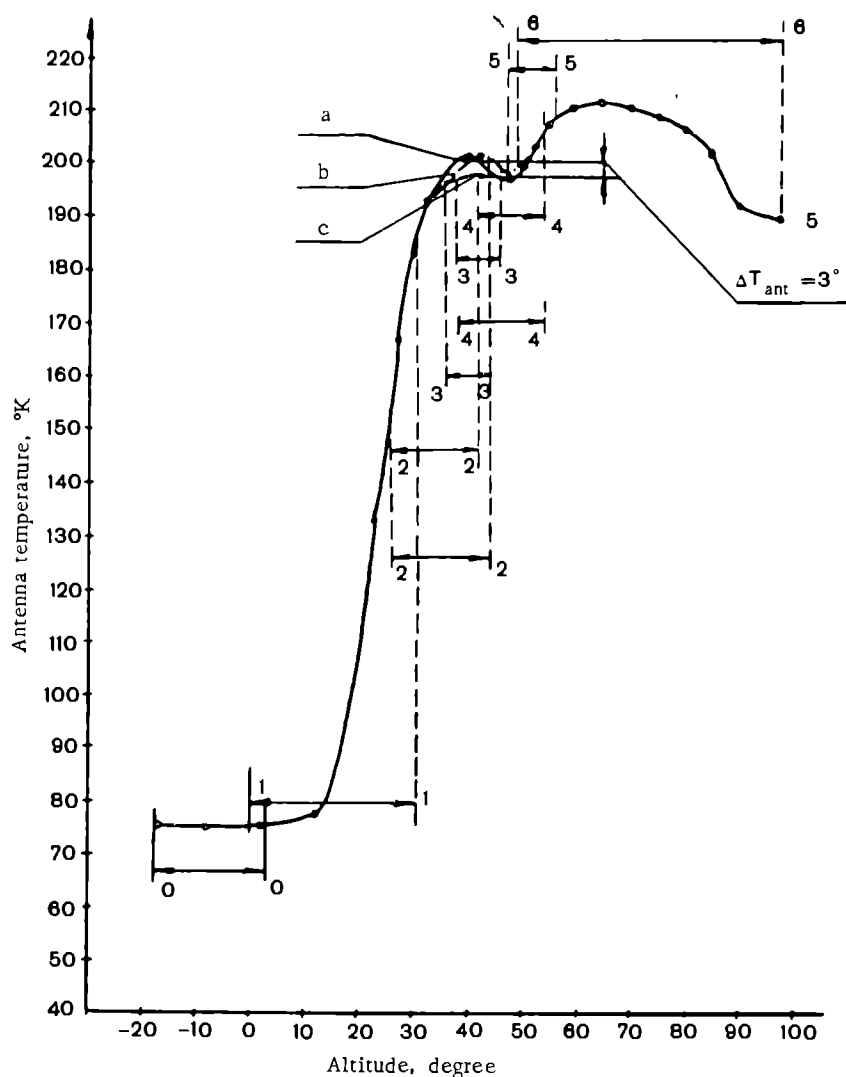
FIGURE 1. Antenna temperatures of various objects from the horizon to the experimental setup:

0—0) "sky"; 1—1) "before target"; 2—2) target before crack; 3—3) "crack"; 4—4) "target beyond crack"; 5—5) "front face"; 6—6) "beyond target". a symmetrical crack ($3 \times 0.5 \times 0.5$ m); b asymmetrical crack; c no crack.

As could be expected, the antenna temperature in each case was found to increase with the increase in the thickness of the specimen. The measurements show that the optical density increment of the various materials grows in the following order: snow—sawdust—foam plastic—ice—planks. Snow and sawdust, on the one hand, and ice and planks, on the other, display very close emissive properties in the S range.

The principal results were obtained in measurements using targets close to natural cracks. To permit comparing the antenna temperatures at the radiometer output from broken and unbroken ice surfaces, the 3 × 6 m measurement area was densely paved with smooth ice slabs measuring 0.8 × 0.8 × 0.5 m. This sample layer was then doubled to a height of 1.0 m. From targets 0.5 and 1.0 m high, some sample slabs were removed to simulate a crack perpendicular to the direction of reception, and measurement we made for various altitude angles for each target. The antenna temperatures were recorded with particular care for altitude angles corresponding to the target.
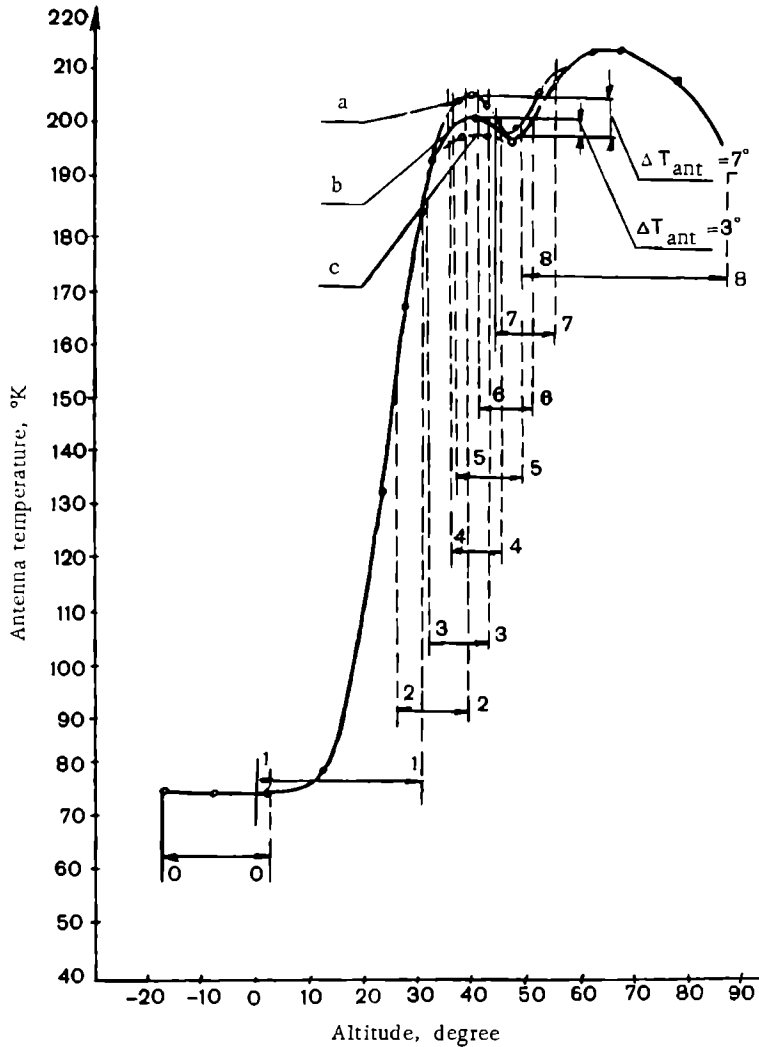
FIGURE 2. Variation of antenna temperature as a function of crack depth:

0—0) "sky"; 1—1) "before target"; 2—2) "target 0.5 m thick"; 3—3) "target 1 m thick"; 4—4) "1 × 0.5 m crack; 5—5) "target 1.0 m thick"; 6—6) "front face"; 7—7) "target 0.5 m thick"); 8—8) "beyond target". a 1.0 m crack; b 0.5 m crack; c no crack.

Let us consider in more detail the experimental results. The solid curve in Figure 1 gives the antenna temperature as a function of the altitude

angle for targets between the horizon and the foot of the measurement tower. The antenna temperature of each target was determined by the intrinsic radio brightness temperature of the target and the viewing angle. As the antenna was rotated, the output indicator registered the antenna temperature corresponding to the heat radiation of the sky $(0-0)$, the ice on Lake Ladoga $(1-1, 6-6)$, and the ice slabs packed on the test area $(2-2$ through $5-5)$. The general trend of the curve is mainly determined by the dependence of the emissivity on the altitude angle. The only exception is the section of the curve near altitude of 47°30', which may be associated with interference of direct and reflected radiation at the "lake ice—target ice" interface created by the finite height of the target. Reruns fully confirmed these results.

The dashed curve in Figure 1 corresponds to an ice monolith measuring $6 \times 3 \times 0.5$ m, with a smooth unbroken surface. The corresponding antenna temperature was 198°K.

A $3 \times 0.5 \times 0.5$ m crack with smooth walls in the monolith, at right angles to the direction of reception, raised the antenna temperature by 3°K. "Symmetric crack" and "asymmetric crack" in the figure describe crack propagation along the monolith. The antenna temperature increased in these cases also, but the effect corresponded to different viewing angles.

An attempt was made to increase the depth of the crack to 1 m. The walls of the crack were raised by packing another layer of ice slabs on top of the original layer. The resulting increase of the antenna temperature was 7°K, compared to the monolithic case (Figure 2).

To measure the increase in antenna temperature associated with the increase in crack width from 0.5 to 1 m, the height of the ice monolith had to be raised to 1.0 m. The $3 \times 1 \times 1$ m crack produced an antenna temperature increase of 8°K compared to the monolith temperature. The result is close to the computed figure of 6°K.

Figure 3 plots the antenna temperature as a function of position angles for targets on a distant test area, removed 20 m from the antenna. The corresponding range of altitude angles is between 14 and 24°. Section $2-2$ of the curve corresponds to a $6 \times 3 \times 1$ m ice monolith with a smooth unbroken surface. A crack of $3 \times 1 \times 1$ m with smooth vertical walls in the monolith oriented at right angles to the direction of reception, increased the antenna temperature by 7°K, and a crack of 1.8 m width raised the antenna temperature by 13°K.

The experiments lead to the following conclusions:

1) the radiometric receiver with 0.7°K sensitivity and 1 Hz passband will detect ice cracks 0.5—1.0 m wide, extending at right angles to the direction of reception at distances of 9 and 20 m from the antenna with viewing angles of 45 and 17°, respectively;

2) whenever the antenna beam intercepted the crack, an increase in antenna temperature was recorded at the radiometer output;

3) the minimum antenna temperature increment (3°K) was observed for ice with a crack 0.5 m wide;

4) the maximum antenna temperature increment (13°K) was observed for ice with a crack 1.8 m wide;

5) for a crack 0.5 m wide, the increase of crack depth from 0.5 to 1.0 m raised the antenna temperature increment from 3 to 7°K;

6) for a crack 1 m deep, the increase in crack width from 0.9 to 1.8 m raised the antenna temperature increment from 7 to 13°K.
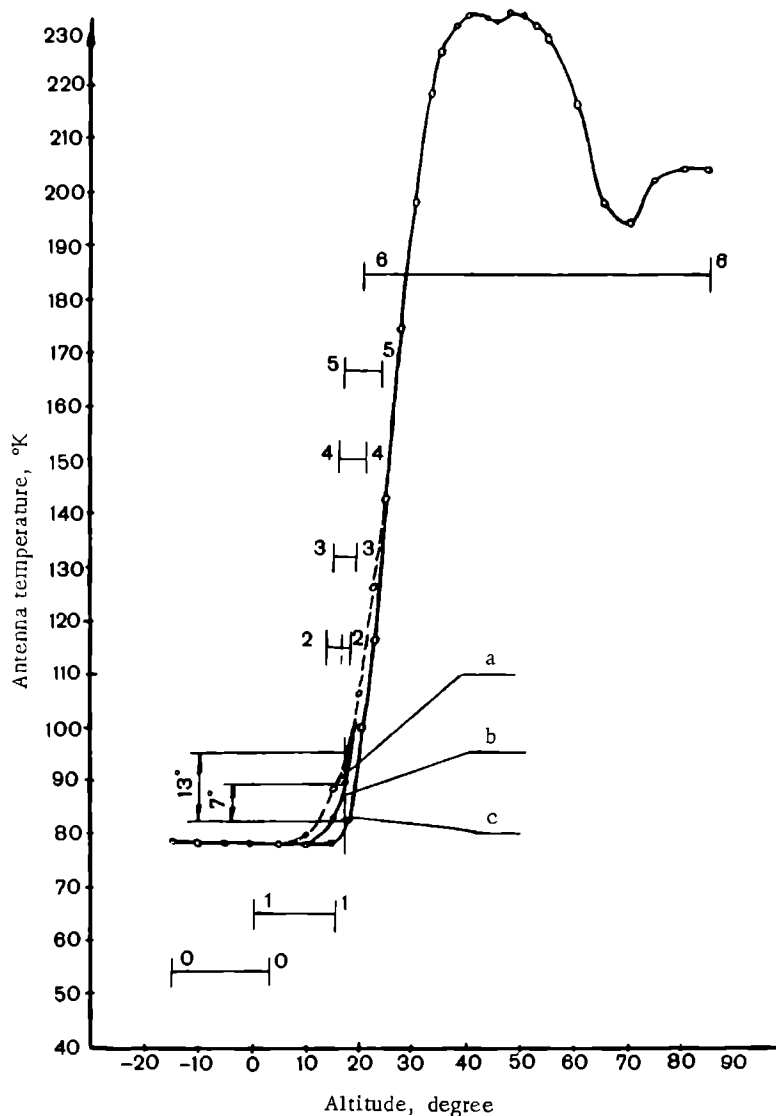

FIGURE 3. Antenna temperature as a function of crack width:

0—0) "sky"; 1—1) "before target"; 2—2) "target before crack"; 3—3) "crack"; 4—4) "target beyond crack"; 5—5) "front face"; 6—6) "beyond target". a 1.8 m crack; b 0.9 m crack; c no crack.

Bibliography

1. Bogorodskii, V. V. and M. N. Vitushkina. Passive Radar Probing of Glaciers. (See next article of this collection.).

V. V. Bogorodskii and M. N. Vitushkina

PASSIVE RADAR PROBING OF GLACIERS

The potential of active radar techniques for probing glaciers is well known. Recently, Soviet and American glaciologists have taken up the subject of passive radar probing of various ice formations.

The spectral density of the high-intensity microwave heat radiation is characterized by the radio brightness temperature. An approximate dependence of the radio brightness temperature on the electrical parameters of the radiating medium can be found by considering models of plane-layered ice fields with Fresnel reflection coefficients in the microwave region.

A model of an unbroken ice cover can be described as follows: a layer of snow of finite thickness (medium 2) overlying a half-space filled with ice 3. For simplicity medium 3 is assumed to be homogeneous and uniformly heated to temperature T_3. The brightness temperature of the radio emission of medium 3 into medium 1 (the atmosphere) therefore can be expressed in the form

$$T_{b_{31}} = T_3 (1 - R_{31}^2) \tag{1}$$

where T_3 is the thermodynamic temperature of medium 3, R_{31} is the reflection coefficient of electromagnetic energy from the plane interface $3-1$. The heat radiation of snow is ignored.
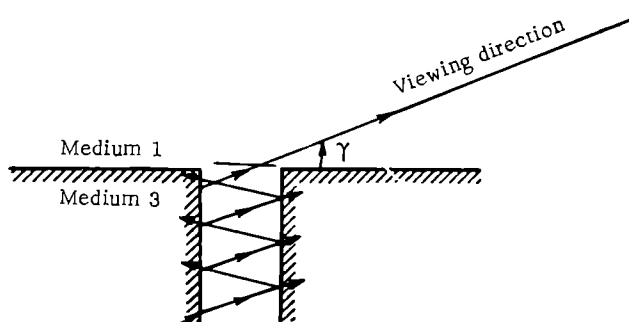
FIGURE 1.

Figure 1 shows a model of a crack of semi-infinite depth with smooth vertical walls in medium 3. As a result of multiple reflections of the radiation flux from the crack walls, the brightness temperature of the radiation emitted from medium 3 into medium 1 through the crack is equal

to the thermodynamic temperature of medium 3:

$$T_{b_{cr}} = T_3. \tag{2}$$

In other words, the crack emits blackbody radiation.

Comparison of (1) and (2) shows that the difference in the brightness temperatures of an unbroken and a broken surface of medium 3 is

$$\Delta T_b = T_{b_{cr}} - T_{b_{3\,1}} = T_3 R_{3\,1}^2. \tag{3}$$

Let us now consider the case when the radiating homogeneous unbroken medium 3 is separated from medium 1 by a layer of transparent medium 2 at temperature $T_2 = T_3$. The interface $3-2$ and $2-1$ are assumed to be plane, as before. In general, the following relation applies:

$$T_{b_{3\,2\,1}} = \frac{T_3 \left(1 - R_{32}^2\right) e^{-2\tau_2} \left(1 - R_{21}^2\right)}{1 - R_{21}^2 R_{32}^2 e^{-2\tau_2}}. \tag{4}$$

where R_{32}, R_{21} are the reflection coefficients of electromagnetic energy from the plane interfaces $3-2$ and $2-1$, respectively, τ_2 is the optical thickness of medium 2.

Calculations carried out for the case when medium 2 is a snow layer about 1.0 m thick and medium 3 is ice show that the flux attenuation due to absorption (τ_2) and multiple reflections at the interfaces (R_{21}^2, R_{32}^2) is negligible, and (4) may be written in the form

$$T_{b_{3\,2\,1}} = T_3 (1 - R_{32}^2)(1 - R_{21}^2). \tag{5}$$

Let us consider the case when the transparent medium 2 between media 3 and 1 fills the gap between the walls of a semi-infinite vertical crack in medium 3. The radio brightness temperature of the heat radiation from medium 3 into medium 1 is clearly expressed by the equality

$$T_{b_{3\,2\,1_{cr}}} = T_3 (1 - R_{21}^2). \tag{6}$$

Comparison of relations (5) and (6) shows that the difference in the brightness temperatures of a broken and an unbroken medium 3 is

$$\Delta T_{b_{3\,2\,1}} = T_3 R_{32}^2 (1 - R_{21}^2). \tag{7}$$

If the Rayleigh criterion

$$H_{irr} < \frac{1}{16 \sin \gamma}. \tag{8}$$

is satisfied for the surface irregularities H_{irr}, the electromagnetic energy reflection coefficients R_{21} and R_{32} in (1) through (7) are expressed by Fresnel's standard relations.

The noise temperature induced in the radiometer antenna by the heat radiation from the medium is expressed in terms of the so-called antenna

temperature

$$T_{ant} = \frac{D}{4\pi} \int_{4\pi} T_b(\varphi, \theta) F(\varphi, \theta) d\Omega, \tag{9}$$

where D is the antenna directivity coefficient, $F(\varphi, \theta)$ is the power directivity function of the antenna.

For simplicity, a loss-free antenna is assumed; the brightness temperature of the radiating medium is assumed to remain constant within the main lobe of the antenna pattern, and the radiation picked up by the side lobes is ignored. Then

$$\Delta T_{ant} = \Delta T_b. \tag{10}$$

FIGURE 2.

40
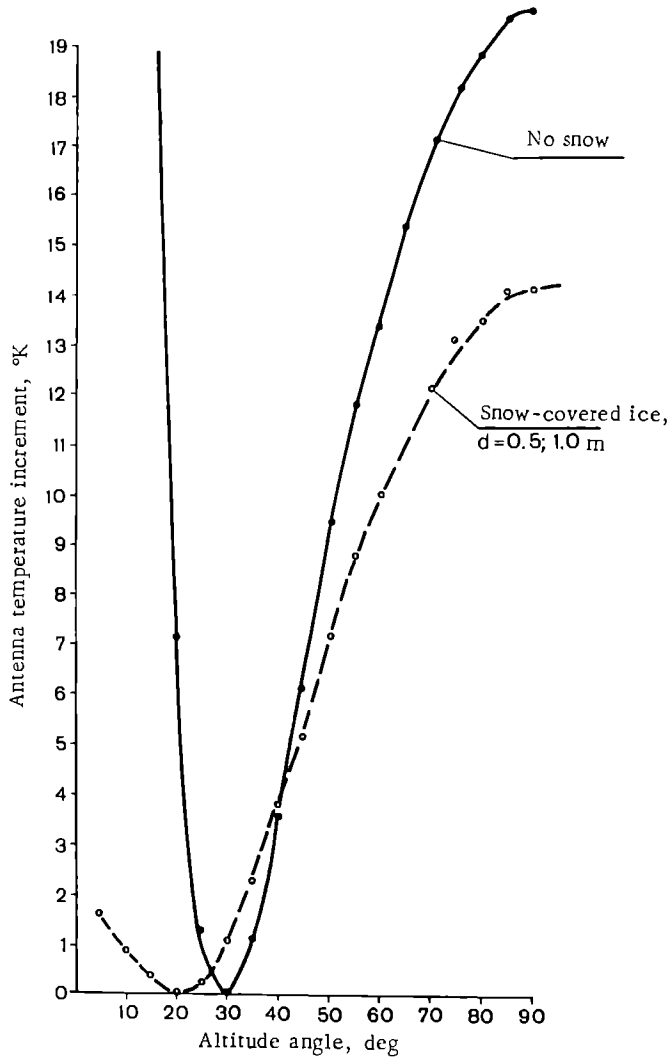
Inserting (7) in (10), we find

$$\Delta T_{\text{ant}} = T_3 R_{32}^2 (1 - R_{21}^2).$$ (11)

The different ΔT_{ant} in the antenna temperatures is registered by the radiometer input stage when the antenna is switched from the snow-filled crack to the unbroken ice surface, assuming that the crack filled the entire solid angle of the main lobe.

If the crack fills only part of the main lobe angle, we have

$$\Delta T_{\text{ant}}' = T_3 R_{32}^2 (1 - R_{21}^2) \frac{S_{\text{cr}}}{S_{\text{spot}}}.$$ (12)

It can be shown /1/ that if the width of the main lobe $\alpha \ll 1$, we have

$$\left. \begin{aligned} S_{\text{spot}} &= \frac{\pi r^2 \alpha^2}{4 \sin \gamma}, \\ S_{\text{cr}} &= l r \alpha = \frac{l h \alpha}{\sin \gamma}, \end{aligned} \right\}$$ (13)

where r is the distance from the antenna to the crack, h is the height of the antenna above the snow surface, l is the crack width.

The temperature differences $\Delta T_{\text{ant}} = f(\gamma)$ computed from (11) for 0.5 and 1.0 m snow thickness (dashed curve) and from (3) without snow (solid curve) are shown in Figure 2. The trend of the curves is mainly determined by the dependence of the square of the reflection coefficient of radiation from the ice — snow interface on the altitude angle.

A brief review of the theory leads to a number of conclusions:

For viewing angles other than Brewster's angle, a semi-infinite crack with smooth vertical walls filling the entire main lobe of the antenna may be detected radiometrically when the receiver sensitivity is no worse than 1°K.

The expected difference in the antenna temperature is 6°K when the crack is viewed at a 45° angle in two cases: (a) with 1 m of snow filling the crack and covering the surface above the crack and (b) without snow.

41

G. V. Trepov and G. P. Khokhlov

INTERFEROMETRIC MEASUREMENTS OF THE ELECTRICAL PARAMETERS OF THE ICE COVER IN THE METER WAVELENGTH RANGE

Radio interferometric methods recently proposed for measuring the thickness of floating ice /1/ require knowledge of the electrical parameters of ice. Analysis of the effect of irregularities on the top and the bottom surface of ice /2/ shows that meter wavelengths should be used in interferometric measurements of ice thickness. No reliable measurements of the electrical properties of ice have been carried out in this frequency range.

In winter 1968 we applied the interferometric method to determine the electrical properties of the ice cover on Lake Ladoga at frequencies between 60 and 180 MHz.

The reflection coefficient of a plane ice layer is known to be a periodic function of the ratio of the ice thickness to the wavelength in ice. The frequencies corresponding to the minima of the reflection coefficient are given by the relation

$$f_{min} = \frac{2n+1}{4} \frac{c_0}{h \sqrt{\varepsilon'}},$$ (1)

where c_0 is the velocity of light in vacuum; ε' is the relative permittivity of ice; h is the layer thickness, $n = 0, 1, 2, 3, \ldots$ Thus, if the ice thickness is known, we can readily find ε'.

The following apparatus was used in the Lake Ladoga measurements. Frame-type antennas were suspended at a height of 3 m above the ice surface, spaced 3.5 m from one another. An amplitude-modulated signal was emitted by an antenna driven by a G-4-7A generator. The receiving antenna signal was picked up by a R-313M receiver and delivered to oscillograph input. The power level at the generator output and the amplification of the receiver channel were maintained constant at all frequencies. The signal amplitude was read off the oscillograph screen.

The main object was to determine the frequency corresponding to the minimum reflection coefficient of the ice layer, to establish a correspondence between the measured frequency and theoretical results, and to assess the potential of the method of remote measurements of the electrical properties of ice in the meter wavelength range.

As ice thickness could not be increased (the measurements were made just before the onset of massive thaw), constant ice thickness of 61.5 cm was used in all measurements.

Figure 1 plots the corresponding curves. Curve 1 is the amplitude of the signal reflected from a 2×6 m sheet of aluminum on the surface of ice, and curve 2 represents the signal reflected by the ice layer. The minimum on curve 2 is evidently associated with the quarter-wave thickness of the ice layer. Between 110 and 180 MHz, the reflection coefficient of ice practically coincides with that of the aluminum sheet. The frequency $f = 70$ MHz corresponding to the minimum adequately fits the results of the theoretical formula and the available permittivity data at this frequency ($\varepsilon' = 3$ according to (1)).
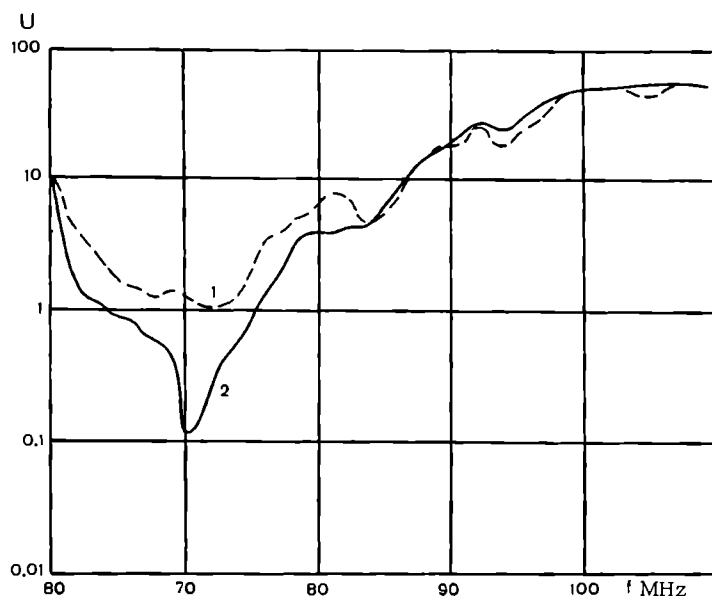
FIGURE 1.

This technique is not particularly accurate; it requires wide-band antennas and meets with certain difficulties because the antenna size is comparable with the antenna spacing and with the distance of the antennas from the ice. Another difficulty is that the antenna pattern is a function of frequency. However, the results obtained suggest that the interferometric method in the meter range can be used for measuring the electrical parameters of sweet-water and saline ice.

Bibliography

1. Bogorodskii, V. V. and V. N. Rudakov. Elektromagnitnye metody opredeleniya tolshchiny plavayushchikh l'dov (Electromagnetic Method of Measuring the Thickness of Floating Ice). — ZhTF, 32, No. 7. 1962.
2. Zubkovich, S. G. Vliyanie sherokhovatosti granits vozdukh—led i led—voda na effektivnost' radiotekhnicheskikh interferentsionnykh metodov opredeleniya tolshchiny l'da (The Effect of Air — Ice and Ice — Water Surface Irregularities on the Efficiency of Radio Interferometric Methods of Ice Thickness Determination). — Trudy AANII, Vol. 284. 1968.

B. Ya. Gaitskhoki

SPECTRAL TRANSMISSION OF SNOW AND
SOME ICE VARIETIES

The transmission of electromagnetic radiation in the optical spectrum by ice and snow is of the greatest importance for solving a number of theoretical and applied problems. So far, however, the characteristics of the transmission of optical radiation through ice and snow have been studied insufficiently. Experimental studies in this direction have made use of the actinometric technique only. The principal results of these studies are summarized in /1, 2, 3/.

Some fundamental shortcomings of the previous measuring technique are worth considering. A specimen in the shape of a plane-parallel plate was cut out from ice. One pyranometer was placed above the layer and the other below the layer. The measurements were made in natural light. The illumination reaching the side faces of the specimen could obviously affect the pyranometer placed under the layer, and the transmission coefficient obtained in these measurements was by no means the true coefficient.

Measurements of snow transmission in the visible spectrum using a selenium photocell were carried out according to the following procedure /1/. The selenium photocell fitted in a special frame was imbedded in snow at different depths. Simultaneous readings were taken for a photocell imbedded in snow and a photocell placed on the snow surface. The main shortcoming of these measurements is that the photocells are uncalibrated. As a result, the transmission coefficients were computed without regard to the nonlinearity of the light curve for certain load resistances and high light flux intensities.

The measurements were generally carried out without any regard to ice structure and composition or snow density.

We measured the diffuse transmission and reflection coefficients, τ and r, using a spherical photoelectric photometer. This is a two-beam photoelectric photometer with two photocells in a compensating circuit: one of the photocells is intended for actual measurements, and the other for compensation. A photometric sphere is provided in the measuring arm of the photometer; it integrates the incident flux, irrespective of its spatial distribution. The inclusion of the integrating sphere in the photometer makes it possible to measure the transmission coefficients of both transparent and scattering media. The instrument will measure the spectral coefficients τ and r between 360 and 1000 mμ. Twelve light filters are used with $\lambda_{ef} = 360$, 400, 445, 490, 540, 582, 607, 760, 839, 887, 935, 1000 mμ. The absolute error in the measurements of τ and r is $\pm 3\%$.

Some varieties of sweet-water and sea ice and snow were measured. The specimens were in the form of plane-parallel plates of fixed thickness with polished faces. All the plates were 20 mm thick. The specimens were cut from the parts of the core with characteristic texture, both at right angles and parallel to the freezing plane. The measurements of τ and r were supplemented by textural description of the core; the density and the salinity were determined; the crystal structure of the corresponding ice specimens was photographed. The snow samples were collected so as not to disturb the natural orientation and packing density of the grains. Measurements with sweet-water ice were carried out at the AANII refrigeration chambers, and with sea ice from SP-13f drifting station.
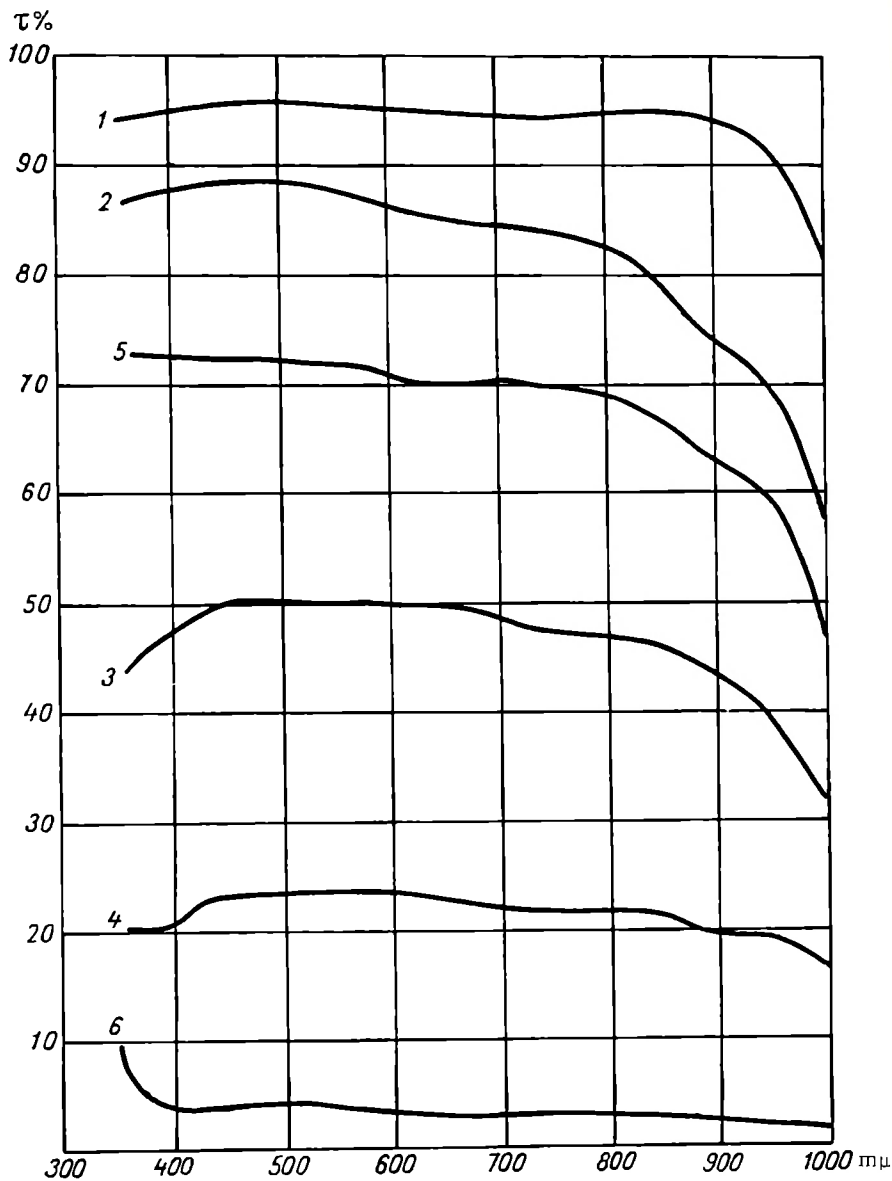
FIGURE 1. Spectral curves of the transmission coefficient.

Figure 1 shows the experimental curves plotting the transmission coefficients for individual characteristic specimens.

The measurements show that coarse-grained monolithic ice without any inclusions has $\tau = 95\%$ in the visible spectrum. As λ is raised to $1000\,m\mu$, τ drops to 80% (Figure 1, curve 1).

The reflection coefficient is around 4% in the entire frequency range. The density of this ice at $-16.4°$ is 0.9170.

Natural ice generally contains various inclusions. We used two highly characteristic varieties of sweet-water ice: ice with tubular air inclusions and so-called bubbly ice.

The tubular inclusions are greatly developed in the vertical direction, and they stretch in the form of tubes, cylinders, bubble tracks, and capillaries of about 1 mm cross section. Such ice texture is often encountered in river and lake ice, and also when snow flakes freeze on many-year sea ice. The density of this variety is 0.8948. In the visible spectrum, $\tau = =84-87\%$, and it is only at $\lambda = 1000\,m\mu$ that τ drops to 52% (Figure 1, curve 2). The reflection coefficient is $5-6\%$.

Bubbly ice is the least homogeneous in optical respect among all the sweet-water varieties. Our results refer to fine-bubbly ice with inclusions in the form of round and oval air bubbles less than 2 cm in diameter. This ice is very common: it forms when sludge and snow freeze, and also when ice formation occurs in choppy weather, so that thin young ice is broken and crushed. The density of these ice specimens was 0.8765. The transmission coefficient in the visible spectrum was around 50%, dropping to 32% in the near infrared (Figure 1, curve 3). For this ice, $r = 10-12\%$.

Measurements of sea ice of various ages show that it is always covered by a surface layer of bubbly ice with grained crystalline structure. In year-old and pack ice, this layer is generally characterized by low salinity and has numerous air inclusions. The surface layer of young ice is characterized by higher density than that of pack and year-old ice. Its salinity may vary between wide limits, depending on the salinity of the water from which it formed and the rate of ice formation. The surface layer of sea ice is characterized by the lowest transmission coefficient. For the surface layer of young ice, τ in the visible spectrum ranged between 30 and 40%, and for pack and year-old ice, between 20 and 30%. The spectral curve of the transmission coefficient for the surface layer of pack ice is shown in Figure 1 (curve 4). The reflection coefficient in the visible spectrum is around 15%, somewhat decreasing at longer wavelengths; for $\lambda = 1000\,m\mu$, $r = 10.5\%$.

In lower-lying layers, the commonest variety is ice with vertical filamental inclusions. The crystalline structure of this ice is mostly columnar-grainy or rod-filamental. The density of the corresponding samples ranged between 0.91 and 0.92, the salinity varying between 1 and 6 per mille. The transmission coefficient was between 60 and 80%. A characteristic spectral curve is shown in Figure 1 (curve 5). The values of r for ice of this texture were between 11 and 14%.

As we have noted above, the specimens for transmission and reflection measurements were cut perpendicular and parallel to the freezing plane. Comparison shows that the values of τ and r for specimens of the same texture are generally independent of orientation. In most cases, the difference for the two orientations does not exceed 10% for τ and about $3-5\%$ for r.

Measurements of snow samples with $\rho = 0.28\,g/cm^3$ gave transmission coefficients between 3 and 5%. The reflection coefficient in the visible was around 80%, and for $\lambda = 1000\,m\mu$, r dropped to 65%.

The transmission coefficients of various ice varieties thus range between wide limits, from 95 to 23% (in the visible). The reflection coefficients vary between 28 and 5% and less.

Note that the spectral transmission curves reveal certain features in common for all the ice varieties and snow. The variation of τ with wavelength in the visible spectrum is highly insignificant. It is only in the near infrared that the transmission coefficient decreases.

Bibliography

1. Kalitin, N. N. Proniknovenie sveta skvoz' sheg (Transmission of Light through Snow).— Problemy Arktiki, No. 3. 1939.
2. Chernigovskii, N. T. Radiatsionnye svoistva ledyanogo pokrova Tsentral'noi Arktiki (Radiative Properties of the Ice Cover in Central Arctic).— Trudy AANII, Vol. 253. 1963.
3. Koptev, A. P. and B. A. Pyatnenkov. O pogloshchenii i proniknovenii solnechnoi radiatsii v led i sneg v Arktike (Absorption and Transmission of Solar Radiation Through Ice and Snow in the Arctic).— Problemy Arktiki i Antarktiki, No. 10. 1962.
4. Savel'ev, B. A. Stroenie, sostav i svoistva ledyanogo pokrova morskikh i presnykh vodoemov (Structure, Composition, and Properties of Sea and Sweet-Water Ice).— Izd. MGU, Moskva. 1963.

B. Ya. Gaitskhoki

A PHOTOMETRIC MODEL OF THE SNOW-ICE COVER

The snow-ice cover on the surface of water bodies plays a leading role in the interaction of the water medium with the atmosphere. The transfer of optical radiation through snow and ice is of the greatest theoretical and applied importance. It is the radiant energy penetrating into the water through ice and snow that shapes the underwater luminous field, determines the biological productivity, the use of various optical systems for underwater (subglacial) vision, and affects a number of other applied problems.

From the photometric point of view, the snow-ice cover may be regarded to first approximation as a stack of plane-parallel light-scattering plates with different scattering properties.

The propagation of optical radiation through a photometrically homogeneous layer of ice (snow) is determined by the size, shape, concentration, and physical nature of the inhomogeneous inclusions and by the thickness of the layer. The solution of the problem should thus begin with the photometry of turbid media — the transmission of radiation through a light-scattering layer.

There are two alternative approaches to this problem. The first approach solves the appropriate integro-differential equation on the basis of a rigorous theory of radiative transfer, whereas the second approach simplifies the starting relations and introduces effective characteristics of the scattering medium, thus leading to a system of simple differential equations. This approach will be found in the work of Gurevich /1/ and Gershun /2/. We will concentrate on the second approach, as it yields in clear form the relevant physical dependences, although the first approach is evidently more rigorous and provides a more complete treatment of the mechanism of the effect.

The following assumptions are introduced:

1) the scattering medium is homogeneous;

2) the number of scattering centers is sufficiently high, so that differential methods are applicable;

3) the thickness of the plate is much less than its length and width, i.e., the light scattering layer may be regarded as limited by two infinite planes;

4) the plate is immersed in a non-scattering medium;

5) the plate is uniformly illuminated, and the conditions of illumination are therefore constant at all points at the same depth;

6) polarization effects are ignored;

7) selective scattering is ignored, i.e., monochromatic incident radiation is assumed.

Let dz be the thickness of an elementary plane-parallel lamina inside the scattering layer. Its reflection and transmission coefficients $r(dz)$ and $\tau(dz)$ are given by

$$\left. \begin{array}{l} r(dz) = k_1\, dz, \\ \tau(dz) = 1 - k_2\, dz. \end{array} \right\} \tag{1}$$

The coefficients k_1 and $k_2 \geqslant k_1$, expressed in units of reciprocal length, fully characterize the scattering medium under the above assumptions. In general, k_1 and k_2 depend not only on the properties of the scattering medium, but also on the spatial distribution of the incident radiation flux. The coefficients k_1 and k_2 introduced by Gurevich are related to the physical characteristics by the following expressions:

$$\left. \begin{array}{l} k_1 = \dfrac{E_0}{E}\, \varphi\sigma, \\[2mm] k_2 = \dfrac{E_0}{E}\, \varphi\sigma + \dfrac{E_0}{E}\, \varkappa = \dfrac{E_0}{E}\, (\varphi\sigma + \varkappa), \end{array} \right\} \tag{2}$$

where E is the surface illuminance of the layer, E_0 is the volume illuminance inside the layer, $\varkappa$ is the absorption index, σ is the scattering coefficient, φ is the fraction of the back-scattered flux.

The ratio of the volume to surface illuminance for a directional beam perpendicular to the layer is equal to unity. For a grazing beam $\dfrac{E_0}{E} = \infty$. If the layer is illuminated from one side by diffuse light, i.e., the light intensity is uniform in all directions within a solid angle of 2π, being equal to B, we have $\dfrac{E_0}{E} = \dfrac{2\pi B}{\pi B} = 2$.

Consider a plane-parallel plate of thickness z_0 made of scattering and absorbing material. The plate is horizontal and is uniformly illuminated from above. The illuminance of a surface at a depth z inside the layer is $E_1(z)$ from above and $E_2(z)$ from below. The luminous budget of an infinitesimal layer of thickness dz between the planes z and $z + dz$ is expressed by the following obvious relations (see Figure 1):

$$\left. \begin{array}{l} E_1(z + dz) = \tau(dz)\, E_1(z) + r(dz)\, E_2(z + dz), \\ E_2(z) = \tau(dz)\, E_2(z + dz) + r(dz)\, E_1(z). \end{array} \right\} \tag{3}$$

Inserting the transmission and reflection coefficients from (1) in (3), we obtain the differential equations

$$\left. \begin{array}{l} E_1' = -k_2 E_1 + k_1 E_2, \\ E_2' = -k_1 E_1 + k_2 E_2. \end{array} \right\} \tag{4}$$

The boundary conditions of our problem are

$$\begin{array}{l} E_1(0) = (1 - \rho) + \rho' E_2(0), \\ E_2(z_0) = \rho' E_1(z_0). \end{array}$$

where ρ is the reflection coefficient of a polished surface for radiation incident from the surrounding medium, ρ' is the reflection coefficient for radiation incident from inside.
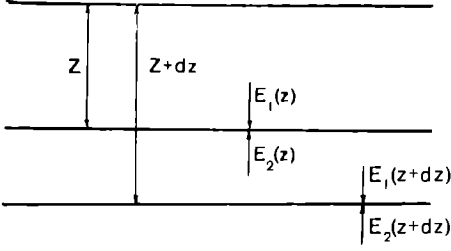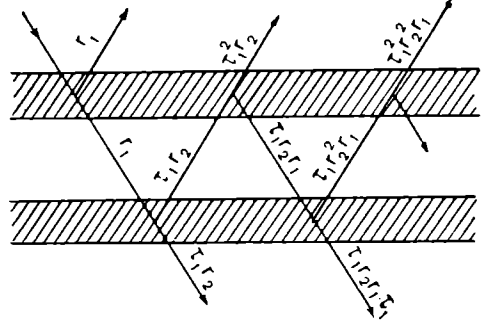

FIGURE 1.

FIGURE 2.

The solution of equations (4) in this case has the form

$$E_1(z) = \frac{1-\rho}{1-R\rho'} \cdot \frac{1 - R\dfrac{R-\rho'}{1-R\rho'} e^{-2L(z_0-z)}}{1-\left(\dfrac{R-\rho'}{1-R\rho'}\right)^2 e^{-2Lz_0}} \, e^{-Lz},$$

$$E_2(z) = \frac{1-\rho}{1-R\rho'} \cdot \frac{R\dfrac{R-\rho'}{1-R\rho'} e^{-2L(z_0-z)}}{1-\left(\dfrac{R-\rho'}{1-R\rho'}\right)^2 e^{-2Lz_0}} \, e^{-Lz} \qquad (5)$$

Here $L = \sqrt{k_2^2 - k_1^2}$, and $R = \dfrac{k_2 - L}{k_1} = \dfrac{\sqrt{k_2 + k_1} - \sqrt{k_2 - k_1}}{\sqrt{k_2 + k_1} + \sqrt{k_2 - k_1}}$.

The transmission and reflection coefficients of a plane-parallel layer in this case are given by

$$\tau = (1 - \rho') E_1(z_0) = \frac{1-\rho}{1+\rho'} \cdot \frac{1-\left(\dfrac{R-\rho'}{1-R\rho'}\right)^2}{1-\left(\dfrac{R-\rho'}{1-R\rho'}\right)^2 e^{-2Lz_0}} \, e^{-Lz_0},$$

$$r = \rho + (1 - \rho') E_2(0) = 1 - \frac{1-\rho}{1-\rho'}\left[1 - \frac{\dfrac{R-\rho'}{1-R\rho'}(1 - e^{-2Lz_0})}{1-\left(\dfrac{R-\rho'}{1-R\rho'}\right)^2 e^{-2Lz_0}}\right] \qquad (6)$$

Let $R_1 = \left|\dfrac{R-\rho'}{1-R\rho'}\right|$ and $M_1 = \ln R_1$. Then

$$E_1(z) = \frac{1-\rho}{1-\rho'}\left[\frac{\operatorname{sh}[M_1 - L(z_0-z)]}{\operatorname{sh}(M_1 - Lz_0)} \pm \rho' \frac{\operatorname{sh}L(z_0-z)}{\operatorname{sh}(M_1 - Lz_0)}\right],$$

$$E_2(z) = \frac{1-\rho}{1-\rho'^2}\rho\left[\frac{\operatorname{sh}[M_1 - L(z_0-z)]}{\operatorname{sh}(M_1 + Lz_0)} \pm \frac{\operatorname{sh}L(z_0-z)}{\operatorname{sh}(M_1 + Lz_0)}\right],$$

$$\tau = \frac{1-\rho}{1-\rho'} \frac{\operatorname{sh}M_1}{\operatorname{sh}(M_1 + Lz_0)},$$

$$r = 1 - \frac{1-\rho}{1-\rho'}\left|1 \pm \frac{\operatorname{sh}Lz_0}{\operatorname{sh}(M_1 + Lz_0)}\right|. \qquad (7)$$

The top sign in (7) corresponds to the case $R > \rho'$ (highly scattering medium), and the bottom sign to the case $R < \rho'$ (weakly scattering medium). Proceeding from the last relations, we see that our problem reduces to measurements of τ and r of various ice and snow varieties. From the coefficients τ and r of plane-parallel specimens of fixed thickness, we can compute the corresponding values of M_1 and L. In our case, when the scattering particles are suspended in the same medium with a constant value of n, ice and snow are best characterized by the constants R_1 and L. If a sufficient amount of experimental data is available, a photometric classification of ice and snow can be developed on the basis of R_1 and L. The results of the first experimental studies in this direction are presented in /3/.

We have thus derived expressions which enable us to compute transmission and reflection coefficients for a layer of ice (snow) of any thickness, assuming constant light-scattering properties throughout the layer.

To extend the results to multilayer systems, we will use the theory developed by Gurevich /4/, Genford /5/, and Kubelka /6/. According to this theory, the transmission and reflection coefficients of a system consisting of two plane-parallel scattering plates may be found by means of the simple constructions which are clear from Figure 2. If τ_1, r_1 and τ_2, r_2 are the transmission and reflection coefficients of the first and second layer, respectively, the total transmission coefficient is

$$\tau_{1+2} = \tau_1\tau_2(1 + r_1r_2 + r_1^2r_2^2 + \ldots) = \frac{\tau_1\tau_2}{1 - r_1r_2}. \tag{8}$$

The total reflection coefficient is

$$r_{1+2} = r_1 + \tau_1\tau_2r_2(1 - r_1r_2 + r_1^2r_2^2 + \ldots) = r_1 + \frac{\tau_1\tau_2r_2}{1 - r_1r_2}. \tag{9}$$

From the last equalities we readily derive an expression for the overall transmission and reflection coefficients of a stack consisting of any number of scattering plates:

$$\tau_{1+2+3+\cdots+n} = \frac{\tau_1\tau_2\tau_3 \ldots \tau_n}{1 - r_1r_2r_3 \ldots r_n}. \tag{10}$$

$$r_{1+2+3+\cdots+n} = r_1 + \frac{\tau_1 r_{2,3,\ldots,n}}{1 - r_1r_2r_3 \ldots r_n}. \tag{11}$$

Our photometric model of the snow-ice cover is clearly a first approximation. However, it yields adequate results for a wide range of practical problems.

Bibliography

1. G u r e v i c h, M. M. — Trudy GOI, No. 57:1—18. 1931.
2. G e r s h u n, A. A. Izbrannye trudy po fotometrii i svetotekhnike (Collected Works on Photometry and Illumination Engineering). — Gosudarstvennoe izdatel'stvo fiziko-matematicheskoi literatury, Moskva. 1958.

3. Gaitskhoki, B. Ya. — See this collection, p. 44.
4. Gurevic. — Physik. Z., **31**:753. 1930.
5. Benford, F. — Journal of the Optical Society of America, Vol. 44, No. 4. 1954.
6. Kubelka, P. — Journal of the Optical Society of America, 44, No. 4. 1954.

G. V. Trepov

MEASURING THE VELOCITY OF PROPAGATION OF ELECTROMAGNETIC WAVES IN A GLACIER

Measurement of the electromagnetic properties of ice under natural conditions, in the interior of a glacier, is one of the main problems of the electrophysical research in the Antarctic. Special emphasis is placed on the velocity of propagation of electromagnetic waves in a glacier, since radar techniques are currently used for probing glaciers and particularly for determining their thickness.

The velocity of propagation of electromagnetic waves in a glacier was measured in 1969 near the Molodezhnaya Soviet Antarctic station. The measurements were carried out by the method of slanted probing. The principle of this probing method is shown in Figure 1. Point A is a receiving antenna with a receiver and a recorder; a transmitting antenna with a pulse transmitter is set up at a distance l from it, at point B. Each transmitter pulse produces two pulses in the receiver: one pulse which traveled a distance 1 through air, and another which bounced off the glacier substrate and reached the detector after traveling a distance s inside the glacier (in Figure 1, point A' is the mirror image of point A relative to the glacier substrate). Measuring the delay of the second signal relative to the first signal for various transmitter — receiver separations l, we find the velocity of propagation of the radio waves from obvious geometrical considerations:

$$\frac{t_s^2 c^2}{\varepsilon_{ice}} = h^2 + l^2, \qquad (1)$$

where h is double the glacier thickness at the point of reflection, $c = 300\,\mathrm{m}/\mu\mathrm{sec}$ is the electrodynamic constant, ε_{ice} is the permittivity of ice, $\dfrac{c}{\sqrt{\varepsilon_{ice}}}$ is the velocity of propagation of radio waves in ice; t_s is the time of propagation of the radio waves from the transmitting antenna to the receiver traveling inside the glacier.

By (1)

$$t_s^2 = \frac{\varepsilon}{c^2}\, l^2 + \frac{\varepsilon}{c^2}\, h^2, \qquad (2)$$

i.e., the square of the propagation time of a radio pulse from the transmitting antenna to the receiver is a linear function of the square of the length l, and the slope $\dfrac{\varepsilon}{c^2}$ of the straight line is equal to the reciprocal of the square of the propagation velocity of electromagnetic waves in ice.

53

The determination of the propagation velocity of radio waves in ice thus reduces to finding the experimental dependence $t_s^2 = F(l^2)$, fitting the experimental dependence with a straight line, and determining the slope of the best-fit line. The time t_s is found as the sum of the delay time t_d of the pulse propagating inside the glacier relative to the pulse propagating in air plus the propagation time $t_l = \frac{l}{c}$ of the radio pulse through air; the distance l is measured.
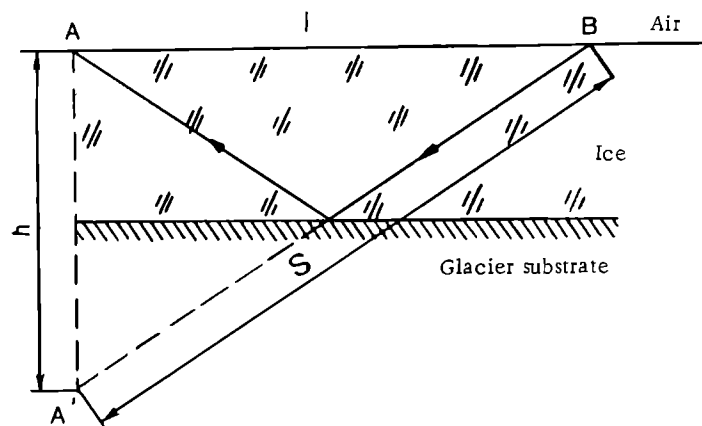

FIGURE 1. Diagram illustrating the propagation of radio waves in slanted probing of a glacier.

In practice, the measurements are carried out as follows. The receiving equipment is mounted in a small hut on a sled. This sled, and the sled with the transmitter, are moved symmetrically apart on the two sides of a marked straight-line traverse, so that the reflecting subglacial area remains the same during the measurements. The reflected pulse delay is measured every 50 m. Reconnaissance measurements of glacier thickness are carried out before the actual tests, and the area for reflection tests is chosen on the basis of these measurements.

The results obtained for one measurement point are summarized in Table 1.

TABLE 1.

l, m	0	50	100	150	200	250	300	350
t_d, μsec	2.25	2.0	1.85	1.72	1.7	1.7	1.75	1.83
t_l, μsec	0	0.165	0.33	0.5	0.66	0.83	1.0	1.165
t_s, μsec	2.25	2.165	2.18	2.22	2.37	2.53	2.75	2.995
l^2, m²/10^{-4}	0	0.025	1	2.25	4	6.25	9	12.27
t_s^2	5.08	4.7	4.75	4.93	5.41	6.4	7.57	8.95

The slope of the straight line $t_s^2 = F(l^2)$ was determined from Table 1 using the least squares method. We know /1/ that in case of linear dependence between two random variables x and y, the slope of the straight line fitting the experimental dependence $y = a + bx$ by the least squares method is

expressed by the equality

$$b = r \sqrt{\frac{\overline{(y-\bar{y})^2}}{\overline{(x-\bar{x})^2}}}, \qquad (3)$$

where

$$r = \frac{\overline{xy} - \bar{x}\,\bar{y}}{\sqrt{\overline{(x-\bar{x})^2}\,\overline{(y-\bar{y})^2}}} \qquad (4)$$

is the correlation coefficient,

$$\overline{xy} - \bar{x}\,\bar{y} = \sum x_i y_i - \frac{1}{n}\sum x_i \sum y_i, \qquad (5)$$

$$\overline{(x-\bar{x})^2} = \sum y_i^2 - \frac{1}{n}\left(\sum y_i\right)^2. \qquad (6)$$

$$\overline{(y-\bar{y})^2} = \sum x_i^2 - \frac{1}{n}\left(\sum x_i\right)^2. \qquad (7)$$

n is the number of experimentally measured points.

An auxiliary table is used in computing the slope of the straight line (Table 2).

TABLE 2.

i	1	2	3	4	5	6	7	Σ
$x_i = t^2 \cdot 10^{-4}$	0.025	1	2.25	4	6.25	9	12.27	34.8
$y_i = t_x^2$	4.7	4.75	4.93	5.41	6.4	7.57	8.95	42.7
x_i^2	0	1	5.07	16	38.1	81	152	293.2
y_i^2	22.1	22.6	24.2	29.3	41.1	57.3	80.1	276.7
$x_i y_i$	0.1	4.75	11.1	21.6	40	63.1	109.9	250.6

From Table 2 and expressions (7), (6), (5), (4), (3) we have $\overline{(x-\bar{x})^2} = 120.3$, $\overline{(y-\bar{y})^2} = 15.5$, $\overline{xy} - \overline{xy} = 38.5$, $r = 0.91$, $b = 0.317 \cdot 10^{-4}$. The result $b = 0.317 \cdot 10^{-4}\,\mu\text{sec}^2/\text{m}^2$ corresponds to velocity of propagation of 176 m/μsec in ice.

According to the results of measurements at other points, the propagation velocity of radio waves in ice is 180, 160, and 158 m/μsec. These propagation velocities are close to the figure computed using the standard permittivity of ice, 167 m/μsec.

Bibliography

1. Pustyl'nik, E. I. Statisticheskie metody analiza i obrabotki nablyu-
denii (Statistical Methods of Analysis and Processing of Observa-
tions). — Izdatel'stvo "Nauka", Moskva. 1968.

A. I. Galkina and V. A. Spitsyn

MEASURING THE TEMPERATURE OF THE SURFACE OF WATER, SNOW, AND ICE WITH A RADIATION THERMOMETER

Airborne tests of a radiation thermometer were carried out in October 1968. Their aim was to establish the applicability of this thermometer to remote measurements of the ground temperature. The tests were carried out in the Kara Sea with the aircraft flying above various surfaces: water, ice, dry land. Meteorological stations provided reference data on the temperature of these surfaces. In addition to that, the surface temperature of the Severnaya Zemlya glaciers was measured, and the glacier thickness was determined simultaneously by radar.

Figure 1 is a specimen recording of the surface temperature obtained with a radiation thermometer along the route extending from Vize Isl. to Srednii Isl. The recording characterizes the variation of the sea surface temperature as a function of the state of the ice cover. The numerical values are summarized in Table 1.

TABLE 1.

Vize Isl.	Fast ice	Nilas	Snow covered ice field	Air temperature (from meteorological data)
−11°	−10.4°	−4.8, −5°	−10°	−12.1°

TABLE 2.

Region, date		Temperature				
		air	water	snow surface	ice surface	soil surface
Peschanyi Isl. 13 Oct. 1968	Meteorological	−3.9	−1.8	−4.0	−4.0	−4.0
	Radiation thermometer	—	−1.6	—	−3.4	−3.8
Cape Zhelaniya 14 Oct. 1968	Meteorological	−8.0	−1.8	−8.0	—	−7.6
	Radiation thermometer	—	−1.6 to −1.8	—	—	−8.0 to −7.6
Vize Isl. 14 Oct. 1968	Meteorological	−12.1	−1.9	−11.3	−11.0	−11.3
	Radiation thermometer	—	—	—	fast ice −10.6	−11.2 to −11.3

N o t e: The radiation thermometer registered the temperature of snow-covered ice and soil.
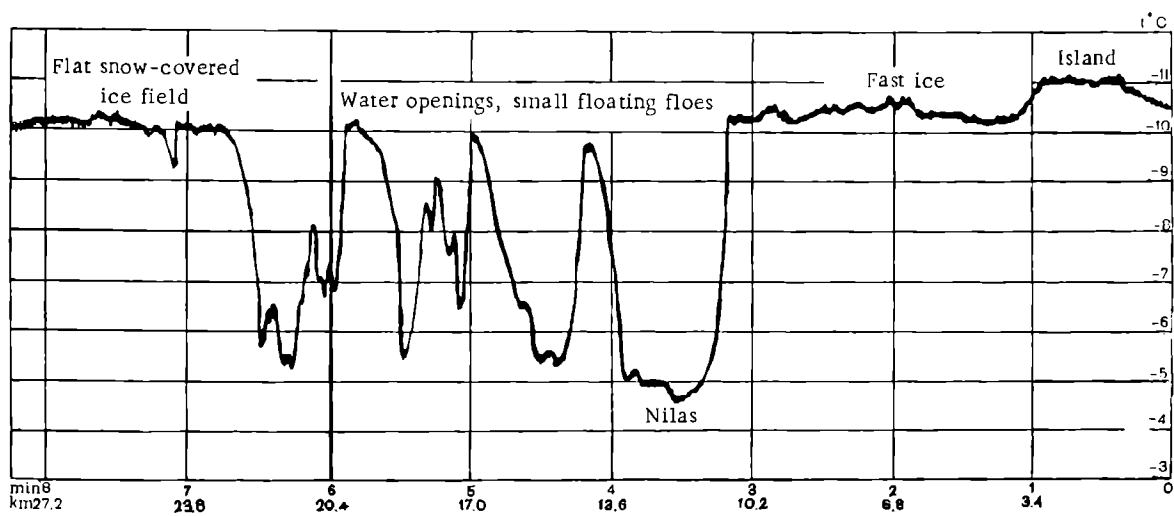
FIGURE 1. Specimen oscillograms of the radiation thermometer (route extending from Vize Isl. to Srednii Isl., 14 October 1968, flight altitude 200 m).

Table 2 lists the ground temperatures as measured with a radiation thermometer during flights above Peschanyi Island, Vize Island, and Novaya Zemlya (Cape Zhelaniya). Meteorological data are also given.

We see from the table that the meteorological data differ by 0.2 — 0.4° from the results obtained with a radiation thermometer. Note that the soil temperatures obtained over Peschanyi Isl. and Vize Isl. were perfectly reproducible.
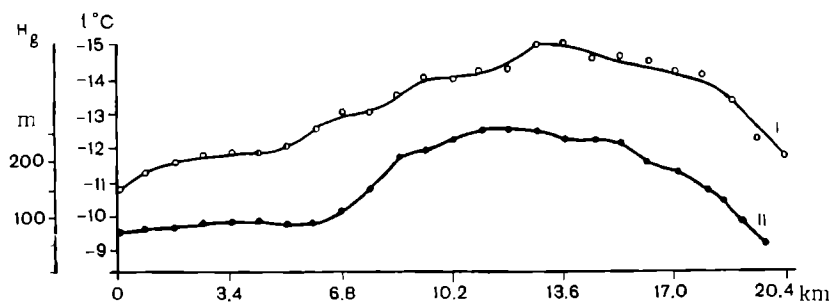
FIGURE 2. Surface temperature of the glacier (I) and the thickness of the glacier (II) from a flight over the Ushakov glacier (15 October 1968).

As we have noted before, flights above the glaciers of Novaya Zemlya provided both surface temperature measurements and radar measurements of the ice thickness. Figure 2 plots the curves of glacier thickness and glacier surface temperature. A good correlation is observed between the two factors.

Analysis of the results obtained in these tests shows that the radiation thermometer is quite suitable for collecting continuous information on the surface temperature of water, ice, and snow, which is greatly needed for oceanographic work.

57

BRIEF DESCRIPTION OF THE INSTRUMENT

The radiation thermometer tested in these flights is distinguished from the standard GGO and LITMO (LO GOIN) radiation thermometers in its smaller size and simpler operation. An original and attractively simple optical unit has been developed; the electronics is solid state. A block diagram of the radiation thermometer is shown in Figure 3.

The infrared heat emission of the scanned object enters through a barium fluoride (BaF_2) window 2, where it is focused by a plane-convex germanium lens 3 (12 mm diameter, 9 mm focal distance) onto the bolometer 6. An indium antimonide (InSb) filter mounted in front of the bolometer defines the desired wavelength range together with the entrance window and the germanium lens, $8-13.5$ μ. The incoming infrared radiation is modulated by chopper 1 before entering the window; this chopper is made of polished aluminum and modulates the incoming flux with a frequency of $30-35$ Hz. The chopper disk is driven by a DPM-20 electric motor (12).
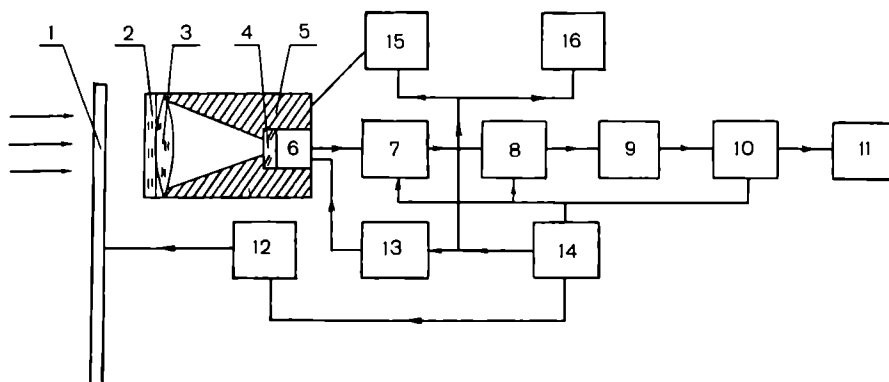
FIGURE 3. Block diagram of the radiation thermometer.

When the incoming flux is cut off by the chopper, the bolometer receives the radiation of the conical cavity around the reference source 5 reflected by the metallic surface of the chopper 1 (the bolometer is mounted at the apex of this conical cavity). The difference flux between the bolometer and the standard source (SS) in this position is expressed by the equality

$$\Delta W_1 = W_{ss} K_c + W_c (1 - K_c) - W_{bol}.$$

where W_c is the energy radiated by the chopper, K_c is the reflection coefficient of the chopper.

When the chopper transmits the incident flux, the difference energy flux is given by

$$\Delta W_2 = W_{object} - W_{bol}.$$

The chopper disk is made of polished duralumin. It has $K = 0.96 - 0.97$ and is mounted in an enclosed space. The heat emission of the disk thus may be ignored with fair accuracy. The amplitude of the variable radiant energy flux which produces an electric signal is then expressed by the equality

$$\Delta W = W_{ss} - W_{object} .$$

The variable electric signal generated in the bolometer is delivered to a low-noise transistor amplifier 7 and 8 and onward to the detector 9. The rectified voltage, whose magnitude is proportional to the temperature of the object, is delivered to an RC filter and to the null-recorder (10). A pen-and-ink potentiometer (11) with a 1—10 mV scale and 1 sec time constant is used as a recorder.

The thermal stabilization systems 15 and 16 maintain the temperature of the reference source at $+35°\pm0.1°C$ and heat the body of the measuring head to a constant temperature of 30°C. The power supply blocks 13, 14 provide the stabilized voltage needed for normal operation of the instrument. A BKM-5 semiconductor bolometer is used as the IR detector in the instrument.

Main technical specifications

Temperature range . . . . from — 20°C to + 20°C
Resolution . . . . no less than 0.2°C
Recorder time constant. . . . . 2.5 sec
                                       7°
Size:
      measuring head . . . . 150×130×350 mm
      control unit . . . . 310×300×190 mm
Weight . . . . 10 kg
Supply voltage . . . . d.c., 27 V

E. A. Martynova and V. A. Spitsyn

SOME RESULTS OF TESTS OF INFRARED SCANNERS
FOR HEAT CHARTING OF POLAR REGIONS

Every physical object emits electromagnetic radiation. The exact frequency or spectral composition of this radiation is determined by the relevant microprocesses in the object (internal and external electron transitions, vibrational and rotational motion of molecules, lattice vibrations, etc.). IR radiation, in particular, is emitted in transitions between different vibrational and rotational states of a molecule: electron transitions do not emit at these frequencies. The vibrational and rotational states of a molecule change as a result of random thermal fluctuations. It is thus evident that a direct relationship exists between the temperature of the object and its IR radiation. Planck's equation establishes a relationship between blackbody radiation intensity and temperature in any wavelength interval:

$$E = \int_{\lambda_1}^{\lambda_2} \frac{2hc^2}{\lambda^5} \frac{1}{e^{\frac{hc}{\lambda kT}} - 1} \, d\lambda.$$

No ideal blackbody radiation exists in nature. The "degree of blackness" of an object is characterized by its emissivity, which in general is a function of wavelength, temperature, and state of the surface. The IR radiation of an object is thus determined by its temperature and emissivity. By detecting the IR radiation from objects, we can therefore solve the "inverse" problem, namely determine the surface temperature distribution of the object or "take" a heat chart of its surface.

Temperature resolution of the measuring IR equipment is one of the important factors to be considered in heat charting of surfaces. The instrument obviously is expected to distinguish between different parts of the surface only if there is a sufficient temperature gradient or a noticeable difference in emissivity between them. The temperature contrast should not be less than the threshold value ΔT_{min} of the measuring equipment, i.e., the minimum detectable temperature difference. ΔT_{min} is not an instrumental constant: it depends on the properties of the radiating surface — its temperature and emissivity — as well as the instrumental parameters. The computation of ΔT_{min} of an ice surface between 0 and $-40°C$ shows that the minimum detectable temperature difference steeply increases at low temperatures (Figure 1).

In autumn 1968, an IR scanner was tested from aircraft over the Kara Sea and the Severnaya Zemlya glaciers: it recorded the heat chart of the ice—water surface, and this chart was subsequently processed.

Specifications of IR scanner

1. Wavelength range — $3.4 - 5.4 \mu$
2. Receiver—cooled photoresistor — (InSb)
3. Elementary angle of view — 1.6×10^{-5} sterad
4. Angle of view of one scanning line — $68°$
5. Effective objective area — $109 \, cm^2$
6. Objective focal distance — $253 \, mm$
7. ΔT_{min} for $-20°C$ — $0.26°C$
8. Amplification channel gain — 10^3
9. Amplifier passband — $8 \, Hz - 100 \, kHz$ (2 dB nonuniformity)
10. Power requirements — $1.2 \, kW$
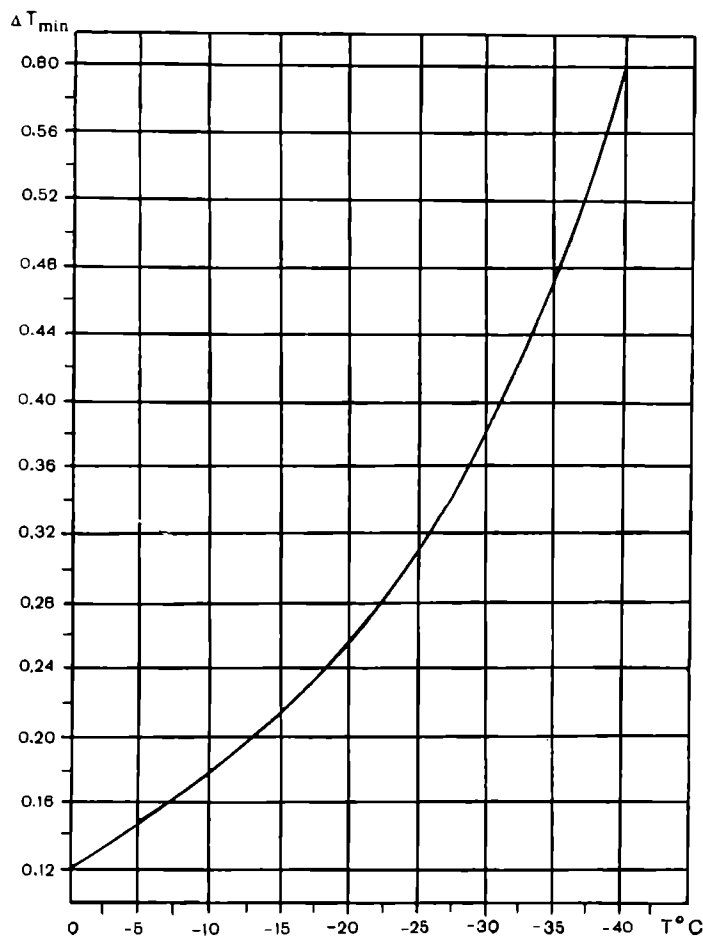
FIGURE 1. The detectable temperature threshold ΔT_{min} vs. surface temperature.

A new cooling system based on the Joule—Thomson effect (cooling of gas by adiabatic expansion) was first tried with the IR scanner.

Nitrogen compressed at 120—160 atm in a cylinder was fed through a capillary and a special filter to an expansion chamber, with the photoresistor fixed to its outside wall. The gas abruptly expanded absorbing heat and

61

condensed into a liquid with constant boiling-point temperature (77°K). The "spent" gas was then released from the system.

This cooling technique eliminated the need for transporting and storing large quantities of liquid nitrogen—a conventional coolant—in the Arctic.

Heat charts of different types of water—ice surface were taken during flights above the Kara Sea. The equipment was adjusted so that the photograph (Figure 2) presented a visually meaningful picture, i.e., water against the background of gray-white ice registered in the form of black bands and spots.

Analysis of the heat charts led to the following results:

1) the water—ice boundary (and especially the water—dry land boundary) is always very sharp. This applies both to water—white ice combinations (with surface temperature difference of up to 10°C) and to water—nilas combinations, where the temperature difference is very small;

2) ice of different ages (i.e., different thickness and temperature) is easily distinguishable. The heat chart clearly shows nonuniform dark-gray areas with spots of clear water—sludge and nilas. Gray ice (up to 15 cm thick) appears to be lighter than nilas. Gray-white ice (15—30 cm thick) corresponds to even lighter, possibly white, areas;

3) the coast shows on the photographs as a lighter (colder) area against the ice background;

4) night photographs lead to the same conclusions regarding the underlying surface as IR charting in daytime.

FIGURE 2. Heat chart of one of the areas of the water—ice surface of the Kara Sea.

Flights over the Severnaya Zemlya glaciers yielded IR information about cracks in ice (Figure 3). The photograph clearly shows cracks in the continuous ice area. Unfortunately, no airborne survey photographs were available to decide whether the IR scanning showed only visible crevasses or also revealed hidden cracks covered by snow. The snow-covered cracks, in principle, should show on the IR photographs because of the difference in temperature between the continuous ice cover, hidden under the snow, and the air volume of the crack.
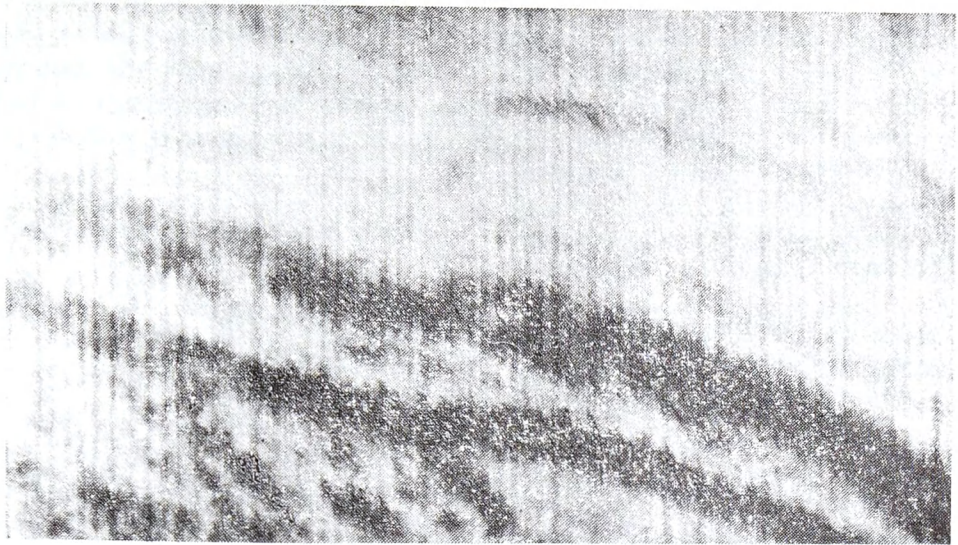
FIGURE 3. IR photograph of crevasses in Severnaya Zemlya glaciers (Albanov Glacier).

In conclusion note that the tests of IR scanning equipment in the Arctic yielded valuable thermal information about the state of the ice-covered sea surface and insular glaciers. The tests also proved the high quality of the IR equipment and the adequacy of the IR detector cooling system.

G. P. Khokhlov

RESULTS OF EXPERIMENTAL MEASUREMENTS OF THE ELECTRICAL PARAMETERS OF ARCTIC SEA ICE AT FREQUENCIES BETWEEN 100 Hz AND 1 MHz

Sea ice in general, and drifting Arctic ice in particular, are important geophysical objects whose physical properties have been largely neglected so far. The electrical properties of sea ice, for example, have hardly been studied. The importance of the experimental measurements of the electrical parameters of sea ice stems from two basic factors. First, accurate knowledge of the electrical properties of sea ice is absolutely essential for the application of a wide range of radio-physical methods of research in the Arctic and the Antarctic. Second, a consistent theory of polarization of sea ice can be developed only on the basis of experimental data, because of its great complexity. In view of the importance attached to the electrical properties of sea ice, methods should be devised for appropriate measurements in the low-frequency range, where the processes responsible for the difference in the electrical properties of saline ice and sweet ice are the most prominent.

No complete picture of the variation of the electrical properties of sea ice in a wide range of frequencies, temperatures, salinities, and other physical parameters can be reconstructed at this stage, as the corresponding studies were very few in number and mostly dealt with synthetic ice. For example, no data are given in /1/ on the permittivity and the loss angle of sea ice at frequencies below 100 kHz in a wide range of ice temperatures, and in /2/ data for high temperatures and low frequencies are conspicuously missing. Marked changes in the permittivity (10^6) of artificially prepared sea ice at $-22°C$ are reported in /3/ on the basis of Addison's unpublished results (measurements between 20 Hz and 50 MHz). The permittivity of natural sea ice of various ages at various temperatures is given in /4/, but there is no indication of the frequencies at which the measurements were carried out. Comparison of the electrical characteristics of sea ice from these sources and from /5/ reveals substantial discrepancies in the measurement results of different authors.

The present report describes the results of experimental measurements of the electrical properties of drifting sea ice carried out in 1965 — 1966 on the SP-13 drifting research station.

§1. MEASUREMENT PROCEDURE

The measurements were carried out using samples from various depths in young and pack ice. As a result, ice samples of different structures

with widely varying salinities were studied. Three-electrode plate capacitors from 30 to 90 mm in diameter were used; the nickel-plated electrodes were frozen onto the ice sample. The capacitor was mounted in a holder, which doubled as the stopper of a wide-necked vacuum flask. The ice sample was first cooled in a draft of air to the ambient temperature and the measurements were then carried out with gradually increasing temperature of the sample. The temperature was measured to within ± 0.2°C with a thermistor frozen under the capacitor guard ring and connected in the diagonal of the thermometer bridge. The uniformity of temperature distribution inside the capacitor was determined by simultaneous temperature measurements at several points inside the sample. The temperature distribution was found to be uniform within the experimental margin of error, for a temperature difference of 1 — 3°C between the sample in the vacuum flask and air.
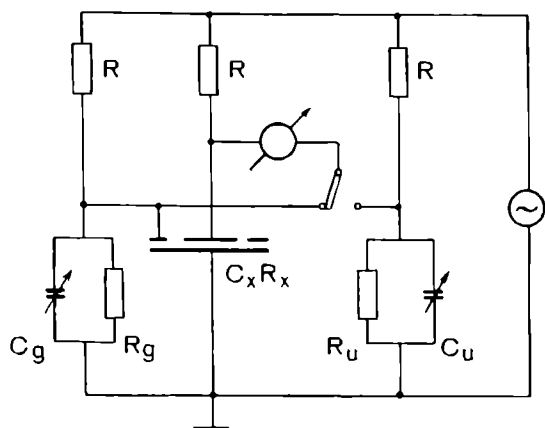
FIGURE 1.

The electrical parameters of ice were measured with two bridges covering the frequencies from 100 Hz to 1 MHz. A simplified circuit diagram of the bridges is shown in Figure 1. In addition to the four principal arms, each bridge had two extra arms for equalizing the potential of the guard ring and the potential of the corresponding electrode. The error of bridge measurements did not exceed 10 — 15% for capacitance and 15 — 20% for resistance.

The salinity of the ice samples was determined with an electrical salinity meter calibrated in units of chlorine salinity after preliminary titration of the ice. This calibration was needed because all the measurements with newly formed and pack ice were referred to chlorine salinity; the calibration was legitimate because the ice samples were collected from the same horizons. The application of an electrical salinity meter, which will function with very small quantities of thawed water, made it possible to determine the salinity directly for the ice samples used in measurements.

The samples were cut out from cores at distances corresponding to the 5, 50, and 100 cm horizons for young ice and 75 and 100 cm horizons for pack ice. Samples from the bottom surface of the ice cover and samples of newly formed ice 1 — 2 cm thick were also studied.

The three-electrode capacitors made it possible to compute the effective permittivity (ε), the effective loss angle (tan δ), and the effective volume resistivity of ice (ρ):

$$\varepsilon = \frac{C_x}{C_0},$$

$$\tan \delta = \frac{1}{\omega R_x C_x},$$

$$\rho = R_x \frac{S}{h},$$

where C_x is the measured capacitance of the capacitor with the ice sample, C_0 is the geometrical capacitance of the capacitor, R_x is the measured resistance of the capacitor with the ice sample, S is the area of the guard-ring electrode, h is the thickness of the ice sample.

§ 2. EXPERIMENTAL RESULTS

Figures 2 and 3 show typical temperature curves obtained for three samples of young ice (50 cm depth, 2 March 1966) and three samples of pack ice (75 cm depth, 24 March 1966). The salinity values in the figures are the averages of three measurements. Qualitative analysis of the ' results suggests that the permittivity and the loss angle of sea ice both increase with the increase in temperature. The resistivity falls, and the corresponding curve has two sections of different slope. The most characteristic temperature at which the electrical properties of ice change markedly is the NaCl eutectic point, which may vary between 21.1 and 22.9°C depending cn the concentration and the composition of other salts in sea ice. A quantitative analysis of the results points to significant differences in the electrical parameters of young and pack ice, despite the relatively slight difference in their salinities.
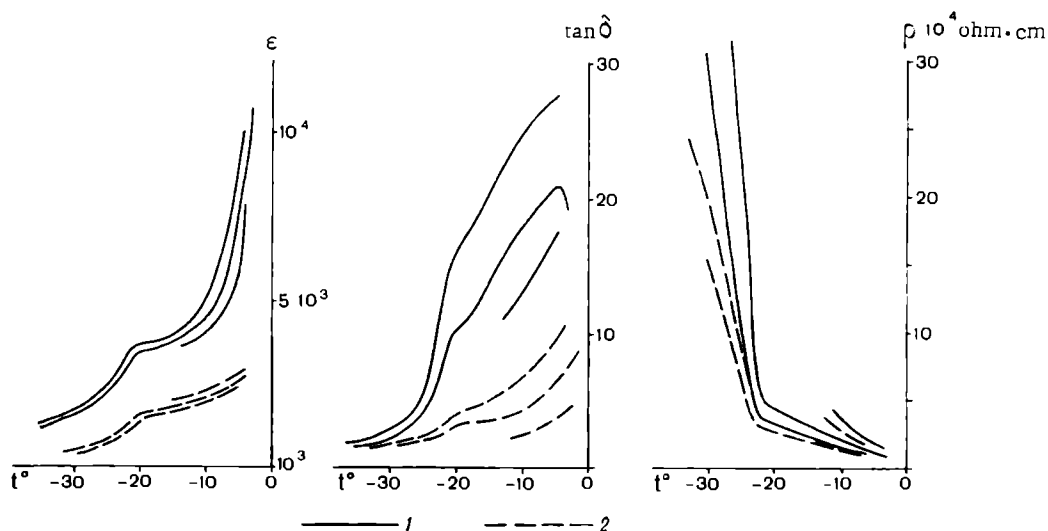
FIGURE 2. Temperature curves of ε, tan δ, and ρ of young ice. Horizon, 50 cm; salinity, 5.4 per mill:

1) 1 kHz; 2) 10 kHz.

Figures 4 and 5 plot the permittivity and the resistivity of sea ice as a function of salinity (average data for November 1965 — October 1966). Note that in the absence of data on the dependence of these electrical parameters on ice structure and density, the averaging provides a general pattern of the variation of ε and ρ of sea ice with salinity. The scatter of

points in these measurements exceeded the experimental accuracy, and this probably provides an indirect indication of the dependence of the electrical parameters on the number, size, and distribution of inhomogeneities inside the sample and in the electrode layer. A particularly large scatter was observed for the loss angle. Table 1 lists the maximum and the minimum values of the loss angle for various salinities and temperatures of ice. No dependence of resistivity on frequency was noted.
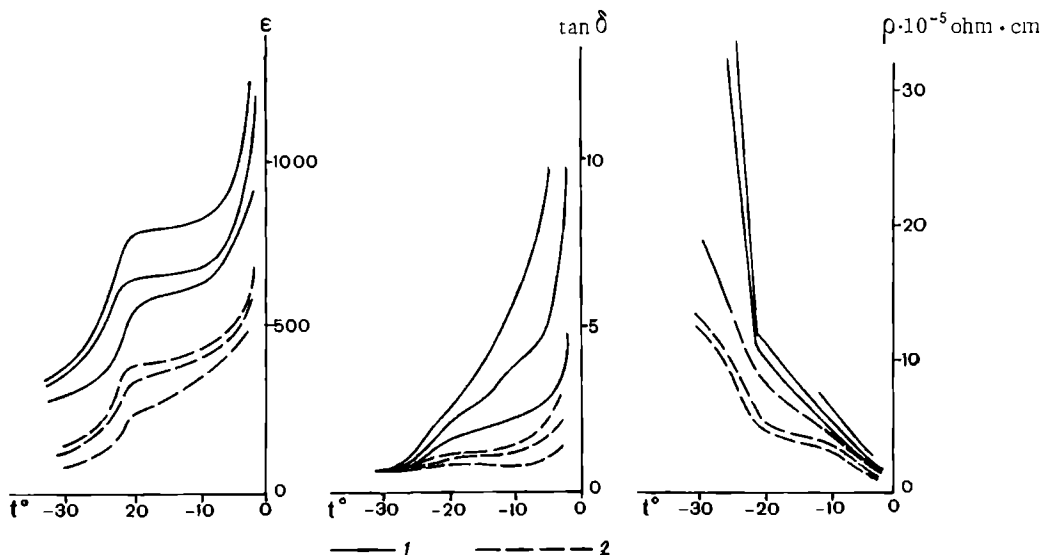
FIGURE 5. Temperature curves of ε, tan δ, and ρ of pack ice. Horizon, 75 cm; salinity, 1.42 per mill:

1) 1 kHz; 2) 10 kHz.

TABLE 1. Effective values of the loss angle

f, kHz	$t°$ C	Salinity, ‰				
		1	3	5	10	14
1	—5	2.5—10	5—30	7—35	17—40	30—40
	—10	1.3—10	3—30	5—35	13—40	30—40
	—20	1.2—5	2.5—25	4—35	9—40	15 —40
	—30	0.3	0.8—6	2—11	4.5—16	5—18
10	—5	0.5—4	1.5 – 15	2.5—20	4—30	15 –35
	—10	0.6—3	1.1—12	1.7—18	3—30	4 –30
	—20	0.6—3	1—12	1.5—19	2.5—30	3.5—30
	—30	0.5—1.5	0.9—3,5	1.2—5	1.6—5.5	2— 5.5
100	—10	3—4.5	3—10	3.2—14	3—15	3—15
	—30	1.2—2,5	2.5—5,5	4—7	5—18	5.5—8
1000	—10	1.3—2	1.5—4	2—7	4 –11	7—12
	—30	0.1—0.35	0.5—1	0.9—2	1.8—2.8	2—2.8

Figures 6 through 9 plot the frequency curves of the effective permittivity of sea ice at various temperatures and salinities. The same figures also give the frequency curves of sweet ice according to Eder /6/.
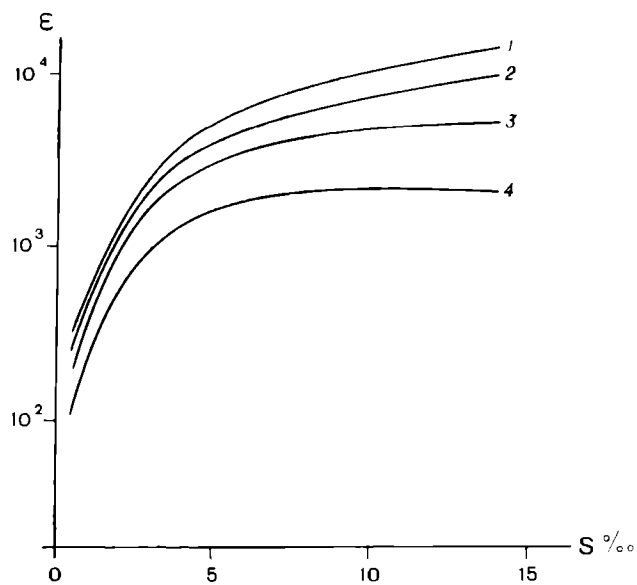
FIGURE 4. ε vs. salinity, $f = 1\,kHz$:
1) $-5°C$; 2) $-10°C$; 3) $-20°C$; 4) $-30°C$.
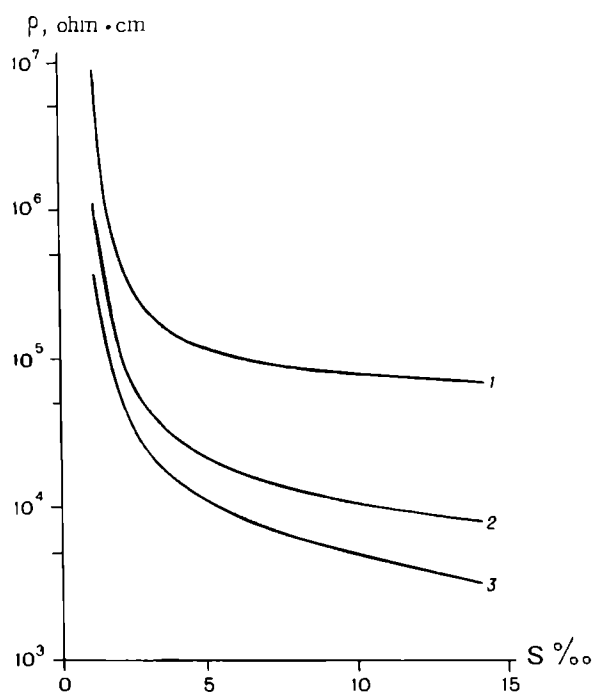
FIGURE 5. ρ vs. salinity, $f = 1\,kHz$:
1) $-30°C$; 2) $-20°C$; 3) $-10°C$.
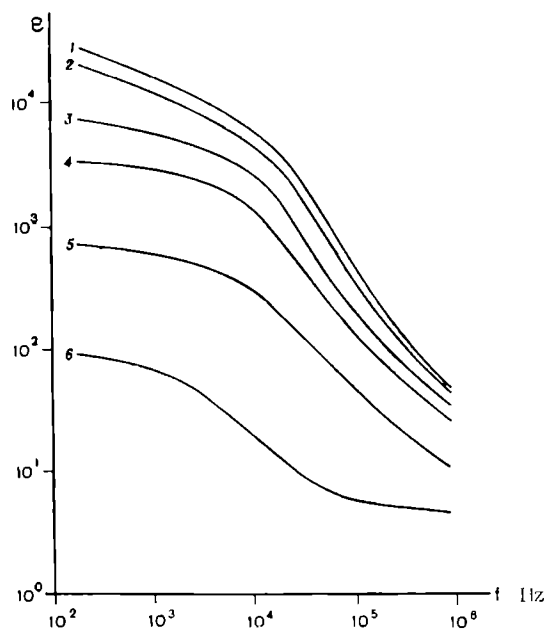
FIGURE 6. ε vs. frequency, $t = -5°C$:

1) 14‰; 2) 10‰; 3) 5‰; 4) 3‰; 5) 1‰;
6) sweet ice (Eder /6/).
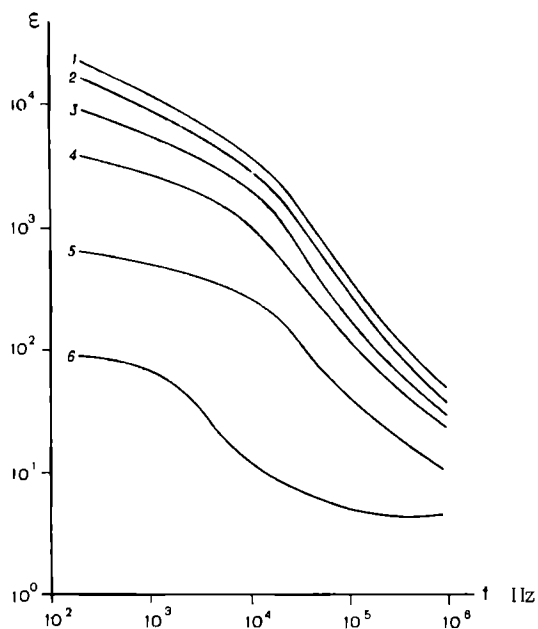
FIGURE 7. ε vs. frequency, $t = -10°C$:

Legend as in Figure 6.
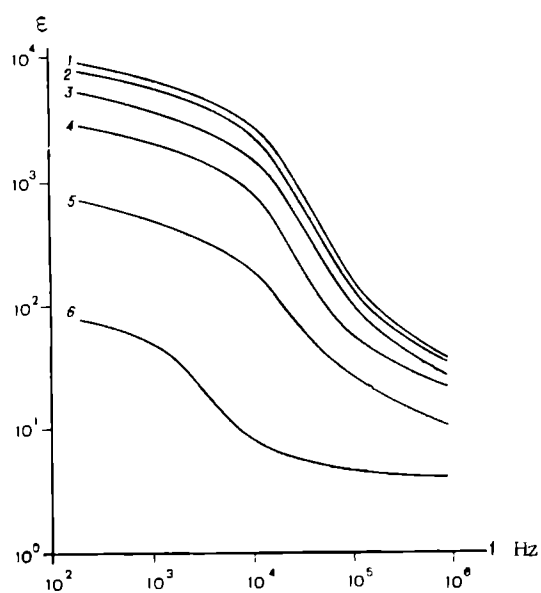
FIGURE 8. ε vs. frequency, $t = -20°C$:

Legend as in Figure 6.
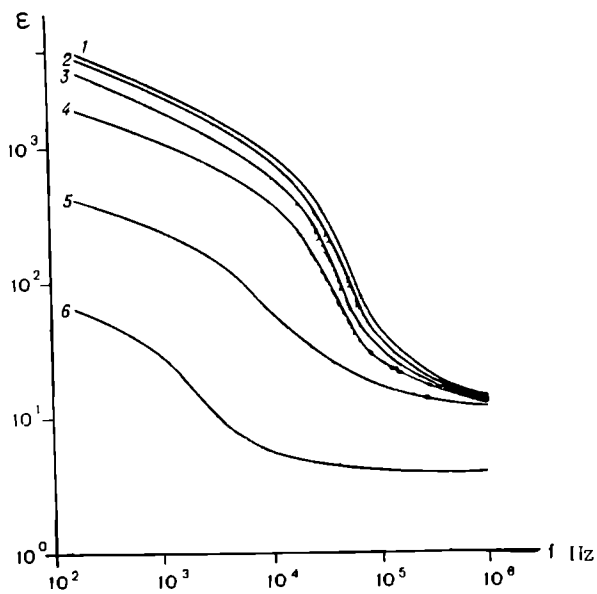
FIGURE 9. ε vs. frequency, $t = -30°C$:

Legend as in Figure 6.

69

§ 3. DISCUSSION OF RESULTS

The effective electrical parameters obtained in our measurements reflect the properties of sea ice immersed in the electrical field of a capacitor in direct contact with the electrodes.

Sea ice is a highly complex dielectric. It contains a mixture of salts which precipitate at various temperatures; it also contains sweet ice crystal crystals and brine. These factors greatly complicate the mechanism of polarization of sea ice. The difference in the electrical characteristics of the different components of sea ice leads to accumulation of space charge as a result of charge migration (interlayer polarization). There is a distinct possibility that the ice crystal lattice may contain interstitial impurity ions, contributing to an ion-relaxation mechanism of polarization.

Sweet ice crystals display dipole-relaxation polarization, and at low frequency sea ice may exhibit structural polarization. Accumulation of space charge in the electrode layer and the accompanying adsorption and electrochemical processes which take place on the electrode surface should lead to a polarization of the electrode layer contributing an additional capacitance between the electrodes, which may markedly exceed the capacitance associated with the permittivity of ice. All these effects lead to exceedingly high effective permittivities; the largest contribution is probably due to electrode polarization.

It is hoped that the experimental curves reflecting the properties of sea ice in contact electrode measurements of its electrical parameters will be useful for solving various problems of electrochemistry, electrical engineering, and physics of sea ice. -

Bibliography

1. Wentwort, F.L. and M.Cohn. Electrical Properties of Sea Ice at 0.1 to 30 Mc/s. — J. Res. NBS USA, Vol. 68. D, No. 6. 1964.
2. Vasil'ev, S.S. and V.S.Luchaninov. Elektricheskie kharakteristiki l'da (Electrical Characteristics of Ice). — Trudy AANII, Vol. 284. 1968.
3. Pounder, E.R. The Physics of Ice. — Oxford, New York. Pergamon Press. 1965.
4. Peschanskii, I.S. Ledovedenie i ledotekhnika (Ice Science and Ice Technology). — Leningrad, Gidrometeoizdat. 1968.
5. Bogorodskii, V.V. and V.A.Rudakov. Elektromagnitnye metody opredeleniya tolshchiny plavayushchikh l'dov (Electromagnetic Methods of Determining the Thickness of Floating Ice). — ZhTF, 32, No. 7. 1962.
6. Eder, P.F. — Ann. d. Phys., 1(7 — 8):381 — 388. 1947.

V. V. Bogorodskii and G. P. Khokhlov

MEASUREMENTS OF THE PERMITTIVITY AND CONDUCTIVITY OF SEA ICE WITHOUT CONTACT ELECTRODES

One of the commonest methods of determining the electrical parameters of matter at low frequencies is by measuring the capacitance and the conductance of a capacitor whose plates are in direct contact with the test sample. However, the free charges which may be present in the sample will migrate in the electrical field of the capacitor, and charge accumulation in the electrode layers will render the contact method largely unsuitable for permittivity and conductivity measurements. Electrode layer polarization introduces additional capacitance and conductance, connected in series with the capacitance and the conductance of the sample, so that the apparent permittivity increases and a higher conductivity is obtained.

Sea ice contains an electrolyte which, on coming in direct contact with the capacitor electrodes, also leads to electrode polarization.

One of the methods which avoid the electrode polarization is the two-thickness method /1/ which can be successfully applied when the thickness and the parameters of the electrode layer remain constant as the thickness of the dielectric layer between the capacitor plates is increased. The two-thickness method, however, is inapplicable to sea ice, as it is impossible to correct exactly for the effect of brine in contact with the electrodes and the distribution of brine near the electrodes will always change from one capacitor to the next.

Another method of measuring the electrical parameters of conductive materials avoids the use of contact electrodes, e.g., in measuring the permittivity and conductivity of electrolyte solutions /2, 3/.

Measurements without contact electrodes use "electrodeless cells" (cells with external electrodes) in which the sample medium is separated from the electrodes by a high-quality dielectric.

The electrical circuit of the cell (Figure 1a) comprises the capacitance C_1 of the dielectric layers connected in series, the capacitance C_x of the test sample and its conductance G_x. Equating the impedance of the cell with the sample to the impedance of the equivalent parallel-substitution circuit (Figure 1b) we obtain the following expression for the resultant capacitance C_r and the resultant conductance G_r:

$$C_r = \frac{b}{a^2 + \omega^2 b^2},$$

$$G_r = \frac{a}{a^2 + \omega^2 b^2},$$

71

where

$$a = \frac{G_x}{G_x^2 + \omega^2 C_x^2}, \quad b = \frac{C_x}{G_x^2 + \omega^2 C_x^2} + \frac{1}{\omega^2 C_1}.$$

Figure 2 plots C_r and G_r vs. the conductance of the sample material at 1 kHz frequency for various values of C_x and $C_1 = 5000\,\mathrm{pF}$. Figure 2 shows that at first the increase in conductance does not affect the resultant capacitance of the cell, which starts changing only after a certain threshold conductance has been attained. As the conductance is increased further, the resultant cell capacitance abruptly increases to a value close to C_1, and becomes independent of the sample capacitance and therefore of any changes in its permittivity. The curves of resultant conductance reach a maximum as the sample conductance is increased; after the abrupt increase in the resultant capacitance, the resultant conductance no longer depends on the capacitance of the sample. This behavior imposes certain restrictions on the range of sample conductances for which the permittivity and the conductivity can be measured with fair reliability in this cell. The maximum conductance G_{max} at which the measurements can be carried out without excessive errors is determined by the conductance G_x corresponding to the upper break in the curve of C_r.
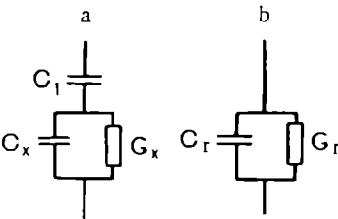
FIGURE 1.
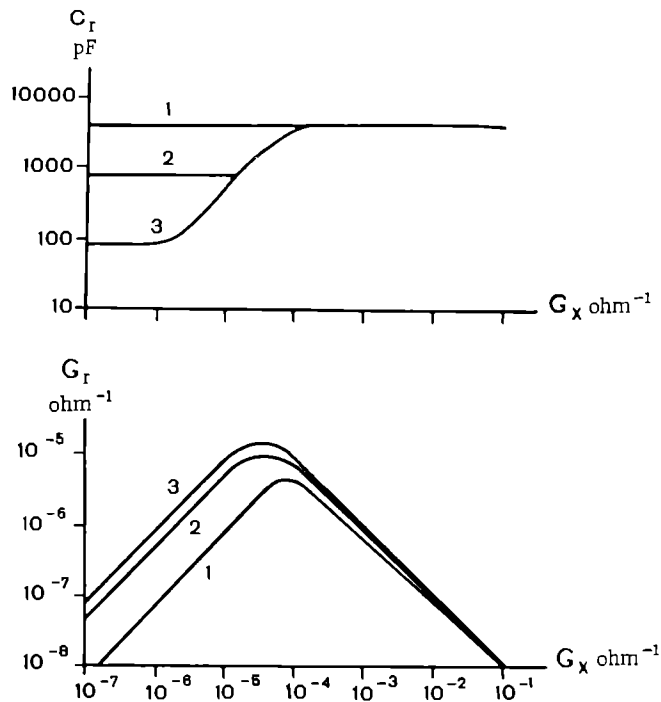
FIGURE 2. C_r and G_r vs. G_x for various C_x:

1) 5000 pF; 2) 1000 pF; 3) 100 pF.
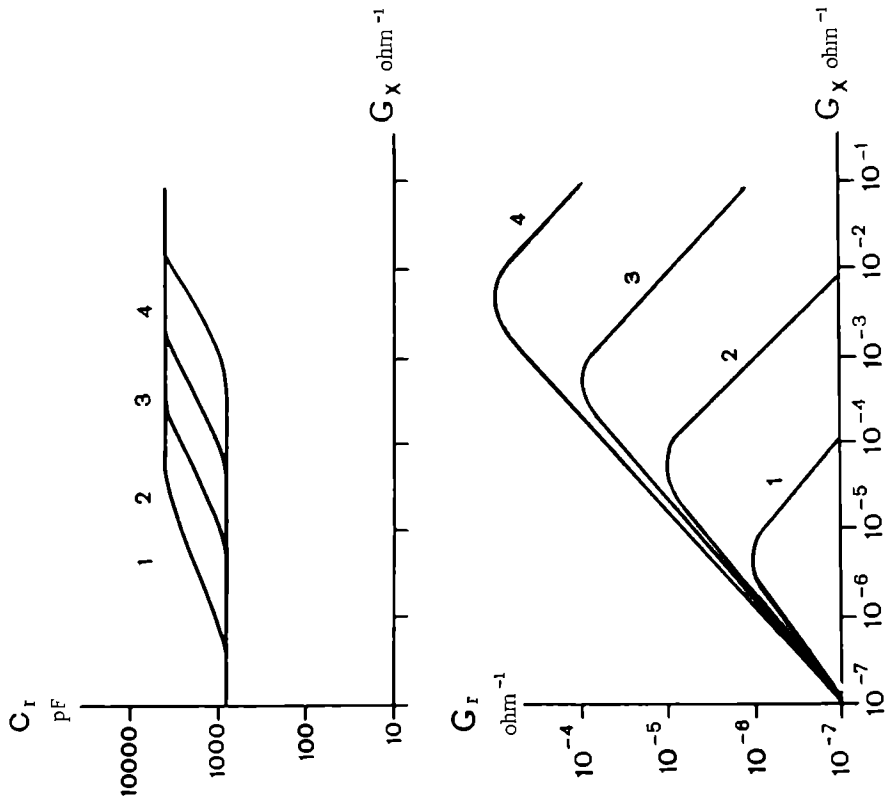
FIGURE 3. C_r and G_r vs. G_x at various frequencies ($C_x = 1000$ pF, $C_1 = 5000$ pF):

1) 100 Hz; 2) 1 kHz; 3) 10 kHz; 4) 100 kHz.
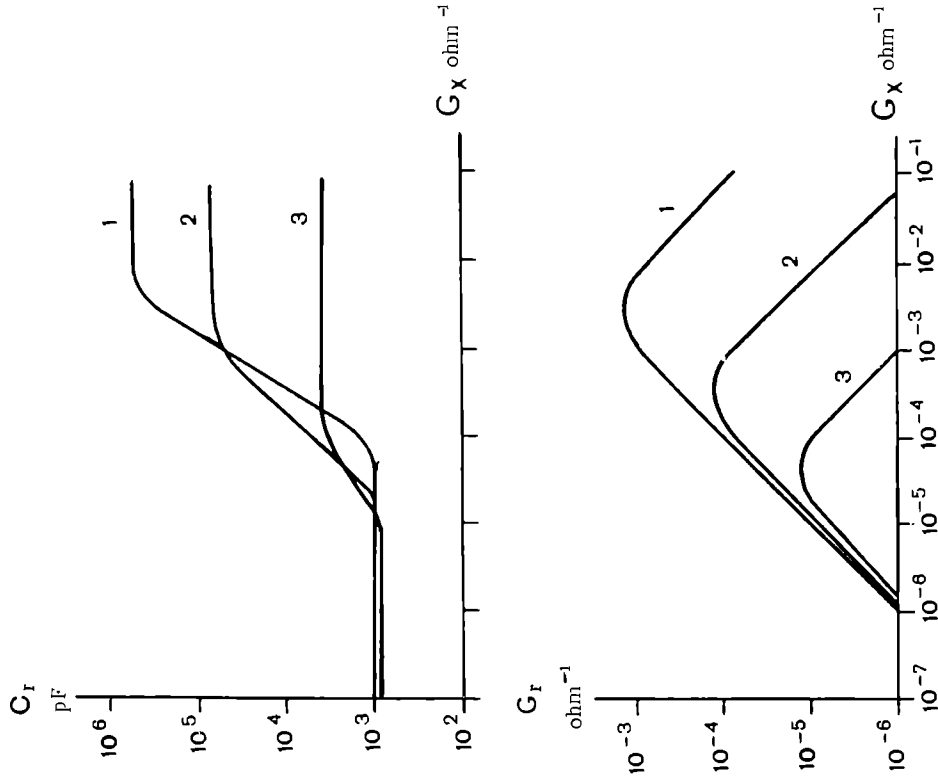
FIGURE 4. The effect of the capacitance C_1 on the effective conductance range, $f = 1$ kHz:

1) $C_1 = 0.5$ μF; 2) $C_1 = 0.05$ μF; 3) $C_1 = 5000$ pF.

At higher frequencies, a wider conductance range is obtained (Figure 3). A substantial reduction of the operating frequency or, alternatively, a broadening of the permissible conductance range at a fixed frequency can be achieved if the capacitance C_1 is increased by reducing the thickness of the dielectric layer coating the electrode surfaces and using a high-permittivity dielectric (Figure 4).

The volume conductivity γ of sea ice may range between 10^{-9} and 10^{-4} $(\text{ohm} \cdot \text{cm})^{-1}$ depending on temperature and salinity /4/. The conductance G_x of an ice sample in the cell may be estimated from the equality

$$G_x = K\gamma \, (\text{ohm})^{-1},$$

where $K = 3.6 \, \pi C_0$, C_0 is the geometrical conductance of the cell, in pF, γ is the bulk conductivity of ice, in $(\text{ohm} \cdot \text{cm})^{-1}$.

Seeing that the coefficient K in most practical cases is chosen equal to at least 10, the conductance of ice samples may vary between 10^{-8} and 10^{-3}ohm^{-1} depending on temperature and salinity. Figure 5 shows the frequency dependence of the maximum conductance of the sample in the cell for various C_1. The range of conductance values of ice samples G_{ice} is also known. We see from the figure that if the electrodes are coated with sufficiently thin layers of high-permittivity dielectric, the electrical parameters of sea ice can be successfully measured at frequencies up to a few kHz.

FIGURE 5. Frequency curves of the maximum conductance of the sample in the cell for various C_1:

1) $C_1 = 0.5 \mu\text{F}$; 2) $C_1 = 0.05 \mu\text{F}$; 3) $C_1 = 5000 \text{pF}$.

The curves give a clear idea of the application of the electrodeless cells to measuring the permittivity and conductivity of sea and saline ice. The working relations make it possible to choose the cell parameters, to estimate the lower frequency limit for a given volume conductivity of ice and known cell parameters, and to determine the cell design and the electrical capacitance of the electrode-coating layers for known conductance and given frequency. The application of the "electrodeless" method will make possible measurements in the frequency range in which the electrical properties of sea ice have remained largely unstudied so far.

Bibliography

1. Efremov, A.N. Ob anomal'noi dispersii nablyudaemoi u nekotorykh dielektrikov v zvukovom diapazone (Anomalous Dispersion Observed in Some Dielectrics in the Acoustic Range).— Trudy Vsesoyuznoi konferentsii po dielektrikam i poluprovodnikam. 1960.
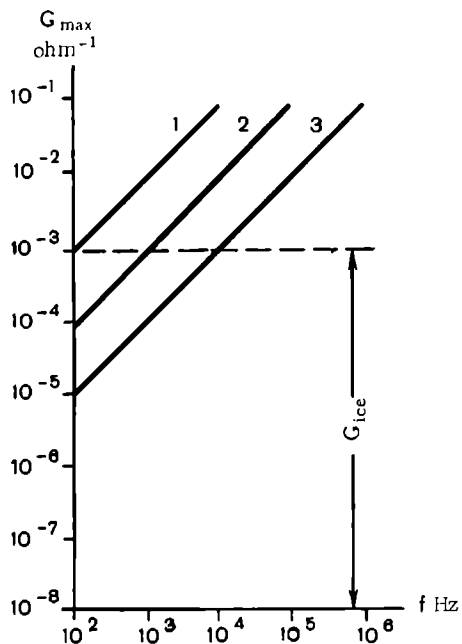
2. Metody issledovaniya elektrofizicheskikh svoistv i protsessov perenosa v elektrolitakh i dielektrikakh (Methods of Study of Electrophysical Properties and Transport Processes in Electrolytes and Dielectrics). — Collection of Articles edited by S. V. Usikov, No. 57, Izdatel'stvo "Khimiya." 1967.

3. O e h m e , F. Dielektrische Messmethoden (zur quantitativen Analyse und für chemische Strukturbestimmungen), 2nd rev. edn. — Weinheim, Verlag Chemie. 1962.

4. P o u n d e r , E. R. The Physics of Ice. — Oxford, New York, Pergamon Press. 1965.

V. V. Bogorodskii and G. P. Khokhlov

TIE EFFECT OF SOME SALT COMPONENTS AND TIEIR COMPOSITION ON TIE ELECTRICAL PROPERTIES OF ICE

The salt content of sea ice is highly variable both in space and in time. It is therefore very important to know the contribution of each salt contained in sea ice to its electrical characteristics.

Studies of the electrical properties of arctic ice, carried out in 1965—1966 on the SP-13f drifting station, confirmed that the effective permittivity of sea ice at low frequencies is of the order of $10^5 - 10^6$. The temperature curves of permittivity and conductivity of sea ice show a fairly sharp break at temperatures around -21 or $-22°C$, associated with the precipitation of sodium chloride. A similar kink observed near $-50°C$ corresponds to the precipitation of calcium chloride /1/.

The very large quantity of salts dissolved in sea water makes the freezing of natural sea ice a highly complex process. Different authors assign different temperatures to the point at which sea ice completely solidifies. According to Ringer, this point is at $-55°C$, according to Gitterman at $-36°C$ /2/, and according to Pounder /3/ even ice cooled to $-80°C$ contains traces of brine. The multicomponent constitution of sea ice may substantially alter the precipitation points of the various salts.

Table 1 lists the eutectic temperatures t_e of binary mixtures and the precipitation temperatures of a number of salts in sea water t_w according to /3/.

TABLE 1.

Salt	t_e °C	t_w °C
KCl	—11.1	−36.8
Na$_2$SO$_4$	—3.5	−8.2
NaCl	21.1	−22.9
MgCl$_2$	—33.6	−43.2
CaCl$_2$	—55.0	−54.0

The variation of the precipitation temperatures of salts as a function of the constitution and the content of other salts should naturally affect the electrical parameters of ice. However, no experimental data are available at this stage on this subject. This gap stimulated our study of the effect of certain salts on the electrical properties of ice.

The effective permittivity ε' and the conductivity γ were measured with E8-2 bridge at 1 kHz using a cell with bulky brass electrodes (these electrodes ensured uniform temperature distribution in the freezing brine within small working volume of the cell). The electrode diameter (11 mm) and the electrode spacing (1.55 mm) were chosen to fit the operating range of the bridge. Chemically pure solutions of KCl, NaCl, and $MgCl_2$ were used in measurements. A medical syringe was used to inject the solutions into the cell through a special hole in the wall. The cell was kept in a TKSI 01/70 thermostating chamber. When the solution had frozen, the temperature curves of ε' and γ were plotted with the cell temperature increasing at a rate of $0.1 - 0.2$ deg/min.
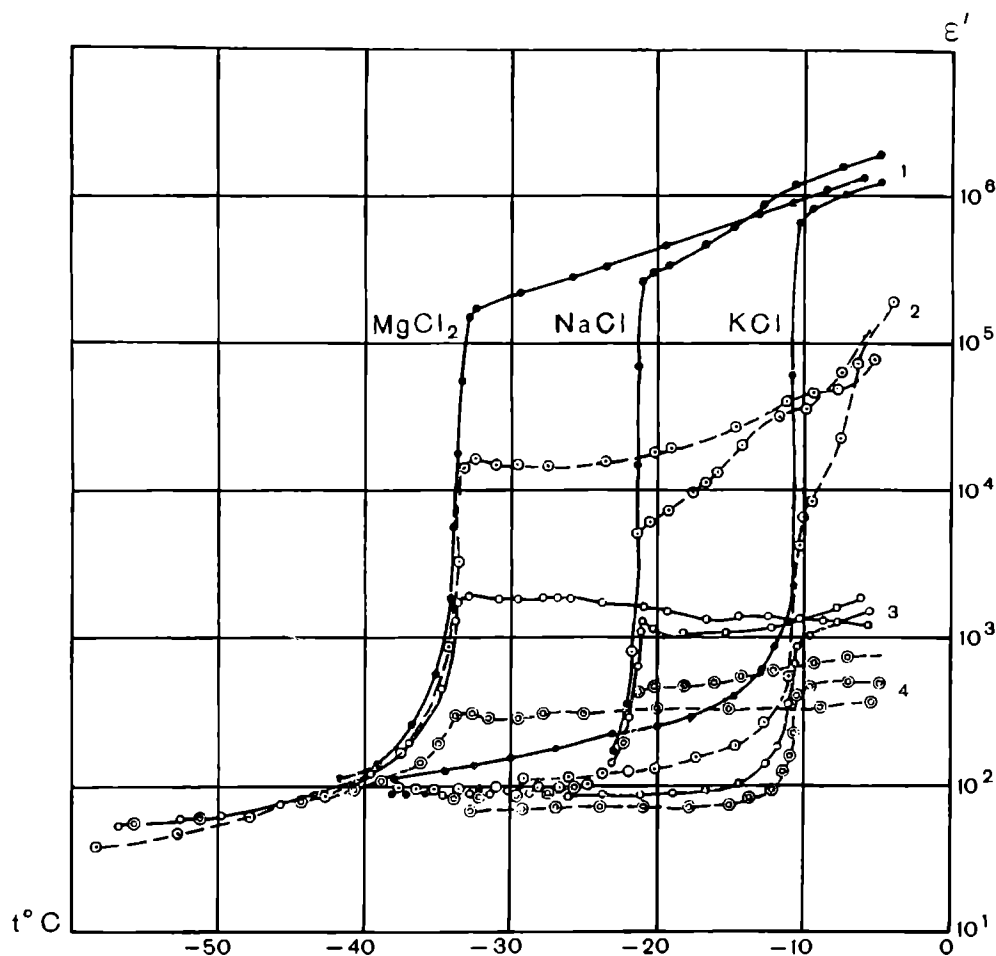
FIGURE 1. Temperature curves of the permittivity ε' of ice prepared from solutions of chemically pure salts of various concentrations:

1) 35 per mill; 2) 15 per mill; 3) 5 per mill; 4) 2 per mill.

Figures 1 and 2 plot the temperature curves of ε' and γ for ice obtained from salt solutions of various concentrations. We see from the figures that the upper kink points of the curves precisely correspond to the eutectic temperatures of binary mixtures (-11.1, -21.1, and -33.6°C). When the eutectic point is reached, a slight decrease in permittivity and conductivity is often observed, possibly due to the redistribution of brine inside the ice volume and in the electrode layers and also to a change in the configuration

77

of the brine cells with increasing temperature. These redistributions may also occur at temperatures far from the eutectic point (see, e.g., the curve of γ for 5 per mill $MgCl_2$). Therefore, at temperatures above the eutectic, the curves will be sufficiently reproducible only if the experimental conditions are constant.
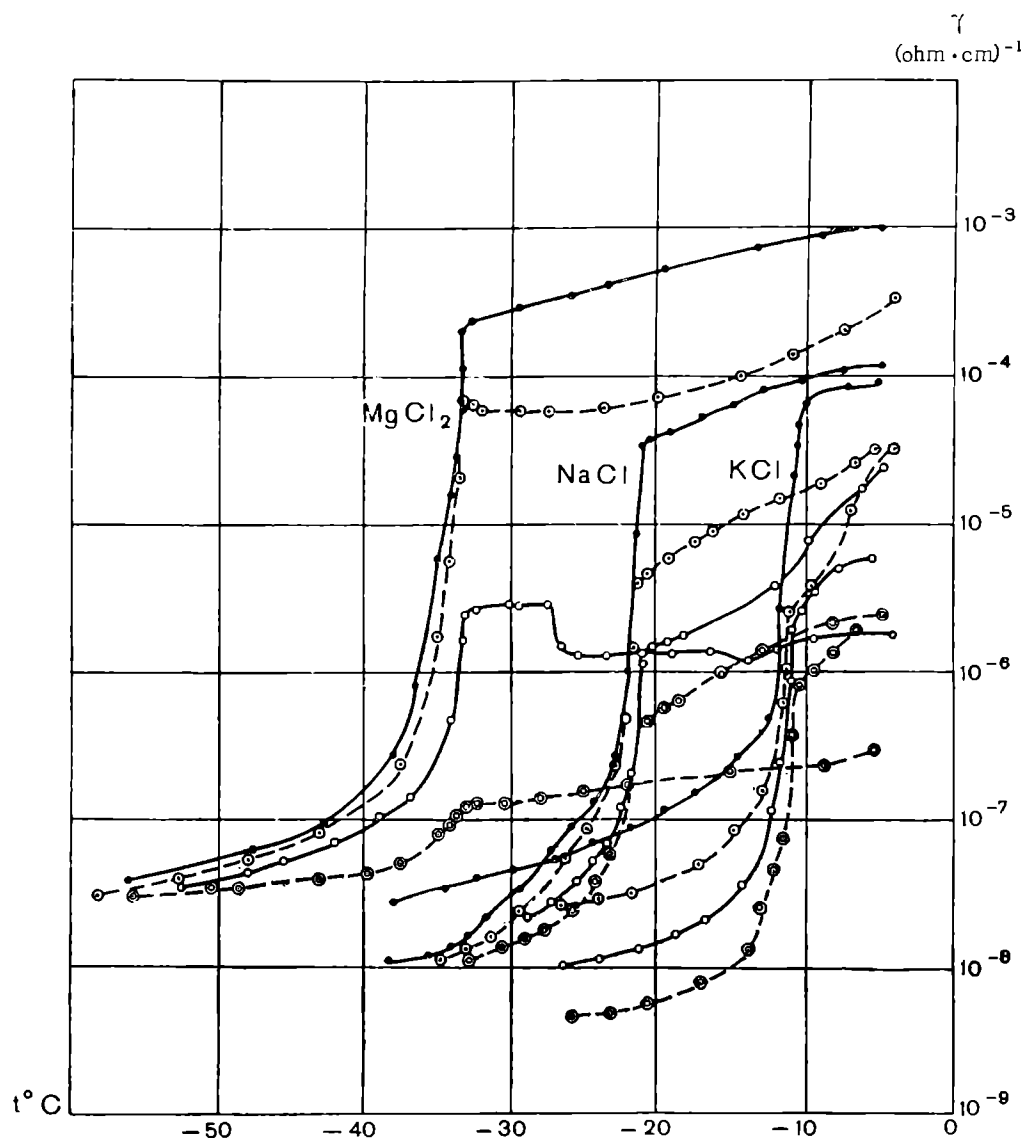

FIGURE 2. Temperature curves of the conductivity γ of ice prepared from solutions of chemically pure salts of various concentrations:

Legend as in Figure 1.

Our experimental procedure ensured adequate reproducibility of results (Figure 3). Regardless of the chemical composition of the salt, the values of ε' near 0°C go to the same limit: about $2 \cdot 10^6$ for $t = -5°C$ and 35 per mill salinity, $2 \cdot 10^5$ for 15 per mill salinity, $2 \cdot 10^3$ for 5 per mill salinity, and $(3-8) \cdot 10^2$ for 2 per mill salinity. The limit values for the conductivity

78

cover a wider range; this is probably due to the higher sensitivity of conductivity to the internal structure of ice. Below the eutectic point, reduction of temperature leads to a slight decrease of ε' for ice prepared for the various salt solutions. The conductivity γ reveals a tendency to increase at low temperatures for salts with relative low eutectic points.
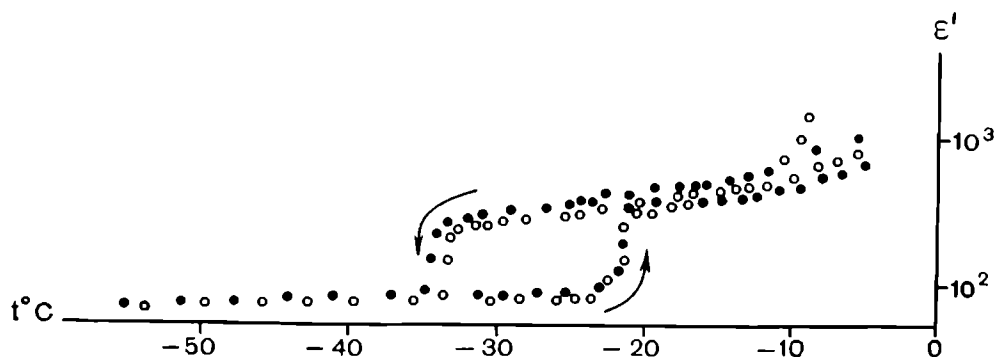
FIGURE 3. Reproducibility of the results of measurements of ε' for two ice samples prepared from a solution of about 2 per mill NaCl.
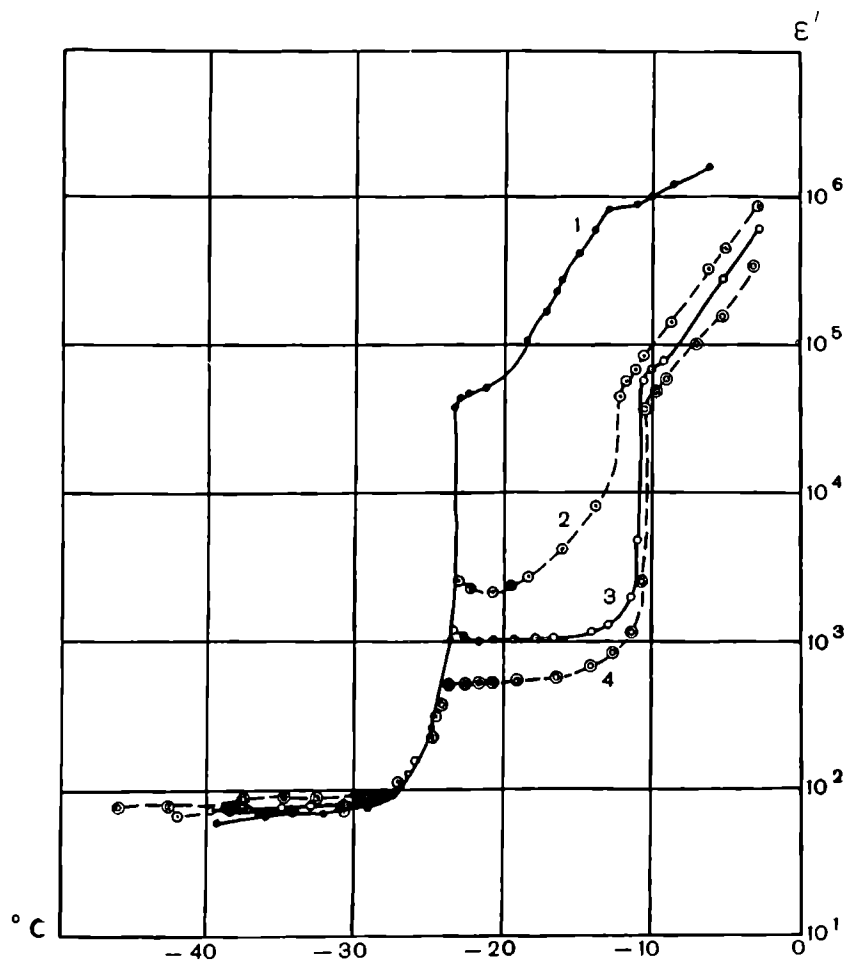
FIGURE 4. Temperature curves of the permittivity ε' of ice prepared from a mixture of 35 per mill KCl solution with an equal volume of NaCl solution of variable concentration:

1) 35 per mill; 2) 15 per mill; 3) 5 per mill; 4) 2 per mill.

Figure 4 plots the temperature curves of the ϵ' of ternary systems; ice prepared from 35 per mill KCl solution mixed with an equal volume of NaCl of variable concentration. We see from the figure that even small quantities of KCl in ice alter the precipitation point of NaCl, which drops from $-21.1°C$ to $-22.9°C$. On the other hand, the presence of small quantities of NaCl in ice (curves 3, 4) does not affect the eutectic temperature of KCl ($-11.1°C$). At higher NaCl concentrations, the precipitation temperature of KCl apparently drops to $-23°C$. This conclusion, however, is highly tentative, since the curves are not sharply defined at these temperatures.

FIGURE 5. Temperature curves of ϵ' and γ of ice prepared from a mixture of 35 per mill NaCl solution with an equal volume of 2 per mill KCl solution.

Highly interesting ϵ' and γ curves (Figure 5) were obtained for ice prepared from a mixture of equal volumes of NaCl (35 per mill) and KCl (2 per mill) solution. It would seem that the minority component, KCl, only binds a certain quantity of NaCl forcing it to precipitate at $-22°C$. The remaining sodium chloride precipitates at its own eutectic temperature, i.e., the effect of potassium chloride is entirely determined by the quantitative ratio of the different salt components in ice.

Temperature curves of ϵ' (Figure 6) and γ were also plotted for ice prepared from a mixture of $MgCl_2$ and NaCl solutions. The presence of NaCl in ice shifts the $MgCl_2$ precipitation point to $35°C$, and the presence of $MgCl_2$ shifts the NaCl precipitation point to around $-22°C$.

Our study of the temperature curves of the electrical parameters of artificial saline ice establishes the effect of each salt on the electrical properties of sea ice and the eutectic temperatures of binary (ice + salt) mixtures. In a number of cases, the results also elucidate the effect of the content and the composition of the salts on the precipitation temperatures of the individual components in a multicomponent system. With the exception of NaCl, no other salt showed the wide variations in the precipitation temperatures, indicated in Table 1 (KCl and $MgCl_2$). The previously observed variation in temperature was probably due to the presence of other salts in sea ice.

Even very slow and gradual freezing of salt solutions leads to a pronounced hysteresis (Figure 3). This effect is also observed in cells of alternative design. It is probably due to the liberation of heat in the sample during the precipitation of the salt.

If this is indeed so, it would seem that the heating of the sample is quite substantial. For example, in experiments with ice prepared from 35 per mill $MgCl_2$ solution, the ice — electrode interface in the capacitor had to be maintained at $-60°C$ for half an hour in order to ensure complete precipitation

of $MgCl_2$. This fact also points to the strong influence of the migration polarization inside the ice volume on the electrical properties of ice.
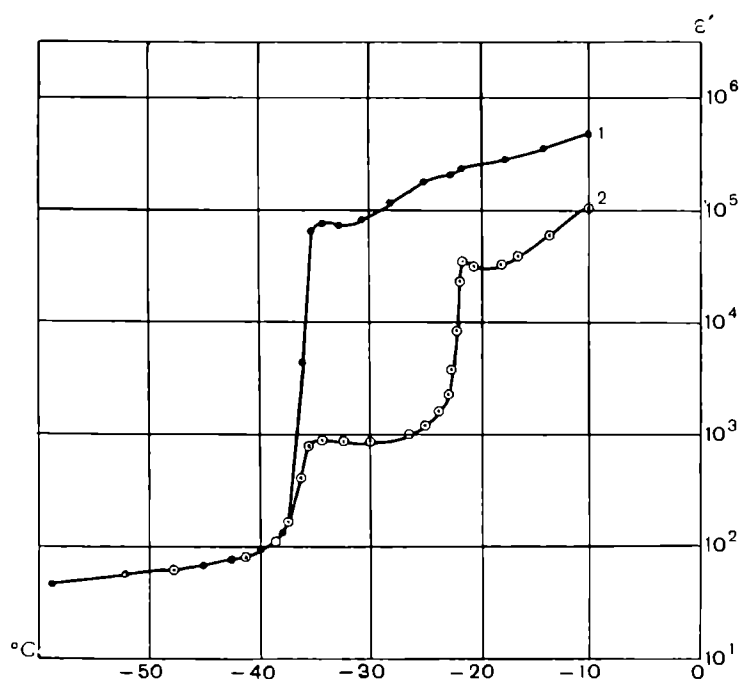

FIGURE 6. Temperature curves of ϵ' of ice prepared from a mixture of 35 per mill NaCl solution with an equal volume of 35 per mill (1) and 2 per mill (2) $MgCl_2$ solution.

Bibliography

1. Fujino, K. Electrical Properties of Sea Ice. — Physics of Snow and Ice. — Vol. 1:1, 633—648, Hokkaido. 1947.
2. Savel'ev, B. A. Stroenie, sostav i svoistva ledyanogo pokrova morskikh i presnykh vodoemov (Structure of Ice and the Properties of the Ice Cover of Saline and Fresh-Water Bodies). — Izdatel'stvo MGU. 1963.
3. Pounder, E. R. The Physics of Ice. — Oxford, New York, Pergamon Press. 1965.

Yu. A. Mach

MEASUREMENTS OF THE MAGNITUDE OF THE MIRROR REFLECTION COEFFICIENT OF THE REAL SURFACE OF SEA ICE FOR ACUTE INCIDENCE ANGLES

The published data on the electrical properties of ice in various radio-wavelength ranges /1, 2/ were mostly obtained with laboratory specimens.

Sea ice is a complex dielectric. Its electrical properties are influenced by a great variety of factors, which include age, morphology, salinity and its vertical distribution, state of aggregation of the brine, presence of snow on the ice surface. No reliable model of ice can be created in the laboratory for adequate simulation of its electrical parameters because of the highly intricate combination of the various factors which affect the ice parameters.

The most reliable results are therefore obtained by studying ice under natural conditions.

The mirror reflection coefficient of decimeter wavelength from a real snow-ice surface of flat ice fields was measured in the winter of 1966 on the SP-13f drifting station.

Since the coefficient of mirror reflection from an interface of two media is a function of wavelength, the electrical properties of the propagating medium, and the incidence angle, measurements of the mirror reflection coefficient of ice fields automatically provided data on the permittivity of the reflecting surface under natural conditions.

Measurements were made with flat snow and ice surfaces on floes of uniform structure. The floes were larger than the first Fresnel zone. The height of the unavoidable irregularities in the first Fresnel zone was $\lambda/8$ and less.

An antenna movable in the vertical direction and receiving equipment were used to determine the interference pattern of a wide-beam transmitter antenna. By measuring the relative signal variations in the receiver, the accuracy of the results was substantially increased.

The measuring setup consisted of a transmitting horn on top of a mast. The height of the antenna phase center was $H = 8$ m.

The antenna had a wide conical beam with $\Delta\varphi_a = 28°$ at the -3 dB level. The axis of the antenna beam was tilted downward at $\alpha = 2-3°$ relative to the horizon. The horn on top of the mast could radiate waves of horizontal and vertical polarization.

The receiving antenna was a half-wave oscillator with a stud reflector, mounted on another mast. It could be aligned to receive waves of horizontal and vertical polarization. The beam width of the receiving antenna in both planes of polarization was $\Delta\varphi_r = 45°$ at -3 dB level. The antenna could be moved up and down the mast without changing its alignment.

The maximum height above the surface was h_{max} = 8 m. Generally, the antenna was set at fixed heights.

The transmitter was a standard signal generator of adjustable power.

The pulse length was τ = 0.25 μsec. Repetition frequency F = 1000 Hz. The wavelength was chosen in the middle of the decimeter range (λ = 40 cm). The receiver passband was 22 MHz.

The transmitting antenna with the transmitter and a power pack was mounted at the far end of the measurement traverse, at a distance L from the receiving antenna. The receiving antenna was set up at the other end of the traverse. A coaxial cable connected the antenna to the receiver, which was mounted in a hut together with an attenuator and an oscilloscope. A D-2-13 coaxial-type instrument was used as the attenuator (it had been specially calibrated at f = 700 MHz). The range of attenuation measurements of this instrument was from 2.5 to 40 dB. The dynamic range of measurements could be extended by additional coaxial attachments, model DO-1.

The receiver video signal was displayed on the cathode-ray oscilloscope S1-20 (with A type sweep). The received signal fell in the linear range of the amplitude characteristics of the amplifiers and the detector. The signal level markedly exceeded the noise level.

The particular dislocation of the equipment components in the measurement area and the use of A type sweep simplified the suppression of synchronous interference.

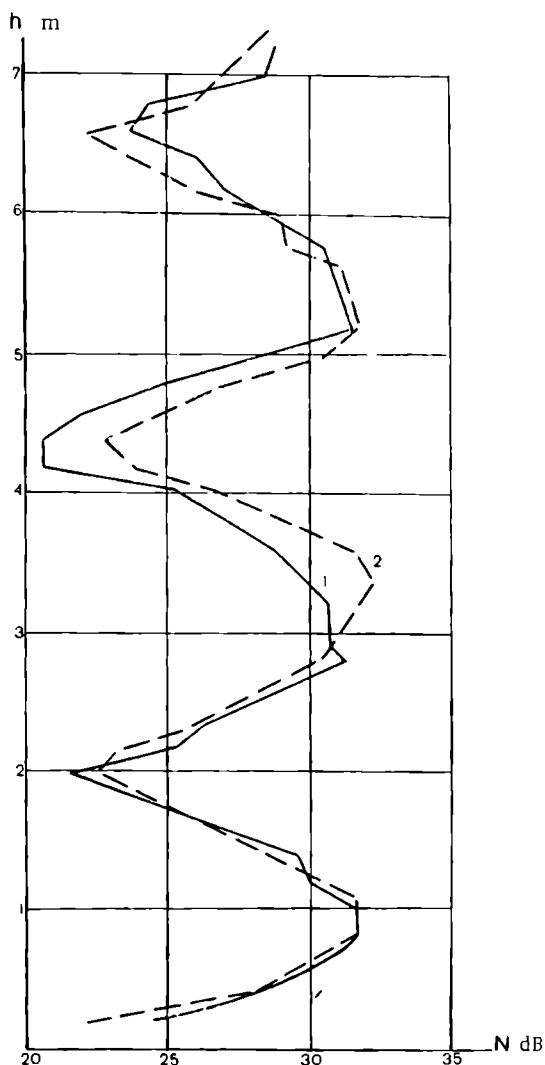After warm-up, measurements were begun. The receiving antenna was moved along the path to certain control points (at distances of 10 or 20 cm). The variable attenuator shaped a pulse of certain predetermined amplitude on the oscilloscope screen. The attenuation reading characterized the relative power of the received signal. The receiver gain and the transmitter power remained constant during the entire measurement cycle.

Figure 1 plots a typical experimental curve of the variation of signal intensity as a function of antenna height.

Unfortunately, because of numerous cracks in the floe, a larger measurement area could not be used, nor was it possible to increase the antenna separation.

FIGURE 1. Reflection curves, traverse No. 3, L = = 80 m (vertical polarization):

1—first measurement cycle; 2—second cycle.

The distance between the antennas ranged from $L_1 = 35$ m to $L_5 = 100$ m.

The characteristics of the measurement traverses are listed below:

traverse No. 1: $L = 50$ m, flat floe of year-old ice with a loose snow layer $10-12$ cm thick; irregularities $\Delta h \cong 1/_\mu \lambda$;

traverse No. 2: $L = 100$ m; flat pack ice floe, no snow; irregularities $\Delta h < 1/_8 \lambda$;

traverse No. 3: length from 35 to 100 m; flat pack ice floe, as in traverse 2, but with more snow in the surface pores; snow irregularities about $\Delta h \cong 1/_\mu \lambda$. Ice cores from this traverse showed that the top layer to a depth of $3-5$ cm mainly consisted of wind-blown snow; the layer from 3 to $18-25$ cm was made of highly porous (firm) ice. Pore diameter up to 0.5 cm. Cavities up to $1-2$ cm present; deeper-lying layers contained transparent ice with minute pores and air bubbles up to $0.3-0.5$ cm in diameter; dense ice began at depths of $30-35$ cm.

A total of 28 experimental curves were obtained for the two polarizations and all the measurement traverses.

The analytical expressions for the magnitude of the mirror reflection coefficient ρ were obtained as follows.

The field produced by a direct beam at the receiving antenna is

$$E_d = \frac{245 \sqrt{P_{tr} \, G_d}}{R_d} \cos \omega t, \tag{1}$$

and the field of the reflected beam is

$$E_{ref} = \frac{245 \sqrt{P_{tr} \, G_{ref}} \, \rho}{R_{ref}} \cos \left(\omega t - q - \frac{2\pi}{\lambda} \Delta R \right), \tag{2}$$

where P_{tr}, ω, λ are the power, the frequency, and the wavelength of the transmitter; G_d, G_{ref} are the directivities of the transmitting antenna in the corresponding directions; q is the phase shift on reflection; R_d, R_{ref} are the path lengths of the direct and the reflected beam; ΔR is the path difference.

Clearly,

$$\Delta R = R_{ref} - R_d = \sqrt{(H + 2\Delta + h)^2 + L^2} - \sqrt{(H - h)^2 + L^2}. \tag{3}$$

where H and h are the respective heights of the phase centers of the transmitting and the receiving antenna, L is the traverse length, Δ is the depth of the effective reflecting layer.

The resultant electrical field produced by the direct and the reflected waves is a vector quantity. The expression for the resultant field is

$$\overline{E} = \overline{E}_d + \overline{E}_{ref}.$$

Only the peak values of the field strength (maximum and minimum) were obtained with adequate reliability. The arguments of $\cos \omega t$ and $\cos(\omega t - q - \frac{2\pi}{\lambda} \Delta R)$ in (1) and (2), which determine the phase of the field vector, are therefore set equal to $\pm \pi$.

In other words, for the peak field values we have

$$|E_{max\,h}| = |E_d| + |E_{ref}|,$$ (4)

$$|E_{min\,h}| = |E_d| - |E_{ref}|.$$ (5)

In case of vertical polarization, expressions (4) and (5) should be corrected for the different orientation of the field vector of the direct and the reflected beam. Since only the projections of the vectors on the vertical axis should be considered, we have

$$|E_{max\,v}| = |E_d|\cos\gamma_1 + |E_{ref}|\cos\varphi_1,$$ (6)

$$|E_{min\,v}| = |E_d|\cos\gamma_2 + |E_{ref}|\cos\varphi_2.$$ (7)

Taking the ratio of (4) and (5), we find

$$\frac{|E_{max\,h}|}{|E_{min\,h}|} = \frac{|E_d| + |E_{ref}|}{|E_d| - |E_{ref}|}.$$ (8)

Inserting the expressions for the field of the direct and the reflected wave, we obtain after some manipulations

$$\rho_h = \frac{R_{ref}}{R_d}\sqrt{\frac{G_d}{G_{ref}}}\;\frac{\dfrac{|E_{max\,h}|}{|E_{min\,h}|} - 1}{\dfrac{|E_{max\,h}|}{|E_{min\,h}|} + 1}.$$ (9)

In case of vertical polarization, we similarly obtain for the magnitude of the mirror reflection coefficient

$$\rho_v = \frac{R_{ref}}{R_d}\sqrt{\frac{G_d}{G_{ref}}}\;\frac{\left(\dfrac{|E_{max\,v}|}{|E_{min\,v}|} - 1\right)\cos\gamma}{\left(\dfrac{|E_{max\,v}|}{|E_{min\,v}|} + 1\right)\cos\varphi}.$$ (10)

The values of the parameters entering these expressions were determined as follows. The intensity of the direct and the reflected beam was determined from geometrical considerations using (3). The antenna separation L was measured with a tape. G_d and G_{ref} were derived from an experimentally obtained antenna pattern, as measured in "free" space. The value of the ratio $\dfrac{|E_{max}|}{|E_{min}|}$ was taken from the corresponding experimental "curve" : it was assumed equal to half the difference in attenuator readings between adjoining maximum and minimum.

An estimate of the accuracy of the results obtained from (9) and (10) shows that the maximum relative error in the magnitude of the mirror reflection coefficient is $(\delta\rho)_{max} = \pm\,0.12$.

The results of several measurement cycles for the same range L showed fair reproducibility.

Before computing the reflection coefficient, we compared the peak amplitudes of the experimental field curves with the theoretical amplitudes calculated for reflection from the top surface, i.e., for $\lambda = 0$. We found that 84% of the results fell within the $\pm 10\%$ deviation range. Only 16% of the peak field amplitudes fell outside this range.

85

Further processing was carried out using expressions (9) and (10), and the effective reflecting layer was assumed to coincide with the top surface $(\Delta = 0)$.

Figures 2 and 3 plot the results of the computations and give the theoretical curves of the mirror reflection coefficient for various relative permittivities ε_0.
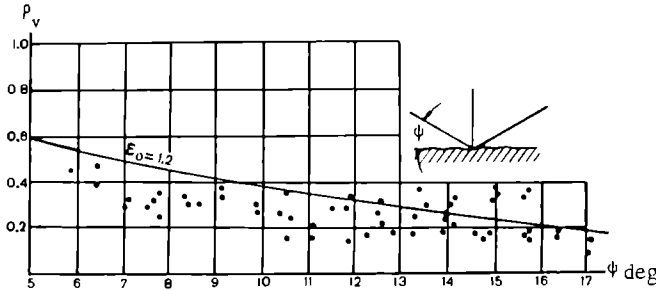

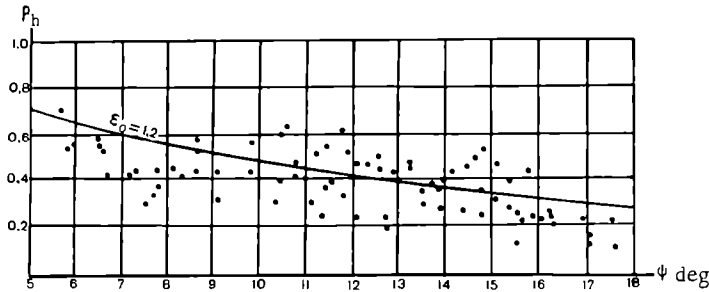FIGURE 2. Computed magnitude of the mirror reflection coefficient (vertical polarization).

FIGURE 3. Computed magnitude of the mirror reflection coefficient (horizontal polarization).

The theoretical dependence of the reflection coefficient was plotted from standard expressions /4/. At low temperatures of the air — ice surface, the imaginary component of permittivity could be ignored because of the low conductivity and the high frequency /5/.

The experiments and subsequent computations led to the following conclusions:

1. The magnitude of the mirror reflection coefficients for decimeter radio waves reflected from a natural ice — snow surface of arctic seas at temperatures of -35 to $-40°C$ for incidence angles $0 = 5 - 20°$ is close to the reflection coefficient computed for a dielectric with relative permittivity $\varepsilon_0 = 1.2$.

The electrical parameters of glacier snow are considered in /2/, where it is shown that relatively loose snow also has the same permittivity.

The measurements confirmed the theoretical findings and showed that loose dry snow and porous dry ice have identical permittivity for sub-Brewster incidence angles.

2. The variation of the reflection coefficient with incidence angle is not affected by the thickness of the snow cover: the snow thickness on traverse No. 1 was $\Delta h \cong \lambda/4$ (about $10-12$ cm) and on traverse No. 2, $\Delta h < \lambda/10$ (less than 3 cm).

Microwave signals in the range of sub-Brewster angles are apparently reflected from the interface between the two media.

3. The results apply to dry snow-covered and ice surfaces. For the exposed surface of young ice, which contains a liquid phase in the top layers, we should apparently distinguish between two cases: the surface is covered by hoarfrost crystals (in this case the reflection coefficient should essentially coincide with the above results) and the ice surface is exposed (the reflection coefficient is then determined by the liquid phase — brine with $\varepsilon_0 = 80$).

In conclusion, I would like to acknowledge the great help of I. I. Pronin in collecting the necessary data under the severe conditions of the arctic night.

Bibliography

1. Bogorodskii, V. V. and G. Rudakov. Elektromagnitnye parametry snega, l'da presnoi i morskoi vody (Electromagnetic Parameters of Snow, Sweet Ice, and Sea Ice). — In: Sbornik "Primenenie radiofizicheskikh metodov v okeanograficheskich issledovaniyakh", Leningrad. 1965.
2. Evans, J. Dielectric Properties of Ice and Snow. — Journal of Glaciology, Vol. 5, No. 42. 1965.
3. Sivers, A. P. and N. A. Suslov. Osnovy radiolokatsii (Elements of Radar). — Moskva, Izdatel'stvo "Sovetskoe Radio". 1956.
4. Vvedenskii, B. A. and A. G. Arenberg. Rasprostranenie ul'tra-korotkikh radiovoln (Propagation of Ultra-Short Waves). — Svyaz'-radioizdat. 1938.
5. Brand, A. A. Issledovanie dielektrikov v SSSR na SVCh (Investigation of Dielectrics at Microwave Frequencies in the USSR). — Fizmatgiz. 1963.

V. V. Bogorodskii and G. P. Khokhlov

INTERLAYER POLARIZATION IN ICE WITH NaCl INCLUSIONS

Sea ice is an inhomogeneous dielectric which, besides sweet ice crystals, also contains numerous foreign impurities with electrical properties markedly different from those of sweet ice.

The high permittivities obtained by contact measurements /1—3/ are probably attributable to the effect of several polarization mechanisms, the most significant being the interlayer polarization and the polarization of the electrode layer. It is therefore very important to determine the individual contributions of these polarization components to the electrical parameters of sea ice. Unfortunately, no such studies have been made so far.

Our aim was to determine the migration polarization in ice containing NaCl impurities and to estimate its contribution. The migration polarization can be detected either by injecting salts into the sample volume or by studying the electrical properties of impurity ice by methods which avoid the electrode polarization effects (e.g., by the method without direct contact electrodes /4/). The application of the former technique limits the results to high-salinity ice, and the measurements cannot be carried out at some frequencies (e.g., not at sound frequencies). The application of the second procedure is limited by technical considerations: it is not easy to produce thin insulating coatings on the electrodes. As a result, the corresponding measurements are limited to low frequencies.

We investigated the electrical properties of ice which had been doped with sodium chloride by embedding the impure sample inside a sweet ice sample. The contribution of the interlayer polarization was elucidated by the "electrodeless" method.

§1. PROPERTIES OF ICE WITH EMBEDDED NaCl CORE

The measurements were carried out between $3 \cdot 10^2$ and $2 \cdot 10^4$ Hz. The measuring capacitor was in the form of a tub (23 × 23 × 10 cm) with electrodes with guard rings affixed to the side walls. The sweet ice in the tub was prepared by pouring distilled water over ice fragments and allowing the conglomerate to freeze (the ice fragments were also prepared from distilled water). The measurements were carried out at −15°C using an E8-2 bridge. Sodium chloride was introduced by pouring a 35 % NaCl solution into holes 10.2 mm in diameter drilled in ice in a plane equidistant from the two

electrodes. The capacitor parameters were measured after the solution had frozen.

The dependence of ε' and tan δ on frequency and the equivalent salinity S_e (obtained by correcting the salinity of the initial solution for the total ice volume under the guard-ring electrode) is shown in Figure 1. Curves for pure ice (1) and ice with $S_e = 1.1$ per mill (5, $t = -30°C$) are also given. We see from Figure 1 that the permittivity increases with the increase in S_e, and the frequency dependence of tan δ changes.
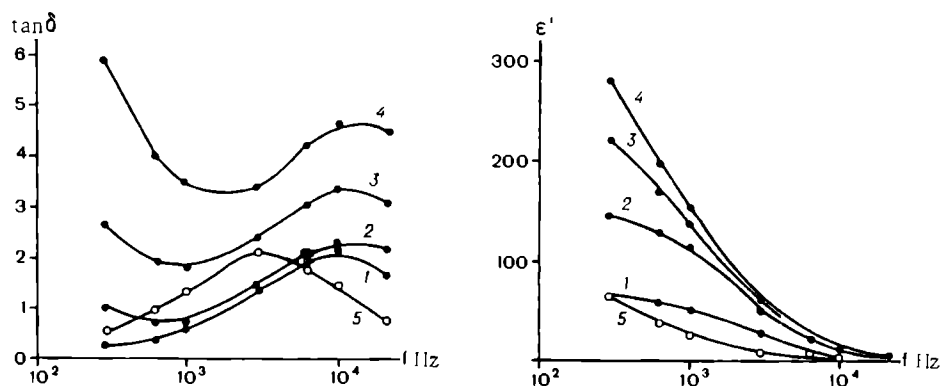
FIGURE 1. Frequency curves of ε' and tan δ for pure ice (1) and for ice with various equivalent salinities S_e at $t = -15°C$:

1) pure ice; 2) 0.59 per mill; 3) 0.855 per mill; 4) 1.1 per mill; 5) 1.1 per mill (at $t = -30°C$).

The aim of the experiment was to detect anomalously high values of ε' of saline ice at low frequencies. The results show that this anomaly is indeed observed.

For NaCl-doped ice the anomaly is observed at temperatures above the eutectic point, i.e., when ice contains a liquid phase. Below the eutectic temperature, a marked suppression of ionic conductivity is expected; this effect is indeed observed at $-30°C$ (curve 5). In this case, the experimental curves correspond to the curves of sweet ice.

§2. DIELECTRIC CONSTANTS OF SALINE ICE OBTAINED BY "ELECTRODELESS" MEASUREMENTS

The electrodes in the "electrodeless" measurements of ε' and tan δ of saline ice were coated by VL-941 varnish (a solution of polyvinylformalic and phenolformaldehyde resins with some triethanolamine added). The polymerization of the varnish took place in a desiccator at 150°C. The enamel film produced in this way had a high mechanical strength and excellent insulating properties.

The measurements were carried out with a partly filled capacitor at 500 kHz. Ice was frozen layer by layer in a thin-walled Plexiglas ring (50 mm in diameter, 10 mm high). While ice was being prepared, the ring was placed directly on the electrode. The second cold electrode was frozen to the ring after the last portion of the solution had been added. The capacitor was left for an hour at $t = -11°C$; then it was fitted into the stopper of

a vacuum flask and transferred to E10-2 bridge for measurements. Two measurements were carried out for the determination of ε' and $\tan \delta$: one with an empty ring (Figure 2a) and another with ice-filled ring (Figure 2b). In this way, we could readily find the capacitance C'_x of the circuit consisting of the capacitance C_i of the insulating layer in the ring connected in series with the ice capacitance C_x and having the ice conductance G_x in parallel to it:

$$C'_x = C_{meas} - C_{tot} + C_0, \qquad (1)$$

where C_{meas} is the measured capacitance of the capacitor with the sample, C_{tot} is the measured capacitance of the capacitor without the sample, C_0 is the geometrical capacitance inside the ring.
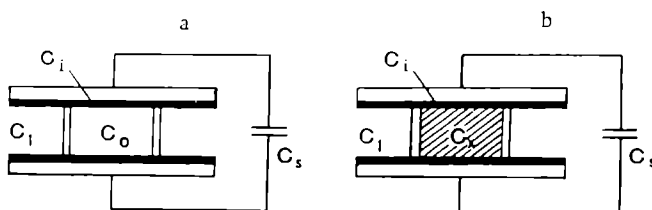

FIGURE 2.

Two measurements enabled us to eliminate from (1) the parasitic capacitances of the stopper holder C_s and the capacitance C_1 associated with the edge capacitance and the capacitance of the outer surface of the electrodes. Further calculations were carried out using the relations

$$C_x = \frac{b}{a^2 + 4\pi^2 f^2 b^2}; \quad G_x = \frac{a}{a^2 + 4\pi^2 f^2 b^2},$$

where

$$a = \frac{1}{G_{meas}\left[1 + 4\pi^2 f^2 \frac{(C'_x)^2}{G^2_{meas}}\right]},$$

$$b = \frac{C'_x}{G^2_{meas}\left[1 + 4\pi^2 f^2 \frac{(C'_x)^2}{G^2_{meas}}\right]} - \frac{1}{4\pi^2 f^2 C_i},$$

$$\varepsilon' = \frac{C_x}{C_0}; \quad \tan \delta = \frac{G_x}{2\pi f C_x}.$$

G_{meas} is the measured capacitance of the capacitor with the sample.

C_i was measured by pouring mercury into the ring and then measuring the capacitance between mercury and the electrode. This capacitance was found to be 710 pF for each electrode.

The no-contact electrodes were used to measure the electrical properties of sweet ice and of ice prepared from a NaCl solution of 1.1 per mill salinity. A pair of identical electrodes, but without the varnish coat, was also tested. The corresponding results are listed in Table 1.

Seeing that different samples were measured each time, the results are quite satisfactory as far as scatter of data is concerned. We see from the

table that the permittivity of saline ice, as well as tan δ, are higher than those for sweet ice and fit the published data for arctic drifting ice /1/. Apart from that, no significant differences were noted in the electrical parameters of ice as measured by the two methods. This proves that the effect of the electrode polarization on the electrical properties of ice is much less significant (at 500 kHz) than the effect of volume polarization.

TABLE 1.

Ice	Measurement method				Relative error, %	
	contact electrodes		no-contact electrodes		$\Delta\epsilon'/\epsilon'_{av}$	$\Delta\tan\delta/\tan\delta_{av}$
	ϵ'	$\tan\delta$	ϵ'	$\tan\delta$		
Sweet	3.1	0.308	2.85	0.27	5	10
Saline	8.9	2.78	8.8	1.74	1.1	19

The results prove the existence of interlayer polarization in ice with salt inclusions and identify it as a dominant factor. Further studies in this direction, in our opinion, should be carried out in a wide range of frequencies, temperatures, and salinities. The effect of saline ice structure on its electrical properties should also be considered.

Bibliography

1. Khokhlov, G. V. Results of Experimental Measurements of the Electrical Parameters of Arctic Sea Ice at Frequencies between 100 Hz and 1 MHz. — This collection, p. 64.
2. Fujino, K. F. — Physics of Snow and Ice, Vol. 1, Hokkaido. 1967.
3. Addison, I. R. and E. R. Pounder. — Physics of Snow and Ice, Vol. 1, Hokkaido. 1967.
4. Bogorodskii, V. V. and G. P. Khokhlov. Measurements of the Permittivity and Conductivity of Sea Ice without Contact Electrodes. — This collection, p. 71.
5. Bogorodskii, N. P., Yu. M. Volokobinskii, A. A. Vorob'ev, and B. M. Tareev. Teoriya dielektrikov (Theory of Dielectrics). — Moskva-Leningrad, Izdatel'stvo "Energiya". 1965.

B. Ya. Gaitskhoki, P. T. Morozov, and L. I. Sovalkov

STUDIES OF THE STRUCTURE AND COMPOSITION
OF SEA ICE IN THE ARCTIC BASIN

The present paper describes some results regarding the structure and composition of sea ice formations of various ages, obtained on the SP-13f drifting station.

Sea ice constitutes a ternary system — the solid phase consists of ice crystals and salt precipitates, the liquid phase consists of inclusions of salt solutions, and the gaseous phase consists of air inclusions.

The constitution of the ice cover is described in terms of its crystal structure and texture.

The structure is a function of crystal size, shape, and the spatial arrangement; the texture is a combination of external aspect features associated with the size, shape, and concentration of various inclusions in ice.

A qualitative estimate of inhomogeneities determines the density and salinity of ice. Ice salinity is expressed as the weight (in grams) of all the solid salts in 1 kg of ice. Ice density is defined as the ratio of weight to volume.

The constitution and composition of ice are entirely determined by the hydrometeorological conditions of ice formation. Air temperature, wind conditions, sea currents, choppy weather, atmospheric precipitations, and sea water salinity are among the leading factors.

The structure of the ice cover was studied with the aid of photographs of ice sections taken in polarized light. The ice sections were prepared from plates cut from different horizons of the core. Specimens for density and salinity tests were cut from the same core. Salinity was determined by the standard water titration technique (and expressed according to the chlorine content). The quantitative content of salts in molten ice was determined with high precision (up to 0.01 — 0.02 per mill).

The ice density was determined by hydrostatic weighing.

The results described in this paper cover the period from June 1965 to June 1966.

 . Observations were carried out for ice of various ages. Four age groups were studied:

1) young autumn ice,
2) year-old ice,
3) two-year-old ice,
4) pack ice.

Observations of young autumn ice revealed characteristic fine-grained and inequigranular structure. There is a clear tendency to preferentially

vertical growth of crystals. The size of crystals increases with depth from 0.05 — 0.3 mm in the 0 — 5 cm layer to 1 cm and more in the 29 — 33 cm layer.

The vertical distribution of salinity is shown in Figure 1. We see from the figure that the salinity of young ice is insignificant in the top layers. This ice has anomalously low salinity because it formed from thawed water on the surface in openings. Its salinity on the surface was 0.8 — 1.7 per mill. In deeper layers, the salinity increased. As the ice layer becomes thicker, the salinity in the topmost part diminishes because of downward brine seepage.
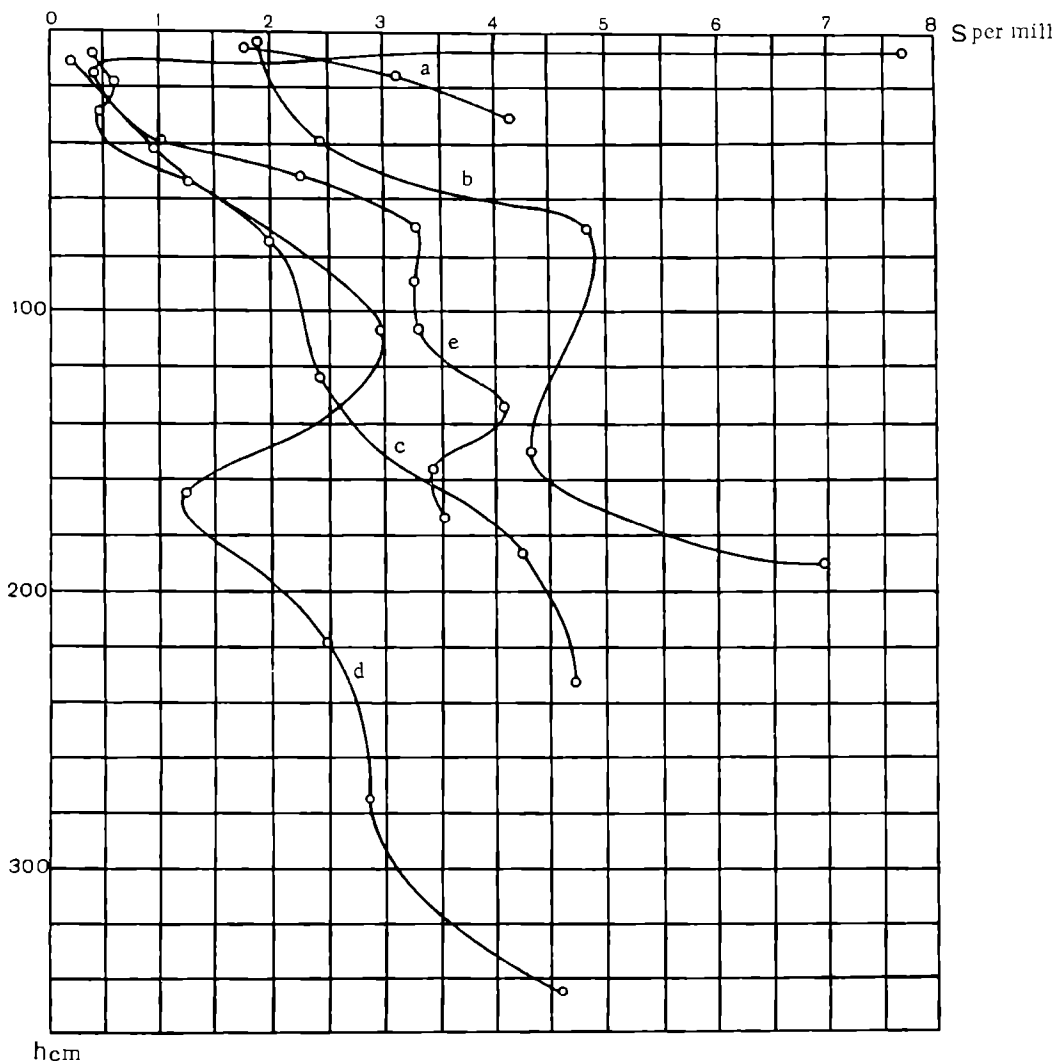
FIGURE 1. Distribution of salinity in sea ice:

a young ice; b, c year-old ice; d two-years-old ice; e pack ice.

Figure 2 shows the curves of the vertical distribution of density in ice of various age groups. The topmost layer of young ice is characterized by minimum density. This is attributed to the peculiar ice texture, which contains numerous air inclusions.

Studies of year-old ice 205 cm thick, carried out at the beginning of July, show that morphologically four layers of characteristic texture can be distinguished. The first layer (0—15 cm) is made of large-bubbly ice containing air inclusions of mostly spherical and oval shape. The second layer (15—55 cm) is ice of vertical filamental air inclusions. Then comes another layer (55—105 cm) of vertical filamental air inclusions, whose size, however, is somewhat larger and concentration somewhat lower. The last layer consists of water-saturated gray ice with occasional air inclusions.
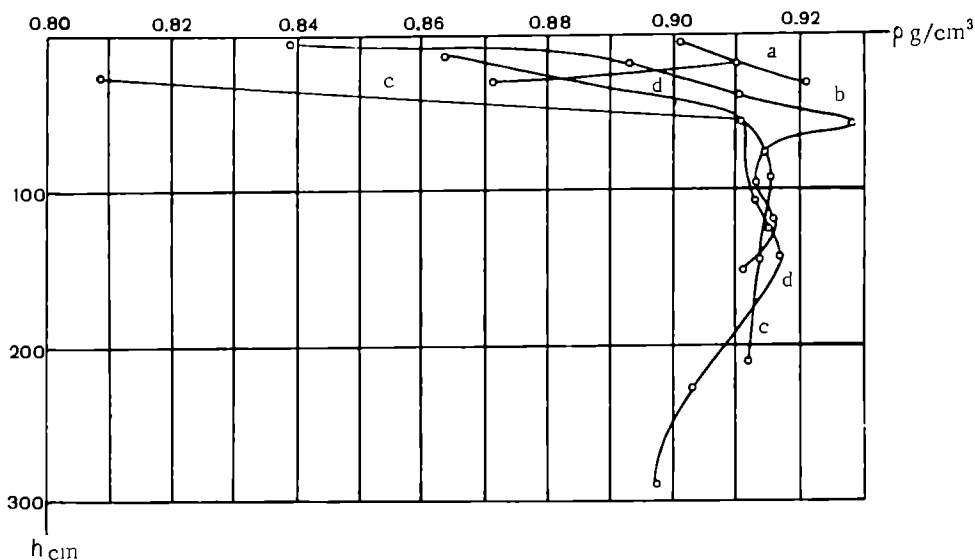
FIGURE 2.   Distribution of density in sea ice:

a   young ice; b   year-old ice; c   two-year-old ice; d   pack ice.

Examination of the crystal structure photographs shows that the ice in the 0—30 cm layer is coarse-grained, with isometric, irregular crystals, uniformly growing in all directions. The predominant crystal size is 1—2 cm. The next layer consists of ice of fibrous-columnar structure. The crystals are irregular, with serrated faces. The vertical size of crystals is from 1 to 5 cm and larger, and the horizontal size is from 0.5 to 1—2 cm. The lowermost layer is characterized by a more stable orientation of crystal growth.

The salinity measurements of year-old ice revealed a general trend in the distribution of the salt composition in water (Figure 1). The year-old ice has a maximum salinity in the topmost layers, since the period of ice formation was accompanied by pronounced entrapment of salts in the intergrain spaces.

The salinity levels out in spring and in summer and the maximum shifts into the lower layers because of brine migration. Enhanced brine migration into the lower-lying layers is the result of the higher temperature, the more pronounced porosity, and the increased content of the liquid phase in ice.

We see from Figure 2 that the topmost ice layer is always characterized by minimum density. In year-old ice, this is a consequence of brine migration and the peculiar features of ice formation which, under conditions

of large temperature gradients, proceeds with entrapment of large quantities of air.

Two-year-old ice reveals a 25 cm surface layer saturated with air inclusions up to 0.6 cm in diameter. This layer is characterized by fine-grained structure. The lower-lying layers display vertical-fibrous and fibrous structure with crystals up to 7 cm long and up to 1—2 cm across. The 26—27, 56—58, 88—92, and 111—115 cm horizons show distinct inter-layers of fine-grained ice.

Two-year-old ice is characterized by an overall reduction of salinity in the topmost layers. Vertical salinity profiles reveal a steady growth of salinity with depth (Figure 1).

The lower density of the topmost layers of two-year-old ice is attributable to its increased porosity, the result of summer thaw and seepage of thawed water through ice. The maximum thickness of the low-density top layer in two-year-old and pack ice is invariably reached at the beginning of the autumn ice formation period.

Pack ice 310 cm thick contained a visually discernible layer of large-bubbly ice between 0 and 30 cm. Below this layer, no stratification was noted in the core.

The 0—30 cm layer contained coarse-grained crystals from 0.5 to a few centimeters across. The 30—310 cm layer contained crystals of complex vertical-fibrous form. Their vertical dimensions varied from 1 to 5 cm, and horizontal from 0.2—0.3 to 1—2 cm.

As the age of ice increases, the salinity distribution changes. The topmost layers of pack ice are largely desalinated as a result of the downward seepage of brine in summer. The salinity distribution curve may have several maxima and minima associated with annual variations in the vertical distribution of the ice cover salinity. Low-salinity layers form from fresh water, which accumulates in summer under ice (Figure 1).

The distribution of pack ice density is similar to that observed for two-year-old ice.

A few remarks concerning the structure of the cores from ice formations of various age groups.

All cores show a bubbly top layer of grained structure. The thickness of this layer varies from 1—2 cm for young ice to 25—30 cm for year-old and pack ice.

Vertical-fibrous structure with highly irregular, complex-shaped crystals is characteristic of the middle and the bottom layers.

All ice formations have a so-called "lace" layer near the bottom surface. The "lace" is distinguished by an increased content of brine-filled capillaries. The thickness of the "lace" layer varies from 2—5 cm for young ice to 30—50 cm for year-old and pack ice. In summer, the capillaries merge and sea water penetrates into the ice to a distance of 50—60 cm from the top surface.

The presence of grainy interlayers in ice of vertical-fibrous structure, which are particularly prominent in cores of two-year-old ice, is attributable to large-scale influx of frazil crystals from hummocking regions.

Analysis of the salinity distribution curves of young, year-old, two-year-old, and pack ice leads to the following conclusions:

1. Salt migration is at its maximum during the formation of the surface ice layer and in the summer thaw period.

95

2. The period of winter ice growth is characterized by a stable salinity across the entire ice layer, although gradual redistribution of salts proceeds in the interior. Brine seepage is prevented by the continued freezing of water from below and the stoppering of the brine capillaries.

3. During the summer thaw, the downward migration of brine is enhanced because of the increase in porosity. The salinity reaches its maximum in the bottom layers of year-old and pack ice during this period, and stops increasing. Autumn temperatures again lead to freezing. The thawed water which seeped down through the ice cover or penetrated from nearby openings, lanes, and leads is the first to freeze. This effect is observed when the ice thickness does not exceed $2-2.5$ m. The ice layer forming from thawed water is characterized by very low salinity. Subsequent freezing of sea water is also accompanied by insignificant capture of salts, since the thick ice layer $(1.5-2.0$ m$)$ prevents rapid dissipation of the heat of crystallization. A second salinity maximum is therefore observed in the bottom layers toward the end of the second year.

The salinity distribution during the third year will apparently follow the same pattern.

Ice density measurements show that the maximum density occurs in the middle layers. Minimum density is characteristic of the top and the bottom layers. According to Savel'ev /4/, this is apparently a common pattern for all Arctic ice.

The bottom ice layer, in direct contact with sea water, is markedly weakened, being saturated with brine and water. Ice density is difficult to determine on these horizons, since most of the brine leaks out before the core samples are withdrawn to the surface. As a result, the density figures obtained for the lower horizons work out too low. This also explains the considerable scatter of the ice density data in the lower-lying layers: the final result depends to a large degree on the sampler's dexterity in withdrawing the cores for density measurement.

The sampling and density measuring procedure thus does not give reliable results for the density of the water-saturated ice at the bottom of the layer.

Let us consider the applicability of some theoretical considerations to the determination of the density of water-saturated ice.

Zubov (1945) /1/ gives the following equation relating the specific volume of sea ice to the salinity of the ice and the salinity of the brine in cells:

$$\theta = \frac{S_i}{S_b} \frac{1}{\rho_b} + \left(1 - \frac{S_i}{S_b}\right) \cdot \frac{1}{\rho_{0t}},\tag{1}$$

where θ is the specific volume of sea ice; S_i is the salinity of sea ice; S_b is the brine salinity; ρ_b is the density of the brine whose salinity is S_b at temperature of t°; ρ_{0t} is the density of pure solid (nonporous) ice at t°.

The specific volume of ice is equal to the reciprocal of its density,

$$\rho = \frac{1}{\theta}.$$

Expression (1) thus may be written in the form

$$\frac{1}{\rho_{St}} = \frac{S_i}{S_b} \frac{1}{\rho_b} + \left(1 - \frac{S_i}{S_b}\right) \cdot \frac{1}{\rho_{0t}}.\tag{2}$$

The ice densities computed from (2) for various temperatures and salinities of nonporous ice are listed in Table 1.

TABLE 1.

Salinity, per mill	Temperature, deg.							
	–2	–4	· 6	· 8	–10	–15	·-20	-23
2	0.924	0.922	0.920	0.921	0.921	0.922	0.923	0.923
4	0.927	0.925	0.924	0.923	0.923	0.923	0.925	0.925
6	0.932	0.928	0.926	0.926	0.926	0.925	0.926	0.926
8	0.936	0.932	0.929	0.928	0.928	0.928	0.929	0.929
10	0.939	0.935	0.931	0.929	0.929	0.929	0.930	0.930
15	0.953	0.944	0.939	0.937	0.935	0 934	0.935	0.935

Let us compare the results of some measurements with the corresponding data in the table.

7 September 1965, ice thickness 280 cm, density in the 260—270 cm layer 0.877 (hydrostatic weighing). The temperature of this layer was –1.4°C, salinity 3.75 per mill. The table approximately gives for these conditions (assuming a temperature of –2°C) a density of 0.926. Since equation (2) ignores air inclusions, the tabulated ice densities are naturally too high. We developed an alternative method for computing the density of water-saturated ice. The pores in ice were assumed to be filled with sea water, and we computed the volume of the gas-bubble pores (V_a) in 1 g of ice using the equality

$$V_a = \frac{0.9168 - \rho_i}{0.9168},$$ (3)

where 0.9168 is the density of pure pore-free ice; ρ_i is the measured ice density.

To reduce the computed ice density to the hydrostatic density, we apply a correction

$$\Delta\rho = \rho_{a\,St} V'_a,$$ (4)

where $\rho_{a\,St}$ is the density of sea water at temperature t and salinity S, V_a is the pore volume.

These densities of water-saturated ice are apparently still too high. However, they are closer to the true densities than the results obtained by hydrostatic weighing.

Bibliography

1. Zubov, N. N. L'dy Arktiki (Arctic Ice).— Leningrad, Gidrometeoizdat. 1947.
2. Pounder, E. R. The Physics of Ice. — Oxford, New York, Pergamon Press. 1965.
3. Peschanskii, I. S. Ledovedenie i ledotekhnika (Ice Science and Ice Technology).— Leningrad, Izdatel'stvo "Morskoi Transport." 1963.
4. Savel'ev, B. A. Stroenie, sostav i svoistva ledyanogo pokrova morskikh i presnykh vodoemov (Constitution, Composition and Properties of the Sea and Fresh-Water Ice Cover).— Izdatel'stvo MGU. 1963.

*V. V. Bogorodskii, G. V. Trepov, B. A. Fedorov,
and G. P. Khokhlov*

THE USE OF ELECTROMAGNETIC WAVES PROPAGATING IN FRESH WATER FOR ACTIVE PROBING AND OTHER PURPOSES

The acoustic field currently provides the only tool which is used on a wide scale for the detection and pinpointing of objects in water. This is also the principle used in various instruments, devices, and methods of physical investigation of water bodies. The electromagnetic field is hardly used for these purposes. This development has its roots in past history. In practice, measurements in saline water were generally encountered. Saline water is a conductor, so that electromagnetic waves do not propagate over practicable distances in it. As a result, a kind of suspicion developed with regard to the use of electromagnetic waves in water in general.

It can be shown, however, that the electromagnetic waves can be used with considerable success in fresh water.

One of the possible applications of electromagnetic waves in fresh water is for detection and ranging of objects (the bottom included) by means of radar.

If a directional beam of electromagnetic waves directed into fresh water is reflected from an object whose electromagnetic properties are different from those of water, the distance R to the object is expressed in terms of the delay time of the reflected signal relative to the primary signal:

$$R = \frac{ct}{2} \, \frac{1}{\sqrt{\frac{\varepsilon'}{2}(\sqrt{1+\tan^2\delta}+1)}} \, ,$$

where c is the electrodynamic constant, ε' is the permittivity of water, $\tan\delta$ is the dielectric loss angle of water.

The maximum detection range for a given energy potential and fixed antenna parameters is determined by the overall attenuation of the signal propagating from the antenna to the object and back. The attenuation (in dB) due to absorption in the medium is expressed by the relation

$$N = 40(\log e) R \frac{2\pi f}{c} \, \sqrt{\frac{\varepsilon'}{2}(\sqrt{1+\tan^2\delta}-1)} \, ,$$

where e is the base of natural logarithms, f is the frequency of the electromagnetic oscillations.

Figure 1 plots the curves of specific attenuation by absorption, computed from the electrical parameters of water (ε' and $\tan \delta$) published by various authors. For comparison, the same figures gives the specific attenuation curve of sweet ice at $-1°C$. We see from the figure that in a number of cases the attenuation in fresh water between 10^6 and $3 \cdot 10^7$ Hz does not exceed the attenuation in pure (sweet) ice. In view of the recent success in radar probing of "warm" glaciers, this fact indicates that radar probing in fresh water is not doomed to failure either.
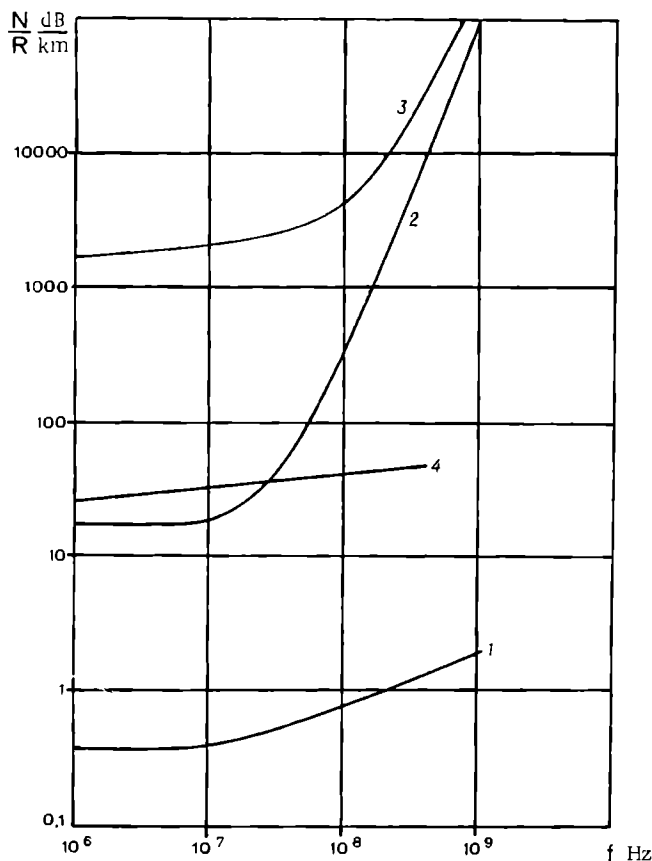
FIGURE 1. Frequency curves of the specific attenuation for distilled and fresh water /1, 2/ and for sweet ice /3/:

1) distilled water; 2, 3) fresh water; 4) sweet ice.

Computations of the overall attenuation of the radio signal carried out with allowance for absorption in water and the divergence of the beam also point to the applicability of radar probing to fresh water. Thus, a radar transmitter with 200 dB energy potential and antenna directivity of 3 ensures the following effective bottom-ranging distances at 10^7 Hz (for effective reflecting surface $S = \pi R^2$):

140,000 m for curve 1,
4,470 m for curve 2,
50 m for curve 3.

We see from the above results that even in the least favorable case (high dielectric losses, curve 3 in Figure 1) the effective range is by no means negligible.

Different modulations of the probing signal and different polarizations of the electromagnetic waves may be used for radar probing in fresh water.

We would like to mention a few useful facts concerning the application of electromagnetic wave probing in fresh water. Thus the permittivity of water is 80, and the foreshortening factor of the dipole antenna is about 9. Therefore, at low frequencies, highly directional multiunit antennas may be used. Another useful point for the radiation of electromagnetic waves from air into water is the presence of a matching ice layer on the surface of water.

Radar probing also can be used to determine the boundaries of freshwater bodies polluted by industrial effluents and to find the level of pollution. Water pollution can be determined by this method under field conditions, both in plan and in the vertical direction.

The water pollution measurements are conducted as follows. The probing unit, comprising a transmitting and a receiving antenna set up at a fixed distance from one another and having a certain mutual alignment, is moved in water. The electromagnetic field strength is measured at the point occupied by the receiving antenna. As the probing unit moves from "clean" water into polluted water, the field strength at the receiving antenna changes. The received signal level thus provides an indication of the boundaries of the polluted volume, and assuming that the dependence of absorption on pollutant concentration is known, the level of pollution also can be determined.

Our results indicate that electromagnetic waves can be used for communication and for the development of instruments and methods of physical measurement in fresh water.

Bibliography

1. Bogorodskii, V.V. and V.N.Rudakov. Elektromagnitnye para-metry snega, l'da, presnoi i morskoi vody (Electromagnetic Parameters of Snow, Ice, Fresh and Sea Water).—Primenenie radiofizicheskikh metodov v okeanograficheskikh i ledovykh issledovaniyakh. Leningrad, Izdatel'stvo AANII. 1965.
2. Bogoroditskii, N.P. and V.V.Pasynkov. Materialy v radio-elektronike (Materials in Radio-Frequency Electronics).—Moskva, Gosenergoizdat. 1965.
3. Evans, S. Dielectric Properties of Ice and Snow.—Journal of Glaciology, Vol. 5, No. 42. 1965.

V. V. Bogorodskii, G. V. Trepov, and B. A. Fedorov

TENSOR ELECTROMAGNETIC PROPERTIES OF GLACIER ICE

When a linearly polarized electromagnetic wave is radiated into an isotropic nongyrotropic medium (e.g., air), the reflected signal is maximum if the receiving dipole is parallel to the transmitting dipole.* In other words, an isotropic nongyrotropic medium does not possess polarizing properties.

Radar probing of glaciers revealed a certain depolarization of the radar signals: the reflected signal in general was elliptically polarized, and the maximum signal level was received with the dipole making a certain angle (in the horizontal plane) with the transmitting dipole. Since the polarization of signals reflected from targets in a glacier (permittivity inhomogeneities, glacier bed) does not coincide with the polarization of the transmitted signal, the complex permittivity $\dot{\varepsilon}$ of ice has to be treated as a tensor.

The depolarization of the signal propagating in the vertical direction through the glacier can be produced by one of the following three mechanisms.

The first mechanism involves anisotropy of the electromagnetic properties of the ice crystals. In sweet ice single crystals, the difference in the extraordinary and the ordinary refraction coefficients at 10 kHz is $n_e - n_0 = 5.00 - 4.69 = 0.31$ /1/, whereas in the optical spectrum $n_e - n_0 = 1.314 - 1.309 = 0.005$ /2/. We also know that the ice crystals in a glacier are ordered /3/, so that the optical axis of the crystals is normal to the plane of motion of the glacier. This mechanism is effective when the direction of wave propagation does not coincide with the optical axis of the crystals. The wave is decomposed into ordinary and extraordinary waves which propagate with different phase velocities through the medium, and this effect produces distinct depolarization. In general, the received signal is elliptically polarized, and linear polarization is possible only if the phase difference between the ordinary and the extraordinary wave at the reception point is a multiple of π.

Another mechanism involves the Faraday effect. In some media, in the presence of a magnetic field in the direction of wave propagation, the wave remains linearly polarized, but the plane of polarization is rotated. If the direction of the magnetic field is perpendicular to the direction of propagation, depolarization is also felt /4/.

The third mechanism involves depolarization by internal stresses in the medium. Some substances, and in particular glass, acquire tensor properties independent of their crystal structure when stressed. The

---

* The depolarizing properties of interfaces are generally ignorable.

significance of this mechanism in glaciers is fairly difficult to determine and it remains largely unknown.

The tensor properties of glaciers were studied during the 14th Soviet Antarctic Expedition near Molodezhnaya Station. A pulse-modulated radar transmitter was used in these experiments (440 MHz, 0.3μsec pulse duration). The transmitting antenna radiated horizontally polarized waves; the plane of polarization of the signals remained fixed during the experiments. The polarization of the reflected signal was determined by measuring the amplitude of the reflected pulses for different orientations of the receiving linear dipole in the horizontal plane (the receiving dipole was placed next to the transmitting dipole).

The polarization of the reflected signal can be determined from the polarization diagram, which plots the amplitude of the reflected signal as a function of the position angle of the receiving dipole relative to the transmitting dipole. Figure 1 shows the polarization diagrams for a non-polarizing medium (a) together with typical experimental diagrams (b, c) which indicate that the reflected signals are depolarized and have either linear (b) or elliptical (c) polarization. Table 1 lists the results of measurements carried out at 27 points. The observation points were selected at random and the table lists all the relevant data: the angle of rotation (in degrees) of the receiving dipole relative to the transmitting dipole for peak signal reception; the ellipticity, i.e., the ratio (in dB) of the maximum to minimum signal obtained with a rotating receiving dipole; the thickness of the glacier (in meters). The data for points 7, 14, 15, 20, 27 correspond to two signals reflected from the subglacier surface (two signals may appear when a morainic layer occurs near the glacier bed or if there is a break in the bed). If cases with the maximum signal exceeding the minimum signal at least by 14 dB are classified as linear polarization events,* we see from the table that the signal retained linear polarization in 25 out of 32 cases, and in 7 cases it acquired elliptical polarization. The data for observation points with two reflected signals (the time lag between the two signals is about $0.2\,\mu$sec, i.e., 16.7 m thickness) indicate that the bottom part of the glacier is a levorotating medium with a specific rotation of about 0.6 deg/m.
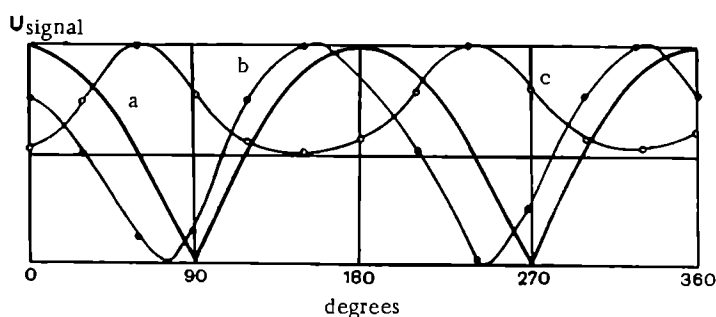

FIGURE 1. Polarization diagrams:

The vertical axis gives the signal amplitude in relative units; the horizontal axis marks the rotation angle of the receiving dipole relative to the transmitting dipole. The experimental points are marked on the curves.

---

* As the rotation angle was incremented in 30° steps, some of the deep minima were probably missed.

The results of these experiments indicate that the tensor properties of glacier ice rotate the plane of polarization of the radar signal and also cause (to a lesser extent) a change in polarization, i. e., a linearly polarized signal is converted into an elliptically polarized signal.

TABLE 1.

Measurement point	Rotation angle	Ellipticity	Glacier thickness, m	Measurement point	Rotation angle	Ellipticity	Glacier thickness, m
1	−30	>20	468	15	+15	>20	230
2	+30	>20	468		0	>20	251
3	−15	20	468	16	−60	6	301
4	+15	20	468	17	+15	>20	301
5	0	12	468	18	+10	>20	301
6	−60	12	468	19	−15	8	292
7	+15	>20	451	20	+30	14	292
	−15	>20	468		+15	>20	318
8	−15	>20	468	21	0	6	292
9	+30	14	305	22	−45	>20	458
10	−60	16	468	23	−10	>20	458
11	−45	6	226	24	0	>20	450
12	+30	>20	234	25	−30	11	350
13	+50	14	226	26	+45	>20	267
14	0	>20	259	27	−75	>20	200
	−15	>20	292		−85	>20	218

To corroborate the change in signal polarization, crossed dipoles were used to probe a glacier section of about 15 km with maximum thicknesses of more than 400 m. These measurements showed that the intensity of the signals reflected from the subglacier surface was the same on the average as in case of reception with parallel dipoles, whereas the signal intensity reflected from inhomogeneities in the upper part of the glacier is markedly lower than in the parallel-dipole case (by 20 dB and more).

The depolarization of radar signals in ice can be used for practical purposes. It reduces the fluctuations of the signals reflected from the subglacial surface and suppresses the signals reflected from inhomogeneities in the top part of the glacier. At a more advanced stage, depolarization effects will probably enable us to investigate the stressed state of the glacier and its crystal structure.

Bibliography

1. Humbel, F., F. Jona, and P. Scherrer. Anisotropie der Dielek-
    trizitätskonstante des Eises. — Helvetica Physica Acta, Vol. 26,
    Fasc. 1, p. 17—32. 1953.
2. Rudakov, V. N. and V. V. Bogorodskii. K voprosu ob izmerenii
    tolshchiny lednikov elektromagnitnymi metodami (Measuring the
    Thickness of Glaciers by Electromagnetic Methods). — ZhTF, 30,
    No. 1. 1960.
3. Shumskii, P. A. Osnovy strukturnogo ledovedeniya (Elements of
    Structural Ice Physics). — Moskva, Izdatel'stvo AN SSSR. 1955.
4. Grudinskaya, G. P. Rasprostranenie radiovoln (Propagation of Radio
    Waves). — Moskva, Izdatel'stvo "Vysshaya Shkola". 1967.

V. P. Gavrilo, A. V. Gusev, and D. B. Dianov

RADIAL OSCILLATIONS OF AN ICE SPHERE IN WATER

Ice breaking is a common phenomenon in nature. When the ice cover of rivers and lakes breaks, ice fragments will often accumulate on the shore and may clog various hydroengineering structures. Hummocks several meters high were observed near the shores of Lake Ladoga. The acoustic effect which accompanies ice breakage may reach considerable strength in air. The noise spectrum of breaking ice in air is described in /1/. When river and lake ice breaks (which is generally accompanied by fragmentation of large ice fragments into smaller ones, impact, friction, etc.), oscillations may often be excited in the ice fragments falling into water (as in any other solid object). It is therefore advisable to analyze the natural frequencies of elastic objects in water, whose density is close to the density of water.

We will determine the natural frequencies (or the oscillation modes) of an ice sphere ($\rho = 0.9\,\text{g}/\text{cm}^3$) in a liquid medium ($\rho = 1\,\text{g}/\text{cm}^3$). The general problem of the radial oscillations of an elastic sphere was solved for the case of a medium with a much lower density than the density of the oscillating sphere /2/. The amplitude spectrum of the oscillation modes of the sphere was calculated on a computer.

Consider a sphere of radius R, whose material is characterized by density ρ and elastic constants λ and μ. The sphere is immersed in a liquid of density ρ_0, whose elastic properties are characterized by the speed of sound c_0.

Let us first consider the forced oscillations of the sphere, assuming a time-harmonic ($e^{-i\omega t}$) external radial stress $\sigma = \sigma_m e^{-i\omega t}$ acting on the surface of the sphere. Because of the spatial symmetry of the external forces, radial oscillations will be excited in the sphere. Dropping the time factor, we write the solution of the wave equation for the sphere in the form

$$\varphi = A\,\frac{\sin kr}{r}. \tag{1}$$

Similarly, for the field in the surrounding liquid

$$\varphi_0 = B\,\frac{e^{ik_0 r}}{r}. \tag{2}$$

Here φ and φ_0 are the elastic displacement potentials; $k = \dfrac{\omega}{c_l}$ and $k_0 = \dfrac{\omega}{c_0}$ are the wave numbers; $c_l = \sqrt{\dfrac{\lambda + 2\mu}{\rho}}$ and c_0 are the velocities of longitudinal

waves in the sphere and in the liquid. Using the boundary conditions for $r=R$ (continuity of radial displacements and radial stresses), we obtain a set of two equations

$$A\left[-c_i^2\rho\frac{k^2\sin kR}{R}+4c_i^2\rho\left(\frac{\sin kR}{R^3}-\frac{k\cos kR}{R^2}\right)\right]+B\frac{c_0^2\rho_0 k_0 e^{ik_0R}}{R}=-\sigma_m;$$

$$(3)$$

$$A\left(\frac{k\cos kR}{R}-\frac{\sin kR}{R}\right)+B\left(\frac{e^{ik_0R}}{R}-\frac{ik_0e^{ik_0R}}{R}\right)=0.$$

Here $c_t=\sqrt{\dfrac{\mu}{\rho}}$ is the velocity of propagation of transverse waves in the sphere material. Solving (3) with the aid of (1) and (2), we find

$$\varphi_0=\frac{\sigma_m R^3\dfrac{1}{\rho c_i^2}\;(kR\cos kR-\sin kR)}{\Delta}\;\frac{e^{ik_0(r-R)}}{r},\qquad(4)$$

$$\varphi=\frac{-\sigma_m R^3\dfrac{1}{\rho c_i^2}(1-ik_0R)}{\Delta}\;\frac{\sin kr}{r},\qquad(5)$$

where

$$\Delta=-(kR)^2\sin kR-4\left(\frac{c_t}{c_i}\right)^2(kR\cos kR-\sin kR)-$$

$$-\frac{\rho_0 c_0^2}{\rho c_i^2}\;(k_0R)^2(kR\cos kR-\sin kR)+i\Big[(k_0R)(kR)^2\sin kR+$$

$$+4(k_0R)\left(\frac{c_t}{c_i}\right)^2(kR\cos kR-\sin kR)\Big].\qquad(6)$$

Changing over to other elastic field characteristics (the sound pressure P_0 for the liquid and the elastic displacement u_r for the sphere), we find

$$P_0=\frac{\sigma_m R\dfrac{\rho_0}{\rho}(kR)^2(kR\cos kR-\sin kR)}{\Delta}\;\frac{e^{ik_0(r-R)-i\omega t}}{r},\qquad(7)$$

$$U_r=\frac{-\sigma_m R^3\dfrac{1}{\rho c_i^2}(1-ik_0R)(kr\cos kr-\sin kr)}{\Delta r^2}\;e^{-i\omega t}.\qquad(8)$$

The above expressions show that, if the effect of the liquid is ignorable $(c_0\to0,\ \rho_0\to0)$, expression (6) retains only the term with i. Setting this term equal to zero, we find the eigenfrequencies of a free sphere:

$$\tan kR=\frac{4\left(\dfrac{c_t}{c_i}\right)^2(kR)}{4\left(\dfrac{c_t}{c_i}\right)^2-(kR)^2}.\qquad(9)$$

105

Let us consider some particular cases of equation (9). For $\nu = 0.5$ (ν is Poisson's ratio), equation (9) takes the form

$$\tan kR = 0, \tag{10}$$

when we obtain the resonance frequencies

$$f_1 = \frac{c_l}{2R}; \quad f_2 = 2\frac{c_l}{2R}; \quad f_3 = 3\frac{c_l}{2R}; \ldots \tag{11}$$

For $\nu = 0$, equation (9) takes the form

$$\tan kR = \frac{2(kR)}{2 - (kR)^2}. \tag{12}$$

The roots of equation (12), by /3/, are

$$kR = 119.26\frac{\pi}{180}; \quad kR = 340.35\frac{\pi}{180}; \ldots,$$

and since $k = \dfrac{\omega}{c_l} = \dfrac{2\pi f}{c_l}$, we have

$$f_1 = \frac{119.26}{180}\frac{c_l}{2R}; \quad f_2 = \frac{340.35}{180}\frac{c_l}{2R}; \ldots,$$

i.e.,

$$f_1 = 0.664\frac{c_l}{2R}; \quad f_2 = 1.89\frac{c_l}{2R}.$$

In the particular case $\nu = 0.25$, equation (9) gives the following resonance frequencies:

$$f_1 = 0.82\frac{c_l}{2R}; \quad f_2 = 1.93\frac{c_l}{2R};$$

$$f_3 = 2.95\frac{c_l}{2R}; \tag{13}$$

The above examples show that the introduction of shear elasticity somewhat lowers the eigenfrequencies of the sphere.

The nonsteady-state problem of the oscillations of an elastic sphere in a liquid can be solved using the Fourier transformation. Suppose that the external stresses are constant, vanishing abruptly at time $t = \tau$. The spectrum of a step function

$$\sigma_0(t - \tau) = \begin{cases} 1 & t < \tau, \\ 0 & t \geqslant \tau \end{cases} \tag{14}$$

is given by

$$S_0 = \int_{-\infty}^{\infty} e^{i\omega t}\sigma_0(t - \tau)\,dt = \frac{e^{i\omega\tau}}{i\omega}. \tag{15}$$

Fourier transformation gives

$$P(t) = \frac{1}{2\pi} \int_{-\infty}^{\infty} S_0(\omega) P(\omega) e^{-i\omega t} \, d\omega.$$ (16)

The sound pressure $P(\omega)$ in the liquid is expressed in the form

$$P(\omega) = \frac{\sigma_m R \frac{\rho_2}{\rho_1} (k_1 R)^2 (k_1 R \cos k_1 R - \sin k_1 R)}{\Delta} \frac{e^{i k_2 (r - R) - i\omega t}}{r}.$$ (17)

Inserting (17) in (16), we find

$$P_0(t) = \frac{-\sigma_m}{2\pi} R \frac{\rho_0}{\rho} \frac{i}{r} \int_{-\infty}^{\infty} \frac{e^{i\omega \tau}}{\omega} \frac{(kR)^2 (kR \cos kR - \sin kR)}{\Delta} e^{i k_0 (r - R) - i\omega t} \, d\omega.$$ (18)

The integration in (18) can be carried out using the theory of analytical functions. The denominator of the integrand vanishes at points of the complex plane which lie above the real axis. Expression (18) can be expressed as an infinite sum of residues at the poles of the integrand. This requires numerical solution of a system of two transcendental equations which are obtained when (6) is set equal to zero.

The spectrum of the radiation field of a sphere undergoing free damped oscillations in a liquid may be written on the basis of (18).

The complex spectrum is

$$\Phi_{P_0}(\omega) = \frac{(kR)^2 (kR \cos kR - \sin kR) e^{i\omega \tau + i k_0 (r - R)}}{\omega \Delta}.$$ (19)

The magnitude of (19) gives the amplitude spectrum of the sound field radiated by the sphere.

If we assume that the external stress is applied for a very brief time $\Delta \tau$, we find $S_0(\omega) = \Delta \tau e^{i\omega \tau}$, where τ is the time when the external stress is switched on. In this case (apart from a constant)

$$|\Phi_{P_0}(\omega)| = \left| \frac{(kR)^2 (kR \cos kR - \sin kR)}{\Delta} \right|.$$ (20)

Figure 1 shows the relative amplitude spectra computed on the URAL-2 computer using (19) for spheres with radii of 1, 5, 10, 20, and 50 cm. The computations were carried out for $c_0 = 1500$ m/sec, $c_l = 3200$ m/sec, $c_t = 1600$ m/sec. The table lists the resonance frequencies of elastic ice spheres in vacuum f_0 according to (9) and in water f_w according to (20)

R, cm	1	5	10	20	50	100
f_0, kHz	125.00	25.00	12.50.	6.25	2.50	1.25
f_w, kHz	100	20	10	5	2	1

We see from the table that the surrounding water medium may substantially lower the resonance frequencies of free oscillations. According to computations, this lowering is $\left(1 - \dfrac{f_w}{f_0}\right) \times 100\% = 20\%$.
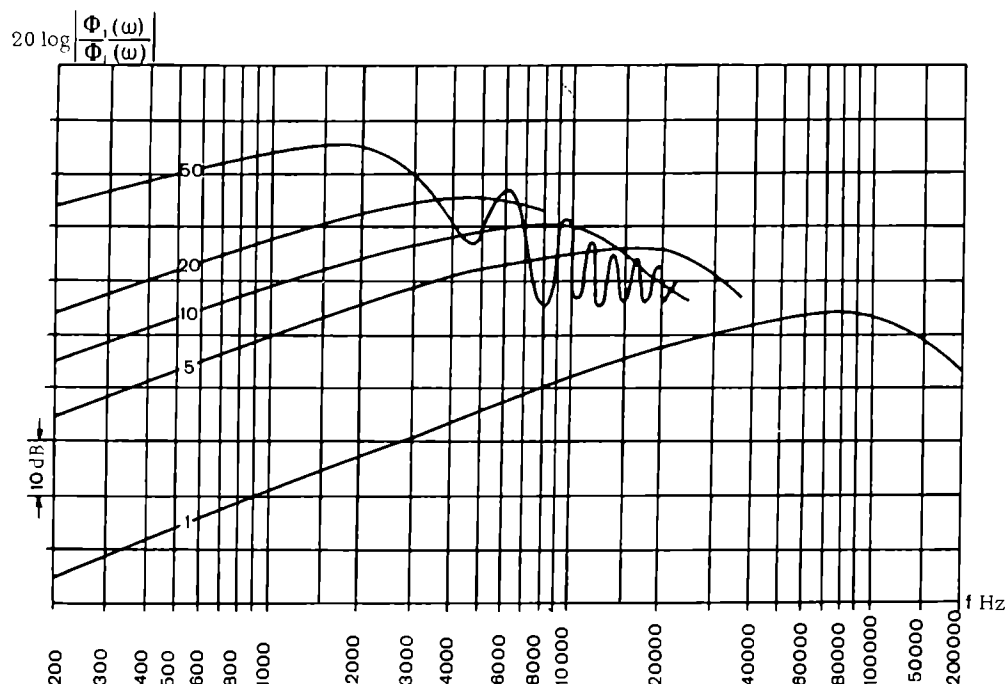

FIGURE 1. Amplitude spectra of the sound field radiated by ice fields with radii of 1, 5, 10, 20, and 50 cm.

The effect of water on the oscillation frequencies of ice specimens was also assessed in special experiments carried out in the AANII refrigeration chamber using an IChMK-2 mechanical frequency meter.* In this experiment, we measured and compared the resonance frequencies of the longitudinal oscillations in an ice rod suspended in air and in water.

The resonance frequencies of rod-shaped ice specimens ($27 \times 6 \times 3$ cm) in water are on the average $15-20\%$ lower because of energy losses and the effect of the additional water mass.

Analysis of the oscillations of an elastic sphere in water thus leads to the following conclusions:

1. An ice body immersed in water and subjected to an external stress will excite outgoing spherical waves in the surrounding medium when the stress is suddenly relieved (i. e., when the ice breaks into smaller fragments). The sound pressure in the liquid is described by a damped sine curve. The sine frequency is equal to the natural frequency of the object, which depends on the size of the oscillating body, its elastic properties, and the additional mass of the surrounding medium. The actual variation of the elastic properties of ice observed in nature affects the resonance

---

* IChMK-2 is designed for measuring the natural frequencies of flexural, longitudinal, and torsional oscillations of solid specimens of circular and rectangular cross sections.

frequencies to a much lesser extent than the changes in body size do. This is understandable if we examine the ratio of the propagation velocities of the longitudinal and transverse waves $\frac{c_l}{c_t}$, entering the expression for the spectrum of the radiation field of the sphere. According to /4/, this ratio is constant, being equal approximately to 2, and c_l varies at most by 10% as a result of ice temperature variation under natural conditions.

2. The spectrum of sound oscillations radiated by an ice sphere in water (when the conditions listed under item 1 above are satisfied) is continuous and it is displaced in the direction of low frequencies compared to the spectrum of free oscillations of an elastic sphere in vacuum.

An estimate of the resultant spectrum of the disturbance produced by the simultaneous oscillations of several ice bodies of different size can be obtained by adding the spectra of the individual objects.

Bibliography

1. Arabadzhi, V.I. O zvuke, voznikayushchem pri droblenii l'da (The Sound Accompanying Ice Fragmentation). — Akusticheskii Zhurnal, Vol. 14, No. 3. 1968.
2. Landau, L.D. and E.M. Lifshits. Teoriya uprugosti (Theory of Elasticity). — Izdatel'stvo "Nauka". 1965.
3. Jahnke, E. and F. Emde. Tafeln höherer Funktionen, 6th edn. — Stuttgart, B.G. Teubner. 1960.
4. Bogorodskii, V.V. Impul'snyi ul'trazvukovoi metod issledovaniya fizicheskikh svoistv l'dov (A Pulsed Ultrasonic Method for Studying the Properties of Ice). — Trudy seminara po fizike i primeneniyu ul'trazvuka, LETI im. V.I. Ul'yanova (Lenina), Leningrad. 1958.

A. E. Kolesnikov and A. V. Prokof' eva

CALIBRATION OF SPHERICAL PIEZOTRANSDUCERS IN ICE

The fast growth of the volume of scientific research work done in the Arctic and the Antarctic often necessitates measurements of sound oscillations propagating in ice. Piezotransducers are generally used as sensing elements. Let us estimate the range of reception of sound oscillations by a spherical piezotransducer and carry out an absolute calibration.

A wave field in a solid medium may be described as a sum of two fields, one corresponding to dilation waves

$$\frac{1}{c_1^2}\frac{\partial^2\varphi}{\partial t^2} = \nabla^2\varphi, \tag{1}$$

where c_1 is the propagation velocity of longitudinal waves, and the other to distortion waves

$$\frac{1}{c_2^2}\frac{\partial^2\overline{\psi}}{\partial t^2} = \nabla^2\overline{\psi}, \tag{2}$$

where c_2 is the propagation velocity of transverse waves.

Let us consider the oscillations of a sphere in an unbounded elastic medium. The origin of coordinates is placed at the center of the sphere and spherical coordinates r, θ, α are introduced. The wave equation (1) in spherical coordinates takes the form

$$\frac{1}{r^2}\frac{\partial}{\partial r}\left(r^2\frac{\partial\varphi}{\partial r}\right) + \frac{1}{r^2\sin\theta}\frac{\partial}{\partial\theta}\left(\sin\theta\frac{\partial\varphi}{\partial\theta}\right) = \frac{1}{c_1^2}\frac{\partial^2\varphi}{\partial t^2}. \tag{3}$$

Because of axial symmetry, φ is independent of α.

After a number of mathematical manipulations, the solution of this equation can be written in the form /1/

$$\varphi = \sum_{m=0}^{\infty}(-1)^m b_m(2m+1)h_m^2(kr)P_m(\cos\theta), \tag{4}$$

where h_m^2 are Hankel's spherical functions of second kind; $P_m(\cos\theta)$ are Legendre polynomials; $kr = \dfrac{2\pi r}{\lambda_1}$; $\lambda_1 = \dfrac{c_1}{f}$.

The vector potential $\overline{\psi}$ is chosen so that in spherical coordinates it has only one nonzero component $\psi_\alpha = \psi$. The solution of equation (2), using (3),

is then written in the form

$$\psi = \sum_{m=1}^{\infty} (-i)^m a_m (2m+1) h_m^2 (qr) P_{m,1}(\cos \vartheta), \tag{5}$$

where $P_{m,1}$ is the adjoint Legendre polynomial; $qr = \dfrac{2\pi}{\lambda_2}$; $\lambda_2 = \dfrac{c_2}{f}$.

In the far zone $(kr \gg 1; gr \gg 1)$

$$\varphi = \frac{ie^{-ikr}}{kr} \sum_{m=0}^{\infty} (2m+1) b_m P_m (\cos \theta),$$

$$\psi = \frac{ie^{-iqr}}{qr} \sum_{m=1}^{\infty} (2m+1) a_m P_{m,1}(\cos \theta). \tag{6}$$

The coefficients b_m and a_m are determined from the boundary conditions for the velocity on the surface of the sphere. In general, the radiation field of a sphere consists of longitudinal and transverse waves. The longitudinal waves, in their turn, are generated by pulsating modes $(m = 0)$, oscillating modes $(m = 1)$, spheroidal modes $(m = 2)$, and higher order modes. In the field of transverse waves, the pulsating component is zero and the oscillating mode is the lowest.

Thin-walled spheres of piezoelectric ceramics are successfully used in acoustic measurements. These detectors comprise a spherical shell made of radially polarized ceramic with metal coating from the inside and from the outside; the metal layers constitute the capacitor electrodes. If an exciting voltage is applied to the terminals of the piezoelectric transducer, it will emit longitudinal spherical waves, spheroidal waves, and higher order waves, as well as transverse waves (for radiation in a solid medium) starting with the second mode and higher. The first mode, which is not related to to the deformation of the piezotransducer, is missing from the spectrum of the sphere.
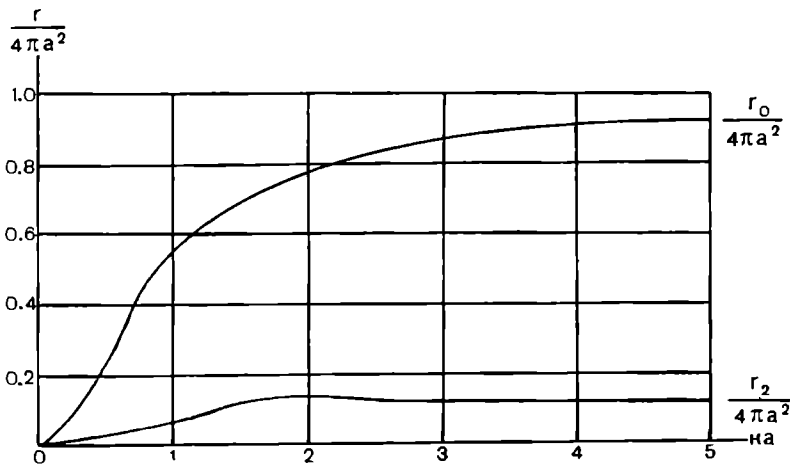

FIGURE 1. Reduced radiation resistance as a function of the parameter ka for longitudinal $\left(\dfrac{r_0}{4\pi a^2}\right)$ and transverse $\left(\dfrac{r_2}{4\pi a^2}\right)$ modes.

The active radiation resistance of the zero-order source is /2/

$$r_0 = \rho_m c_m \frac{4\pi k^2 a^4}{1 + k^2 a^2},\tag{7}$$

where ρ_m is the density of the medium; c_m is the velocity of sound in the medium; $k = \frac{2\pi}{\lambda}$; λ is the wavelength in the medium; a is the radius of the sphere. The active resistance of the second-order oscillator is

$$r_2 = \frac{4}{15}\rho_m c_m \frac{4\pi k^6 a^8}{k^6 a^6 - 2k^4 a^4 + 9k^2 a^2 + 81}.\tag{8}$$

The field of a spherical source consisting of oscillators of different orders which radiate all with equal amplitudes in the long-wave region is mainly determined by the radiation resistance of the lowest order. In the frequence range between 5 and 20 kHz, the radiation field of the longitudinal waves is therefore determined by the pulsating modes, whereas the field of the transverse waves is determined by the spheroidal modes, which are the lowest order mode present for transverse oscillations. Comparison of the radiation resistances for longitudinal and transverse waves (Figure 1) indicates that the longitudinal modes are dominant in the spectrum of a thin-walled piezoceramic sphere between 5 and 20 kHz. The velocity of the longitudinal waves in ice was taken equal to 3600 m/sec, and the velocity of transverse waves to 1800 m/sec /3/.

The intensity of transverse modes increases at higher frequencies, when the nonuniformity of the applied external stress on the spherical piezoceramic surface is felt, but it nevertheless remains substantially lower than the intensity of longitudinal modes. It follows from the above that the oscillations of a spherical transducer both in water and in ice are mainly determined by the longitudinal pulsating mode. The transverse modes in ice can be ignored.

The reciprocity principle leads to the following expression for the response of spherical detectors to longitudinal waves:

$$M = \frac{4\pi a d\, d_{31}}{\omega S_c \sqrt{1 + \left(\frac{\omega}{c_{\text{long}}}\right)^2 a^2}\, \varepsilon_{33}\left(1 - k_r^2\right)\left[\left(\omega M_s - \frac{1}{\omega c_t} - \frac{n^2}{\omega c_s}\right)^2 + \frac{4\pi a^4 k^2 \rho_m c_{\text{long}}}{1 + k^2 a^2}\right]^{1/2}},\tag{9}$$

where d is the thickness of the sphere walls; ε_{33} is the dielectric constant of the sphere material, S_c is the elastic compliance in the radial direction; k_r is the electromechanical coupling coefficient for radial oscillations of the sphere; d_{31} is the piezoelectric modulus of the medium; M_s is the mass of the sphere; c_t is the elasticity of the thin spherical shell; c_s is the capacitance of the sphere; n is the coefficient of electromechanical conversion.

For relative estimates of the piezotransducer response in water and in ice at frequencies below the first resonance, we must introduce a diffraction correction, as diffraction is largely determined by the relationship between

the detector diameter and the ultrasound wavelength. The diffraction term in (9) is expressed in terms of $\sqrt{1 + k^2a^2}$. Figure 2 shows the computed response characteristics of a spherical piezoelectric transducer 50 mm in diameter (95 % $BaTiO_3$ and 5% $CaTiO_3$) in water and in ice (the numerical values of the piezoelastic constants were taken from /4/). We see that the two response curves diverge at frequencies higher than 5 kHz: in water the diffraction effects at these frequencies are pronounced, whereas in ice they are virtually nil. These calculations are highly approximate, since a number of restrictions were introduced in the derivation of the response formula: we ignored internal friction, inhomogeneities of the real sphere, the effect of the cable coupling, the scatter of piezoelastic constants of the materials, etc. Nevertheless, relation (9) correctly reflects the difference in response in water and in air.
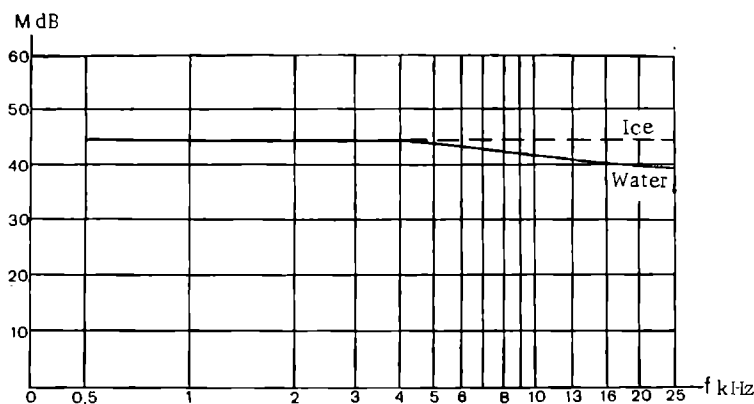
FIGURE 2. A theoretical frequency characteristic of the response of spherical piezotransducers in water and in ice.

Absolute calibration is needed in order to determine the response of the transducers in ice. A number of methods are known for absolute calibration of hydrophones (i.e., calibration without a comparison standard): electrostatic calibration (with an additional electrode), the Rayleigh disk method, calibration by measuring the input resistance, the reciprocity method /5/, but unfortunately not all of them are applicable in a solid medium.

Let us consider calibration by the reciprocity method. No special apparatus is required and no acoustic variables need be measured. The measurements are restricted to determination of distance and two ratios of electrical signal. The frequency characteristic of the receiving channel is of no importance; it may even be nonuniform, since all the individual measurements are relative. The only requirement to be met by the equipment is that it should be linear. Moreover, this method can be applied to determine the absolute response under actual working conditions. This is particularly important since field measurements generally suffer from variable temperatures and variable ice densities; moreover, the elastic constants of ice are never the same over the entire field.

Hydrophone calibration in ice under laboratory conditions involves certain difficulties: the production of large volumes of ice is not a simple undertaking. It is therefore advisable to use the reciprocity method for calibration over short distances. In this case, sounding measurements can be made

without running the risk of reflection from the walls of the specimen. Piezoceramic spheres 50 mm in diameter are virtually isotropic up to frequencies around 25 kHz in ice. Directional errors for stationary detectors in ice are thus avoided. Some authors /6, 7/ carried out theoretical and experimental analysis of the calibration of transducers at a small distance from one another.

We established that the response of a sphere 50 mm in diameter as determined after calibration by the reciprocity method for a separation of $r = 7$ cm between the centers coincides with the response for a separation of about $r \geqslant 50$ cm.

The lower calibration frequency is determined approximately by the relation of the wavelength to the linear dimensions of the volume:

$$\lambda_{max} \leqslant \frac{h}{5} .$$

where h is the side of the ice cube. Hence $\lambda_{max} = 40$ cm for $h = 200$ cm, which corresponds to $f_t = 9000$ Hz (assuming longitudinal waves). The upper calibration frequency is found from the requirement that there be no standing waves between the two transducers; experimentally it was found to be 20 kHz. The reliable calibration range thus extends from 9 to 20 kHz.

The detector response is found from the expression

$$M = \sqrt{\frac{E_1 E_3 2 R r}{E_2 E_4 \rho f}} \cdot 10^6 \ \mu V / N \cdot m^2, \qquad (10)$$

where r is the calibration separation, R is the resistance in ohm, M is expressed in dB per $1 \mu V / N \cdot m^2$; E_1, E_2, E_3, E_4 are the voltages at the receiver channel input for various positions of the selector switch /5/.
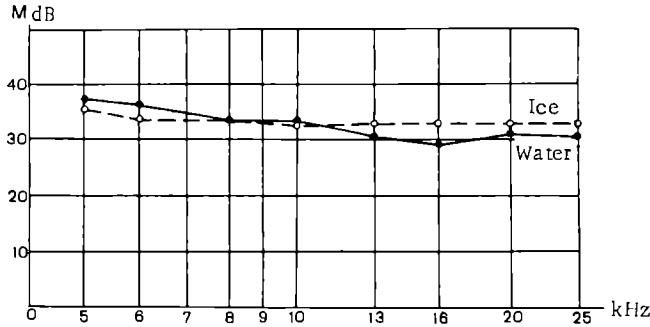

FIGURE 3. Experimental frequency response curve of spherical piezotransducers in water and in ice.

Figure 3 plots the average response in water and in ice from six measurements. The rms error of the results of six measurements does not exceed ± 0.4 dB. The curves in the figure show that at frequencies between 8 and 13 kHz the transducer response is approximately the same in water and ice (the results between 5 and 8 kHz are uncertain because of the limited ice volume). Above 13 kHz, diffraction effects are noticeable in water, and the response in ice is therefore 2 − 4 dB higher than in water, in good agreement with the theoretical curves.

114

Our results thus indicate that the response of a piezoceramic sphere in ice has a flatter characteristic than in water, and in absolute values it approximately corresponds to the low-frequency response in water. Because of the smaller diffraction effects at sound frequencies, the response in ice is $2-4$ dB higher than the response in water.

Bibliography

1. Sivukhin, D. V. Difraktsiya ploskoi zvukovoi volny na sfericheskoi ploskosti (Diffraction of a Plane Sound Wave on a Spherical Surface).— Akusticheskii Zhurnal, Vol. 1, No. 1. 1955.
2. Rzhevkin, S. N. Kurs lektsii po teorii zvuka (Lectures on the Theory of Sound).— Izdatel'stvo MGU. 1960.
3. Bogorodskii, V. V. Uprugie kharakteristiki l'da (Elastic Properties of Ice).— Akusticheskii Zhurnal, Vol. 4, No. 1. 1958.
4. Mason, W. P. (editor). Physical Acoustics, Principles and Methods, Vol. I: Methods and Devices.— N. Y., Academic Press. 1964.
5. Klyukin, I. I. and A. E. Kolesnikov. Akusticheskie izmereniya v sudostroenii (Acoustic Measurements in Ship Building).— Sudostroenie. 1968.
6. Yampol'skii, A. A. Absolyutnaya graduirovka elektricheskikh preobrazovatelei metodom vzaimnosti v kvazisfericheskom pole (Absolute Calibration of Electrical Transducers by the Reciprocity Method in a Quasispherical Field).— Trudy Komissii po akustike, No. 8. 1955.
7. Krishtalevich, A. N. and A. V. Rimskii-Korsakov. Nekotorye zamechaniya k opredeleniyu chuvstvitel'nosti mikrofonov metodom vzaimnosti (Some Remarks Concerning the Determination of Microphone Response by the Reciprocity Method).— Trudy Komissii po akustike, Sbornik No. 8. 1955.

V. P. Gavrilo and A. V. Gusev

ACOUSTIC PULSES PRODUCED BY IMPACT EXCITATION OF FLOATING ICE

The solution of some problems associated with the use of ice roads and air fields, effective ice-breaking methods, and ice protection of hydropower installations requires comprehensive study of the properties of ice in the natural environment and investigation of the processes which accompany ice breakage in nature. The present paper considers the particular topic of acoustic pulses generated by excitation of floating ice.

Special field work was carried out at the Lake Ladoga Research Station of the AANII in order to study some characteristics of the acoustic energy radiated into water as a result of collision between ice and a solid object. Such parameters as collision time, impact stresses, maximum impact acceleration, the velocity of elastic waves in ice, etc., were also determined experimentally.

The following experimental procedure was used. Solid objects (spherical steel casts of 300 and 156 kg) were dropped onto the ice surface. The impact was picked up by an electric strain acceleration gage attached to the dropping weight. The elastic vibrations of ice were picked up by seismic detectors mounted on the surface. The acceleration and seismic wave recording was done continuously during and after impact using appropriate electronic equipment.

The tests were carried out between 10 and 27 February 1967 on snow-covered winter ice, after a prolonged spell of low temperatures hitting −20 to −30°C. The measurements were carried out at a distance of 350 m from the shore, where the lake was 3 — 3.5 m deep. The ice was about 65 cm thick, and the snow cover was about 20 cm thick. The noise in water and the vibrations in ice were recorded with special measuring equipment, including a sound-frequency hydrophone, and a two-channel wide-band amplifier with discrete gain control. A M-75 magnetic tape recorder and a N-105 loop oscillograph were used as the recording terminals. The incoming signals were monitored with SI-1 cathode-ray oscilloscope.

An impact pulse picked up by the acceleration gage AG is bell-shaped (Figure 1); sinusoidal free oscillations of the gage with a frequency of about 600 Hz are superimposed on this pulse. The impact duration is close to 0.01 sec. The collision time is largely insensitive to the impact velocity and the energy of the falling body (under the conditions of our experiment); it is significantly dependent on the mass of the impacting object, however.

The velocity of sound in ice was measured in order to determine the modulus of normal elasticity of ice. The measurements were carried out with contact vibrographs using a separation $l_b = 63.9$ m. The difference Δt

in the time of arrival of longitudinal waves gave the velocity of sound
$c=\dfrac{l_b}{\Delta t}$. Figure 1 shows the oscillograms of the elastic vibrations of ice,
as recorded by the two vibrographs VG1 and VG2. The modulus of elasticity
was computed from the relation $E=\rho c^2$. Young's modulus determined in this
way was bound to be around $95 \, \text{ton}/\text{cm}^2$.
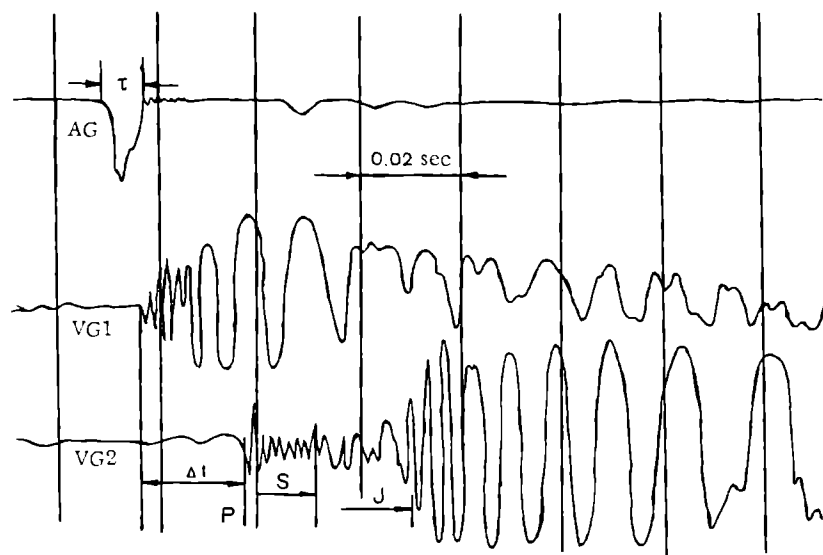

FIGURE 1. Oscillograms of the elastic vibrations of ice in the 30—800 Hz
band for a steel weight impacting on the ice surface.

The different types of waves propagating in ice are clearly distinguish-
able in Figure 1. The first arrival corresponds to the longitudinal elastic
wave (P wave) of relatively small amplitude. It is followed by displace-
ments produced by transverse (S) and flexural (J) waves. In case of a
strong impact, the vibrograph situated sufficiently close to the impact
point (VG1) recorded both the transverse vibrations produced by the shear
wave and by flexural waves, and also the transverse vibrations associated
with the passage of longitudinal waves and attributable to the Pochhammer-
Chree effect. The periods of the longitudinal and the transverse wave are
essentially constant. Flexural waves are characterized by longer periods
with pronounced anomalous dispersion. These waves are the strongest.
Shear waves have substantially smaller amplitudes. In case of a weak
impact, sufficiently distant vibrographs picked up only the S and J waves.
Because of dispersion, the wave packet of J waves spreads out before
reaching the distant vibrograph. The wave amplitude in the packet is
diminished as a result of the total elastic energy losses (dissipation of
energy into adjoining media, scattering by elastic inhomogeneities in ice,
losses in viscous friction).

The recordings of the sound field in water and of mechanical vibrations
in ice near the impact point constitute a complex interference process.
Besides the four wave types generated in an ince plate excited by a suffi-
ciently brief impact, the noise spectrum in ice and water is also considerably
influenced by the reverberations produced by the scattering of sound energy

by ice inhomogeneities and by the multiple reflection of the pulse from the ice—water and water—bottom interfaces.

Figure 2 shows the oscillograms of sound pressure in water (G) and in ice (VG1) for impact excitation of ice covered by a snow layer 20 cm thick. The snow layer clearly has a damping effect, i. e., part of the kinetic energy is expended in squeezing the fluffy snow layer. The leading edge of the impact pulse is stretched in time, and the impact length becomes $\tau = 0.045$ sec. The spectrum of acoustic waves picked up by the hydrophone is enriched in high-frequency components which are produced by the snow crystals rubbing against one another as snow is squeezed by the impacting object. The intensity of the elastic vibrations of the ice cover diminishes in this case.
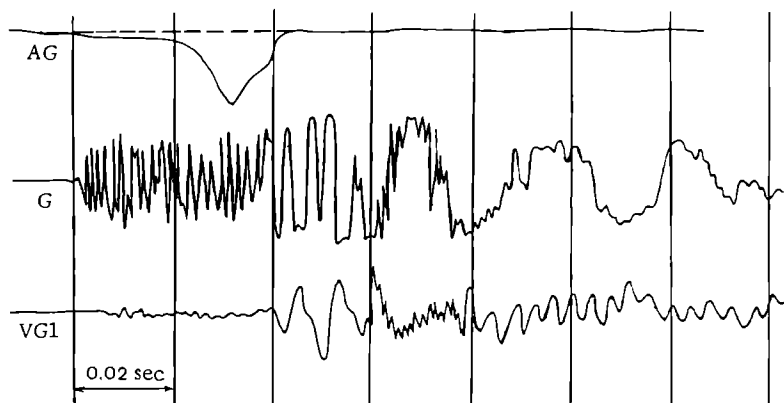
FIGURE 2. Oscillograms of sound pressure in water (G) and in ice (VG1) for impact excitation of ice covered by a snow layer.

The propagation of low-frequency elastic waves (their frequency range as a function of thickness, acoustic energy damping characteristics, etc.) in ice layers of various thicknesses has been considered theoretically by V. N. Krasil'nikov.

The maximum range of propagation /1/ is characteristic of the weakly damped low-frequency flexural waves satisfying the condition $\lambda \geqslant 2\pi h$, where λ is the wavelength in ice cover of thickness h. The penetration depth of a surface wave into water falls between the limits $d \simeq \left(\frac{\lambda}{2\pi} - \frac{\lambda}{4} \right)$. Normal waves, whose propagation velocity in ice is higher than the velocity of sound in the liquid, may also play a certain role over small distances in thick layers. These waves are attenuated through "de-excitation", by radiating their vibrational energy into the liquid medium. Apparently because of the frequency dependence of the damping of elastic waves, the receiving hydrophone located far from the source will mainly pick up noise whose spectrum is rich in low-frequency components.

Let us consider further the effect of an impact pulse on a small floating floe of finite dimensions, whose shape and volume is close to those of ice fragments forming when ice breaks in nature. Table 1 lists the experimental conditions. It is shown in /2/ that elastic bodies under these conditions radiate sound pulses in the form of damped sine oscillations whose frequency is equal to the natural frequency of the excited object.

This conclusion is confirmed by the oscillograms shown in Figures 3 and 4, which correspond to the conditions of experiments 2 and 3 (see table).

TABLE 1.

	No. of experiment		
	1	2	3
Specimen shape	plate	rod	parallelepiped
Size	80 × 201.5 cm	a) 45 × 7× 7 cm b) 23× 7× 7 cm	a) 40× 40× 30 cm b) 40× 40× 15 cm
Mounting, surrounding medium	on supports, air	floating, ocean depth 2 km	floating, lake depth 3.5 m
Excitation method	center-line impact by special reciprocating-action device	hammer impact on one end	central impact by dropping spherical object
Recording technique	electrodynamic pickup, N-700 oscillograph	hydrophone at 35 m depth, N-105 oscillograph	hydrophone at 2 m depth and vibrograph frozen to the specimen
Pulse length, sec	0.3	a) ~0.04 b) ~0.02	a) ~0.06 b) ~0.02
Natural frequency, Hz a) calculated	a) ~55	a) 360—750 700—1500	hydrophone a) 1700—1100, ~1700
b) experimental	b) ~50 flexural waves	b) ~500—1000	vibrograph b) 800—1250

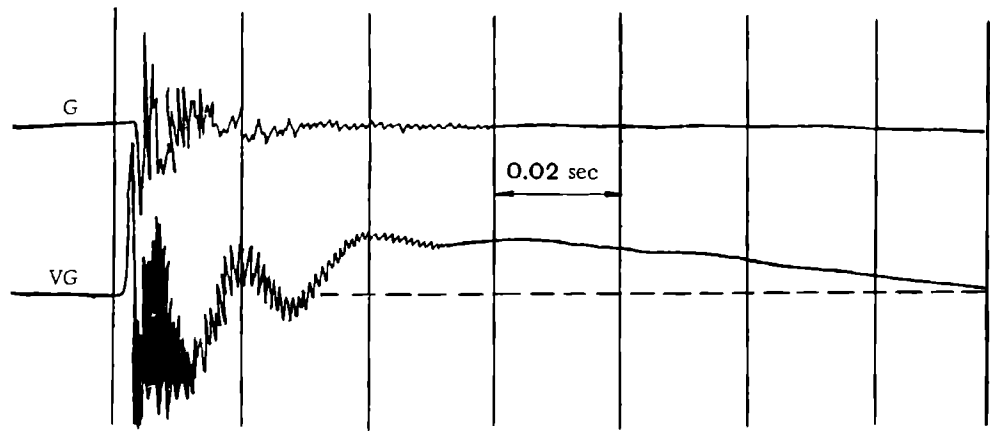Note: The data for experiment No. 1 were borrowed from /3/.

FIGURE 3. Oscillograms of an excited parallelepiped (experiment No. 3).

In experiment 3 (Figure 4), the acceleration gage (VG) picked up float-type oscillations of the specimen (in addition to the natural oscillation

119

modes). The frequency of the float-type oscillations is $\omega_f = \sqrt{\dfrac{\rho_2 g}{\rho_1 h}}$ (where

h is the thickness of the float of density ρ_1, ρ_2 is the density of water, g is the gravitational acceleration), and the results obtained from this formula are fully consistent with the experimental data.

A sufficiently strong impact on ice specimens will radiate aperiodic impact pulses into the water.

Recording the vibrations of the ice cover, we can thus establish the reason for these vibrations, compute the elastic constants of the ice cover, study its mechanical characteristics (damping decrement), and determine the scattering and absorption of elastic energy.
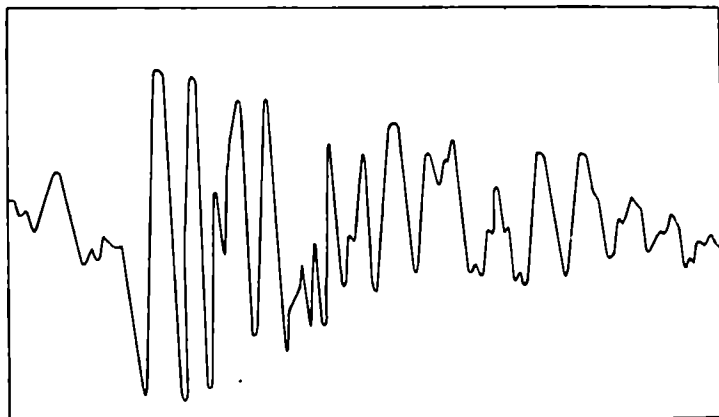
FIGURE 4. Oscillograms of an excited rod 45 cm long ($f = 500$ Hz, $\tau \approx 0.035$ sec).

The results show that dynamic processes in floating ice may be studied by recording the sound waves propagating in ice and in water. The particular recording equipment should be chosen in accordance with the experimental aims.

Bibliography

1. Krasil'nikov, V.N. Rasprostranenie izgibnykh voln (Propagation of Flexural Waves).—LGU. 1960.
2. Gavrilo, V.P. and A.V.Gusev. The Mechanism of the Acoustic Effect Accompanying the Breaking of Ice Rods in a Liquid.— This collection, p. 121.
3. Bogorodskii, V.V. and E.I.Galkin. Issledovanie vnutrennego treniya plastin l'da (Studies of the Internal Friction of Ice Plates).— Akusticheskii Zhurnal, Vol. 12, No. 4. 1966.

V. P. Gavrilo and A. V. Gusev

THE MECHANISM OF THE ACOUSTIC EFFECT
ACCOMPANYING THE BREAKING OF ICE RODS
IN A LIQUID

Mechanical breaking of solids involves release of energy. The amount of energy released depends on the physicomechanical properties of the breaking solid, the surface area of the fragments, and the external stresses applied. Since the energy of elastic wave processes is one of the components of the released breaking energy, a definite relation may be observed between the acoustic energy and the parameters of the breaking solid.

In this paper, we consider the spectral and some other physical characteristics of sound energy generated in a liquid medium as a result of artificial breaking of ice. Ice is treated as a solid with a great variety of physicomechanical properties, which are largely determined by its temperature, structure, and salinity. Investigation of the characteristics of the acoustic field in a liquid generated by breaking ice is of practical importance for the development of remote-control techniques needed to monitor the stressed state of ice and its interaction with the shore or various hydrotechnical structures /3/.

We consider the breaking of an ice rod under water, as a result of the stress produced by Archimedes forces pressing the rod against two supports /1/. When the rod snapped, a hydrophone picked up a characteristic sound pulse. Subsequent recording used a magnetic tape recorder and a loop oscillograph. The rod breaking experiments were carried out for different types of ice using the same procedure.

The first series of experiments was carried out using the low-salinity hummock ice at air temperatures of −5 to −10°C. The following rod dimensions were used: length 30, 60, 80, and 90 cm, cross section 2.5 × 5, 5 × 5, 5 × 10 cm^2. There were 42 rods tested in this series.

The second series used specimens cut from porous summer pack ice at temperatures of −1.0 to −2.0°C. A total of 14 specimens measuring 90 × 6 × 9 cm and 7 specimens measuring 45 × 9 × 6 cm were tested in this series. The breaking force as measured with a dynamometer was found to be 20 − 25 kg.

The third series used sweet ice rods at −4.0 to −6.0°C. A total of 25 specimens measuring 90 × 8 × 8 cm were used; breaking force, 65 − 100 kg.

In all the tests, the rods were broken at a depth of 1 m.

The rod breaking produced damped pulses with durations of a few tens of milliseconds. Figure 1 shows a specimen oscillogram for a rod 90 cm long in the frequency band between 30 and 5000 Hz. The time signals are spaced at 0.02 sec intervals. The oscillograms of the first series of tests

were processed to yield the dependence of pulse duration on the surface area increment of the fragments. The surface area increment was taken equal to the rod cross section area, since in most cases two fragments of roughly equal length were formed. In the range of rod cross sections tested ($S = 10 - 50$ cm^2), the pulse length τ was found to be proportional to S (Figure 2). It follows from the curves that for $S =$ const, τ also depends on rod length l. For larger l, the damped oscillations of the fragments are more sensitive to the adjoined mass of the surrounding medium, whose density is close to ice density.

The oscillograms of the breaking pulses reveal a nonlinear initial section about 0.01 sec long, followed by a fairly clear harmonic component in the form of a damped sine curve with a mean frequency of $100 - 300$ Hz, depending on the length of the original rod.

For more detailed studies of the process of ice breaking by bending, high-speed filming was used, with a camera shooting speed of $0.001 - 0.0003$ sec.

The films were processed to yield the dependence of the recoil speeds of the individual ice fragments on time (Figure 3). The curves were plotted by measuring the displacement ΔL of the ice fragments at intervals of $\Delta t = 0.001$ sec. The velocity was then computed as $\dfrac{\Delta L}{\Delta t}$. As we know that the pressure produced by a moving object in a fluid medium is proportional to the square of the velocity, the time dependence of the pressure $P \sim \rho V^2$ has the form of a shock pulse with peak amplitude reaching tens of thousands of N/m^2. There
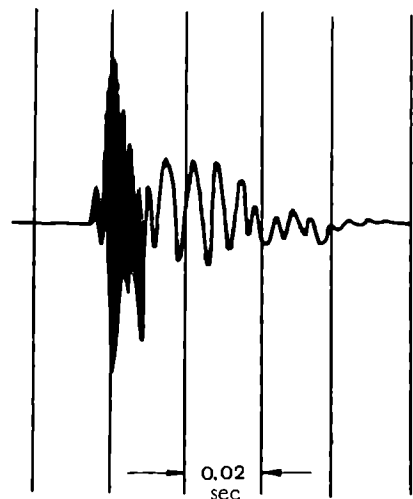

FIGURE 1. An oscillogram of the breaking pulse of a 90 cm long rod.

may be several pulses of this kind when ice breaks, and they may partly overlap. The acoustic shock in this case is apparently also due to the cavitational collapse of the Rayleigh cavity which forms as a result of the sudden fragmentation of a solid object /1/. The mechanism of generation of the short shock pulses thus adequately accounts for the nonlinear character of the initial section of the pulses picked up by the hydrophone.

Inspection of the sound spectra of pulses produced by the breaking of rods of different geometrical dimensions made of ice with different elastic properties shows that the spectral peaks corresponding to rods of various lengths fall at frequencies near 100, 150, 180, and 200 Hz. For shorter lengths, the peaks shift to higher frequencies.

Excitation of solids by impact generates stress waves in the solid. Depending on the degree of acoustic matching with the surrounding medium, these stress waves are radiated from the solid in the form of pulses whose damping is mainly determined by internal friction losses and the effect of the adjoined mass of the medium.

From the differential equation of rod oscillations, we can obtain an expression for the fundamental frequency f_1 of the free transverse oscillations /2/

$$f_1 = \frac{(4.73)^2}{l^2} \sqrt{\frac{EJ}{\mu}},$$

where l is the rod length (cm), E is the elasticity modulus (kg/cm^2), J is the moment of inertia of the rod cross section about a neutral axis perpendicular to the plane of oscillation (cm^4), μ is the mass per unit length of the rod (kg·sec^2/cm^2).
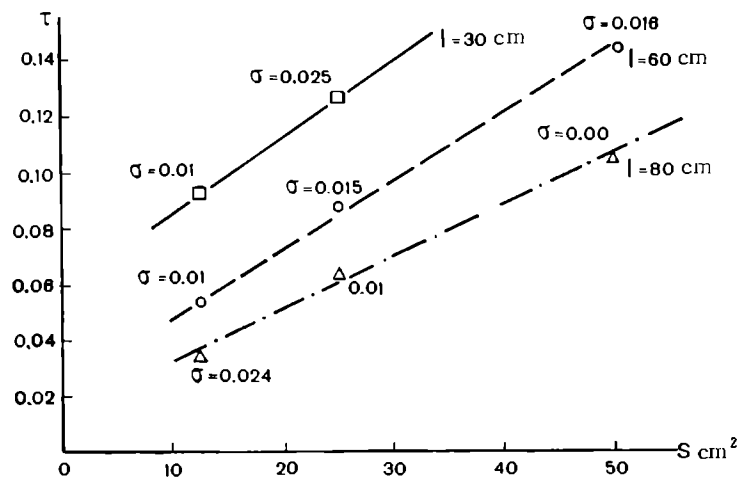

FIGURE 2. Pulse length τ vs. surface area increment S of the breaking specimen; σ is the rms deviation of τ from the mean.
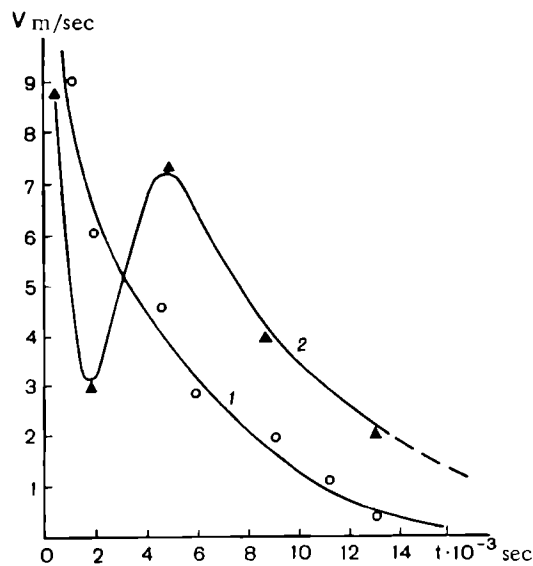

FIGURE 3. Curves of the recoil speeds of the ice fragments vs. time. Curves 1 and 2 correspond to the breaking of two different rods.

123

Calculations of the lower bending modes of rods with appropriate geometrical dimensions fit the maximum frequencies in the experimental spectra and the fundamental frequencies of the damped sine oscillations emerging from the oscillograms of the sound signals (Figure 1).

The spectral levels of the sound pressures produced by breaking sweet ice rods are substantially higher than the spectral levels produced by breaking rods made of mechanically weakened porous summer ice (second series of tests). The difference in intensity around 100 Hz is close to 20 dB. The absolute values of the sound pressure (relative to $2 \cdot 10^{-5} \, N/m^2$) measured by the pickup equipment in the sound range at a distance of 1 m from the breaking rods reach $100 - 130$ dB.

The physico-acoustical characteristics of the simulated process of ice breaking in water (pulse durations and amplitudes, spectral levels and their dependence on physicomechanical properties and geometrical dimensions) obtained in our tests may be used as indicators of the process of ice breaking under natural conditions.

Bibliography

1. Bogorodskii, V. V., V. P. Gavrilo, V. S. Grigor'ev, and A. V. Gusev. Zvukoobrazovanie pri razrushenii l'da v zhidkosti (Acoustic Effect Accompanying Ice Breaking in a Liquid). — Doklad na VI Vsesoyuznoi akusticheskoi konferentsii, Moskva. 1968.
2. Babakov, I. M. Teoriya kolebanii (Theory of Oscillations). — Moskva, Gostekhizdat. 1965.
3. Berdennikov, V. P., A. G. Deryugin, and N. A. Khaminov. Mikrokolebaniya ledyanogo pokrova kak pokazatel' ego napryazhennogo sostoyaniya (Microvibrations of the Ice Cover as Stress Indicators). — Trudy GGI, No. 148. 1967.

V. P. Gavrilo and B. Ya. Gaitskhoki

THE STATISTICS OF AIR INCLUSIONS IN ICE

All forms of natural ice are generally inhomogeneous. Inclusions in ice widely differ in shape, size, and concentration, and also in physical properties. Air inclusions are the commonest in ice. Texture provides a qualitative description of ice with reference to the inclusions it contains; texture is determined by the sum total of the morphological features associated with the various inclusions present. Cherepanov proposed an appropriate textural classification of ice /1/.

A quantitative assessment of the ice inhomogeneity is provided by its density or porosity. Comparison of the density of a given natural ice specimen with the density of monolithic ice free from inclusions gives the volume occupied by the air inclusions per unit weight of the ice specimen; the porosity coefficient is computed as the ratio of the pore volume to specimen volume /2/.

These basic characteristics, however, are insufficient for solving a whole range of problems. For example, in order to determine the damping of sound and electromagnetic waves in ice at wavelengths comparable to the size of the inhomogeneities, we require a quantitative knowledge of the size distribution of inhomogeneities of various shapes. Acoustic and electromagnetic methods of ice probing have become fairly common. To choose the optimum frequency range, we have to know the quantitative distribution characteristics of the inclusions in various ice formations.

The present paper describes the results obtained for the concentration and the size spectrum of air inclusions in two textural varieties of ice. The first variety was fine bubbly ice, with air inclusions mainly in the shape of spherical bubbles. This ice is formed when frazil and snow freeze on the surface of water, and also if the initial ice formation takes place in choppy weather. The second variety included ice with tubular air inclusions. The inclusions in this ice are prominently developed in the vertical direction, in the form of tubes, cylinders, bubble tracks, or capillaries. Ice of this texture occurs on rivers and lakes, and also when snow freezes on the surface of old drifting ice.

Plane-parallel plates of thickness comparable with the cross-sectional extent of the inclusions (about 2 mm) were cut from the corresponding ice specimens. The ice plate was placed under the lens of a photographic enlarger taking large-size film. The image of the ice plate together with a scale was projected onto the film. Contact prints of ice texture photographs were then prepared from the film (Figure 1). Statistical treatment of the ice texture photographs yielded the empirical size distribution of the air inclusions (Figure 2).

In case of spherical bubbles, the sphere radius was chosen as the variable parameter; in case of cylindrical inclusions, the cylinder cross section radius was used. We see from the distribution curves that in fine bubbly ice, bubbles with radii of about $2 \cdot 10^{-2}$ cm are the most probable (Figure 2, curve a). In ice with tubular inclusions, the most probable cylinder radius is $0.3 \cdot 10^{-2}$ cm (Figure 2, curve b). The total number of counted bubbles and cylinders is about 2000 in bubbly ice and over 500 in tubular ice. The concentration of air inclusions in ice can be estimated by counting the number of pulses of various sizes in unit volume, γ_i. The mean count in 1 cm^3 as a function of the bubble radius R_{av} is shown in Figure 3a. For ice with tubular inclusions, the corresponding curve is shown in Figure 3b.
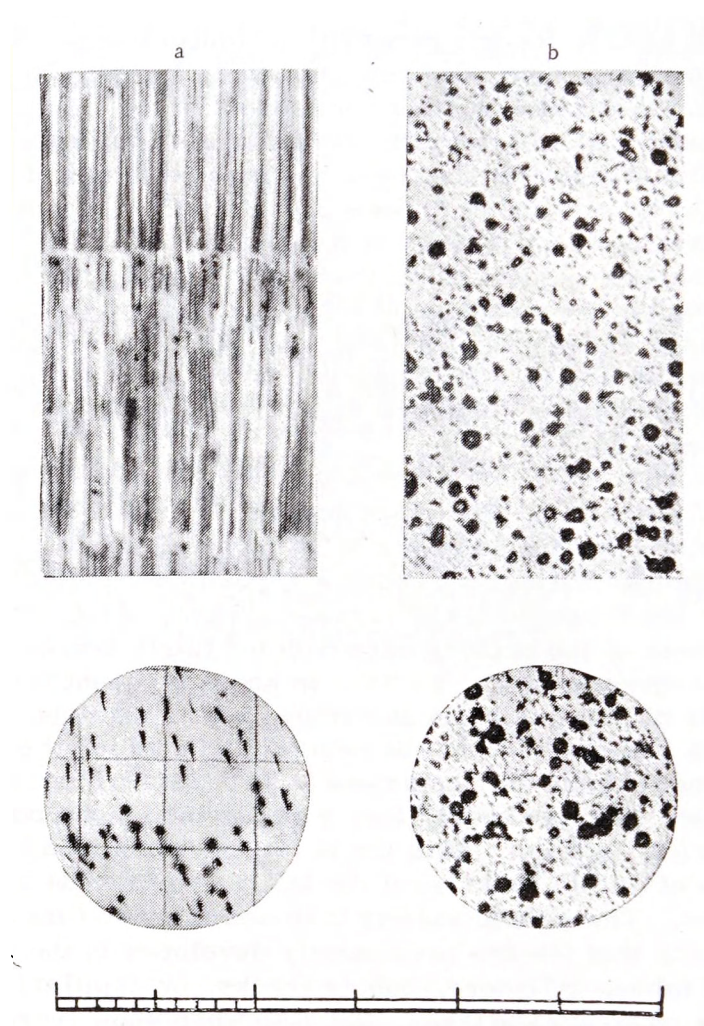

FIGURE 1. Ice texture photographs:

a fine bubbly ice; b ice with tubular inclusions.

The total volume of air inclusions in 1 cm^3 is computed from the equality

$$V = \sum_{i=1}^{n} \frac{4}{3} \pi R_{av}^3 \gamma_i$$

taking $n = 6$. It was found to be close to 30 mm^3, which is about 3.0 % of the total ice volume. The density of monolithic ice is known to be 0.917 g/cm^3. The density of the fine bubbly ice in our tests is thus

$$\rho = 0.917 - 0.030 \cdot 0.917 \simeq 0.875 \text{ g/cm}^3,$$

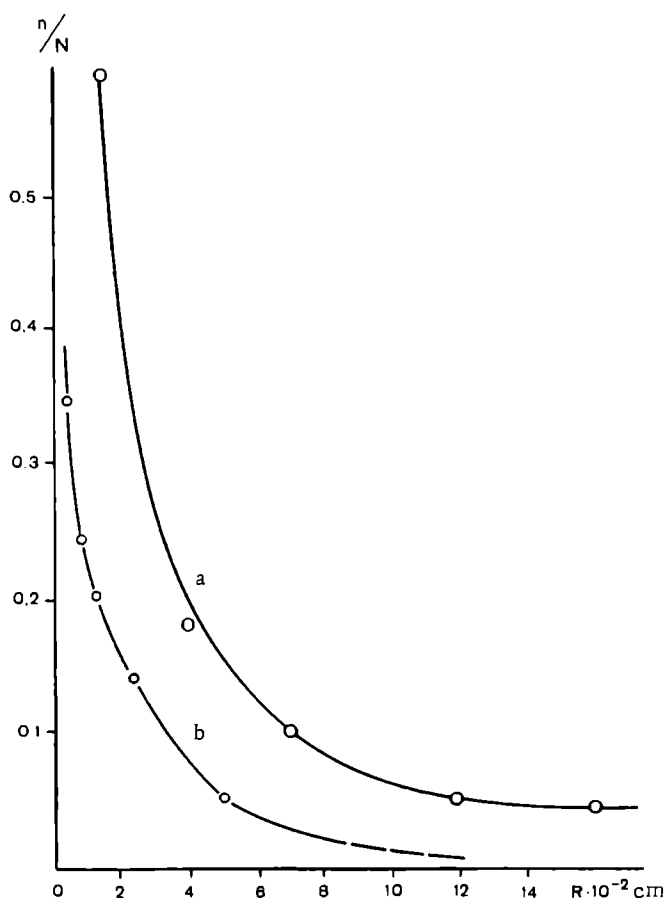which fits the results obtained by hydrostatic weighing for this ice (0.876).

FIGURE 2. Size distribution of air inclusions:

a. fine bubbly ice; b ice with tubular inclusions.

Similar computations for ice with tubular inclusions also give comparable results: 0.899 (computed) and 0.895 (experimental).

We have thus obtained the first tentative results regarding the distribution of air inclusions in two textural ice varieties. Further studies in this direction are evidently needed in order to obtain the corresponding

characteristics for all the other textural varieties of natural ice. The applicability of our technique is confirmed by the adequate fit of the computed and experimental densities for both ice varieties.
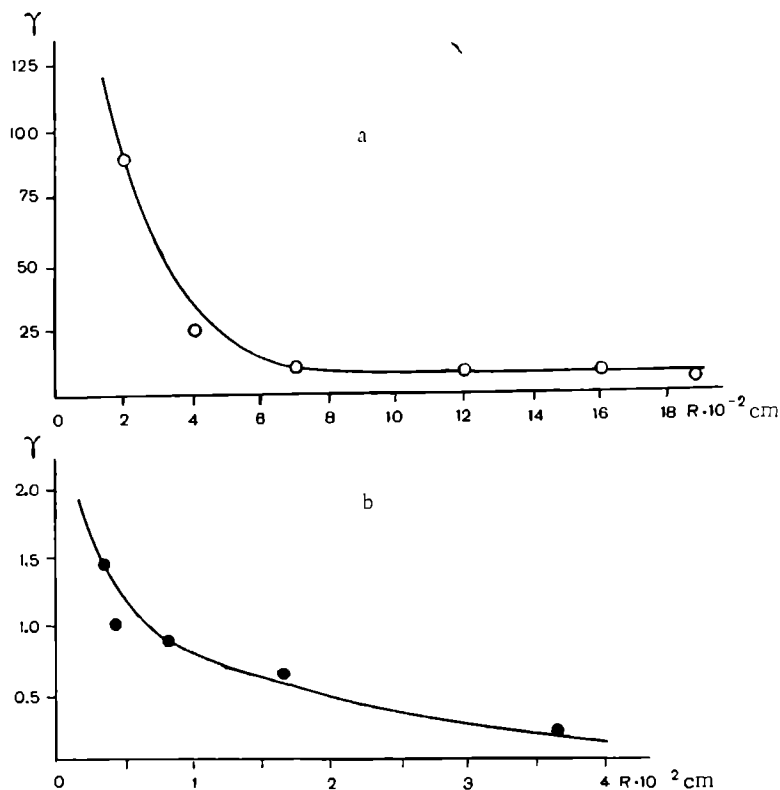

FIGURE 3. Distribution of the number of air inclusions in 1 cm³:

a fine bubbly ice; b ice with tubular inclusions.

The method can be improved by making photometry of the textural photographs. Statistical analysis of the optical densities of the negative obviously may be carried out on a computer. Photometry will appreciably speed up the processing of photographs.

Bibliography

1. Peschanskii, I.S. Ledovedenie i ledotekhnika (Ice Science and Ice Technology). — Leningrad, Izdatel'stvo Morskoi Transport. 1963.
2. Izuchenie mekhanicheskikh i fizicheskikh svoistv l'da (Investigation of the Mechanical and Physical Properties of Ice). A Manual compiled by B. A. Savel'ev. — Moskva, Izdatel'stvo AN SSSR. 1957.

B. Ya. Gaitskhoki and V. A. Spitsyn

SOME RESULTS OF ICE TEMPERATURE MEASURE-
MENTS ON SP-13f DRIFTING STATION

The temperature of the ice cover is one of the principal factors which determine its physicochemical properties. The temperature distribution in ice depends on the temperature conditions at the top and the bottom surfaces of the ice layer, heat capacity and heat conductivity of ice, its density, and thermodynamic and thermochemical processes taking place in its interior.

Systematic round-the-year measurements of the temperature conditions of sea ice in the Central Arctic Basin were carried out on SP-2 drifting station in 1950—1951, SP-4 drifting station in 1956—1957, and SP-5 drifting station in 1955—1956. The results of these measurements show that the temperature conditions of ice are highly variable from year to year. As a result, further measurements of the temperature of the ice cover are needed. Measurements of the temperature distribution inside the ice layer constituted an inseparable component of the general routine implemented at the SP-13f station.

Two thermometric areas were marked on the SP-13f floe: one area corresponded to autumn ice, and the other to pack ice. Characteristic ice areas were selected for measurements, far from the station camp.

The material presented in this article covers the period from May 1965 to April 1966, with a brief interruption associated with changing the camp location.

Three thermometric installations for remote measurements of ice temperature at various depths measured the temperatures to within 0.2°C. The electrothermometric installation comprises a range of electrothermometers, a switch, a measuring bridge, a power source, and connecting cables. The electrical thermometer is made from four wire resistors — two copper and two manganin wires, connected in a bridge. The wires are wound on a core fitted in a sealed cartridge. Each thermometer is connected to the switch by a four-wire cable. The switch is a sealed container with a discrete step selector SI-25/8. The brushes and the lamellae of the selector are palladium-coated to reduce and stabilize the contact resistance. The switch is connected to the measuring panel by a six-wire cable, which delivers the voltage to the thermometer bridge diagonal, takes off the unbalance voltage, and supplies the winding of the step selector. The measuring panel and the power source are mounted in a hut, where all the readings are taken. A distinctive feature of this arrangement is that the unbalanced bridge is completely immersed in the medium whose temperature is to be measured. This largely eliminates the errors associated with the

resistances of the connecting cables. The arrangement also permits extending the scale of the pointer indicator by reversing the direction of the bridge supply current. Before the expedition, all the electrical thermometers and the measuring circuitry were carefully tested at the Central Bureau of Hydrometeorological Instruments.

The electrical thermometers in the test areas were first frozen into autumn ice at depths of 0, 25, 50, 75, 100, 150, and 200 cm and into pack ice at depths of 0, 25, 50, 100, 150, 200, 250, 300, and 385 cm. After the camp had been relocated, the thermometers in the new test areas were frozen into two-year ice at depths of 0, 25, 50, 100, 150, 200, 242 cm and into pack ice at depths of 0, 25, 50, 100, 150, 200, 250, 300, and 350 cm. The ice temperature readings were taken once daily.

The characteristic features of the temperature conditions of the Arctic ice cover are determined by its peculiar position as an interface between two media with markedly different temperature conditions. On one side, the ice is in contact with the water surface, whose temperature is exceptionally stable. It remains constant during the entire year ranging between −1.6 and −1.8°C. It is only during large-scale thaw that the temperature of the subglacial water layer increases to −1.3 or −1.5°C following freshening produced by the influx of thawed water. On the other side the ice layer is in contact with atmospheric air where the temperature conditions are highly variable. Snow distribution over the ice surface is also highly significant, as snow absorbs most of the temperature differential between air and water. Note that nonuniform distribution of snow on the ice surface produces a horizontal temperature gradient in ice.
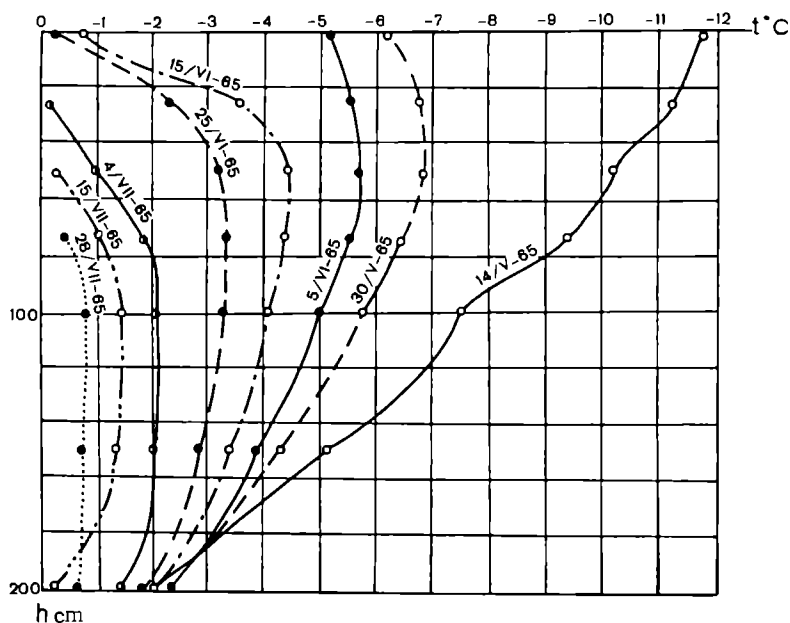

FIGURE 1. Curves of the actual temperature distribution in ice (spring—summer; ice thickness 205 cm).

Observation results reveal the variation in the vertical distribution of the ice temperature during the year and also bring out some general features of the temperature regime. In the initial period of measurements (May — July),
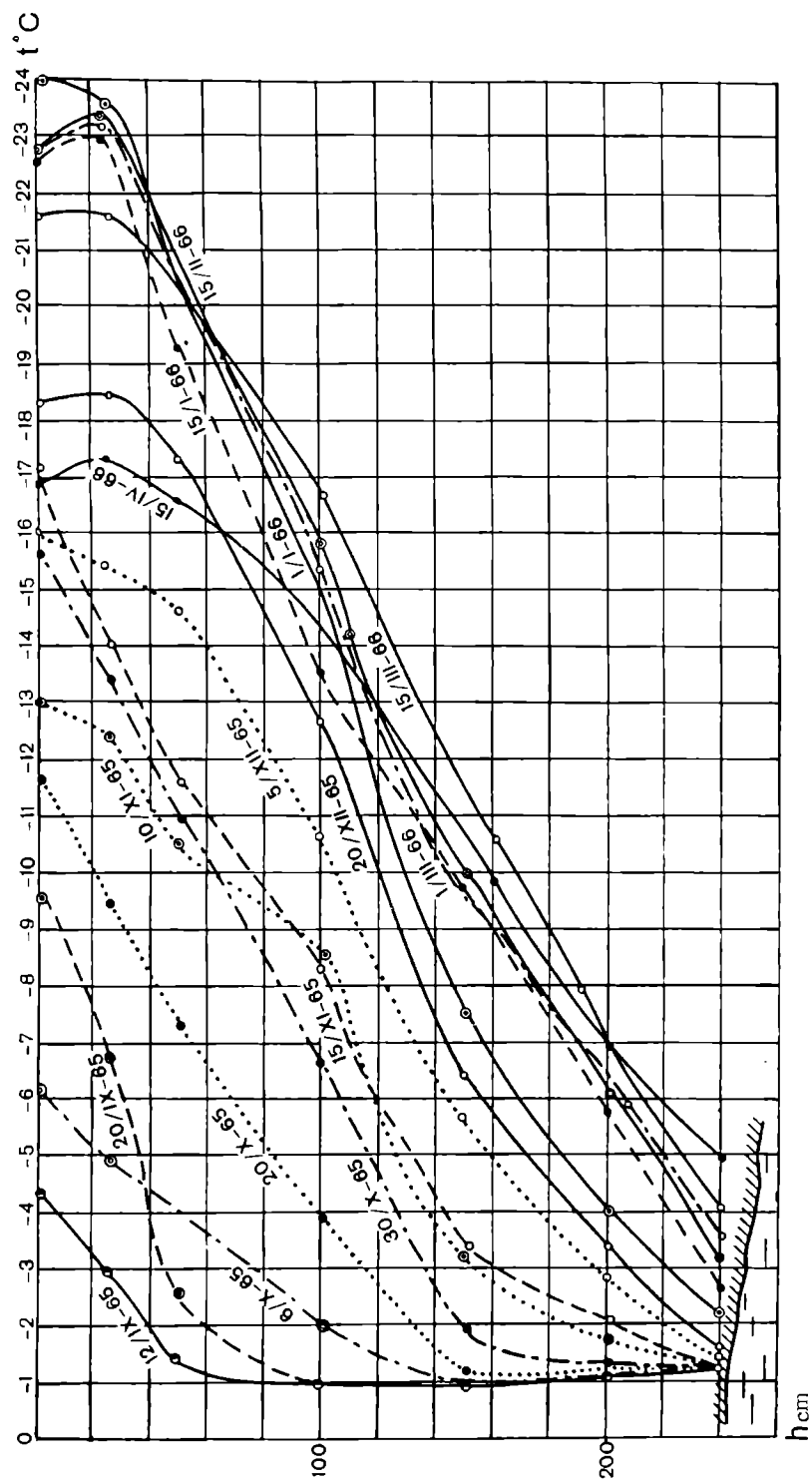
FIGURE 2. Actual distribution of ice temperature (autumn—winter; ice thickness 242 cm).

131

the temperature minimum shifts from the surface into the interior of the ice layer (Figure 1). The vertical temperature gradient in this period is markedly reduced, especially in autumn ice. The drainage of fresh water, on the one hand, and brine migration, on the other, produce in this period a certain instability of temperature near the bottom of the ice layer. In September — January, the top ice cools, and the lower temperatures gradually penetrate into deeper lying layers, the vertical temperature gradient is increased, and the mean ice temperature drops (Figure 2). From the middle of January through April the vertical temperature distribution of ice is stabilized. In April the temperature of the top ice somewhat increases. The best picture of the annual temperature cycle in the interior of the ice layer is provided by the lines of equal temperature based on ten-day averages (Figure 3). The annual temperature cycle of ice clearly shows four distinct periods: the warming period from April through July, the cooling period from September through January, and two periods of stable temperature with the lines almost horizontal (August in summer and February — March in winter). At the end of the warming period, the state of ice is close to isothermal; at the end of the cooling period, the vertical temperature gradient reaches its maximum value. The duration of these periods, however, depends on ice thickness. For thin ice, the cooling and warming periods are relatively short, and the stable temperature periods are correspondingly longer.
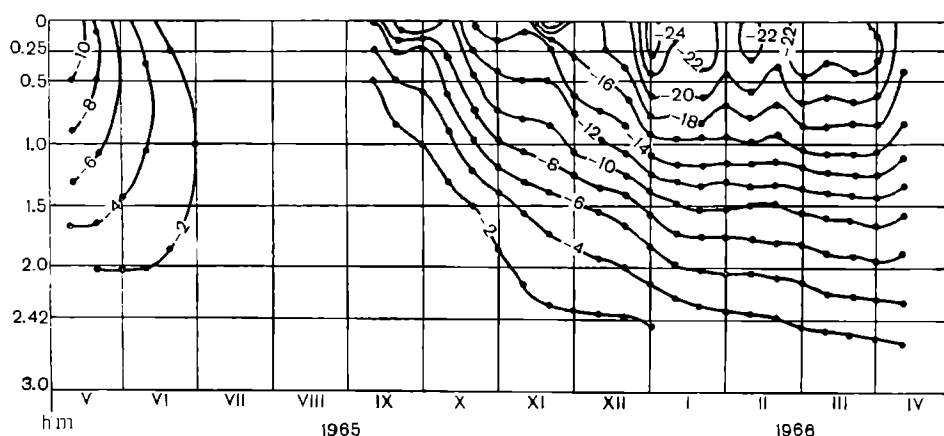

FIGURE 3.   Lines of equal temperature in year-old ice.

The top ice strata are subjected to the largest changes in temperature during the year. The ten-day average temperature at the surface of pack ice varies during the year from −0.4 to −24.4°C, and that of two-year-old ice from −1.2 to −24.3°C (given roughly the same thickness of the snow cover). Minimum temperatures on the surface of ice were observed in January and maximum temperatures in July. Temperature variations with a period of close to one month penetrate to a depth of about 1 m into the ice layer. The lines of equal temperature at greater depths are fairly smooth. Comparison of the temperature chart based on the results of the SP-13f with the results of the SP-2 and SP-4 reveals satisfactory agreement in general features.

V. V. Bogorodskii, V. P. Gavrilo, and A. V. Gusev

NONLINEAR EFFECTS ACCOMPANYING ICE BREAKING IN A LIQUID

Formation of cracks and fissures in ice is accompanied by elastic vibrations which propagate both in the breaking solid and in the surrounding medium. The size of the discontinuities in the ice cover may vary between very wide limits — from small cracks of thermal origin to tremendous crevisses produced by hummocking of large floes. Elastic waves produced by these ice breaking processes have various frequencies depending on the scale of the phenomenon and the physicomechanical properties of ice. They cover the entire frequency range from seismic and flexural waves (observed for vibrations of large ice slabs /1/) to ultrasonic vibrations in the small fragments produced by hummocking.

The spectral characteristics of the sound energy generated by ice breaking in a liquid were considered in /2/, and some physical aspects of the acoustic effect were discussed.

The experimental procedure and the processing are described below. Specimens of certain size and shape were cut from lake or ocean ice; the specimens were then shattered in water by a specially adapted hydraulic press. Acoustic signals generated by breaking ice were picked up by a hydroacoustic receiver. A special depth attachment made it possible to immerse the ice speciment at depths of up to 1.2 m. The specimens were broken at a depth of 1m and right near the surface of water. The elastic properties of the specimens were measured during the experiments, and in some cases the salinity of ice and its structure were also determined.

A number of test cycles were run, using specimens with various physical properties and under various test conditions. The rate of deformation was maintained roughly constant, so that the length of each test (2 — 3 sec) was apparently much less than the relaxation time of any specimen. The breaking load in each experiment was read off the hydraulic press indicator; the strains were not measured. The compression breaking stress σ_b was determined from the measurement results, and this was the parameter used for the comparison of the elastic properties of different specimens.

The breaking pattern of a specimen largely depends on its mounting in the hydraulic press. In case of "lubricated" mounting, when a friction-reducing lubricant layer is interposed between the specimen surface and the press slab, the specimens break by rupture, forming columnar fragments. The system of rupture cracks are parallel to the lateral faces of the specimen. If the specimen is mounted without "lubrication", considerable friction forces develop between the surface of the specimen and the slab. A complex stressed state is set up in the specimen, which then breaks mainly via the growth of cleavage cracks with the formation of two pyramids near the top

133

and the bottom bases. This breaking pattern indicates that shearing stresses predominate in the process. The "no lubricant" mounting was generally used in our tests, as it was thought to provide the best approximation to the ice breaking conditions observed in nature. Ice breaking was explosive.

Ice breaking experiments in water used recorders with a limited passband (40 – 10,000 Hz), so that the total breaking energy could not be measured. Nevertheless, we can try to estimate the absolute energy of the breaking pulses by an indirect method, proceeding from certain assumptions:

1) when the specimen breaks, the entire energy stored in the given volume is converted into the energy of elastic waves;

2) the strength of the material is uniform throughout the specimen volume, being equal to the compression breaking strength σ_b.

The quantity of elastic energy in a specimen of volume V at breaking stress can be computed from the standard expression of the theory of elasticity if Young's modulus E* and the breaking stress σ_b (the hydraulic press gage reading) are known:

$$U_{el} = \left(\frac{\sigma_b^2}{2E}\right) V.$$

According to the first assumption, U_{el} is assumed equal to the energy of the pulse corresponding to complete disintegration of the specimen.

Let us carry out a tentative calculation of U_{el} taking $\sigma_b = 9.81 \cdot 10^7$ dyne/cm^2, $E = 9.81 \cdot 10^{10}$ dyne/cm^2. For specimens with $V \simeq 100$ cm^3, we find

$$U_{el} = \frac{(9.81)^2 \cdot 10^{14}}{2 \cdot 9.81 \cdot 10^{10}} \cdot 10^2 \simeq 0.5 \cdot 10^7 \text{ erg} = 0.5 \text{ joule} = 0.12 \text{ cal.} \quad \text{**}$$

According to the second assumption, the elastic energy per unit volume is

$$u = 5 \cdot 10^4 \text{ erg/cm}^3,$$

i. e., the pressure at the ice – water interface at the time of breaking is $P = 5 \cdot 10^4$ dyne/cm^2 or $P \simeq 170$ dB relative to the absolute zero level ($2 \cdot 10^{-5}$ N/m^2). At a distance of $R = 1$ m from a $5 \times 5 \times 5$ cm^3 cube, the sound pressure in water will reach about 120 dB.

Despite the crudeness of the estimate, the results for the elastic energy are quite reasonable, as is confirmed by a number of experiments for specimens of various volumes.

The plot in Figure 1 is based on experimental data. It gives the mean absolute sound pressure in dB in the 16 – 32,000 Hz band at a distance of 1 m from the source ($\bar{P}_{R=1\,m}$) as a function of the specimen volume. Using the plot, we can estimate the order of magnitude of the sound pressure produced by the breaking of larger specimens. We see from the figure that the calculated pressure of 120 dB for a $5 \times 5 \times 5$ cm^3 corresponds to an experimental pressure of about 135 dB.

Experiments carried out for ice specimens of various elastic properties provided a plot of the absolute sound pressure at a distance of 1 m for $V = $ const as a function of ice strength, represented by the breaking stress σ_b.

---

* Young's modulus E is determined by the method described in /3/.

** Translated to explosives, this energy is released by about 0.13 mg TNT.

Scale-energy characteristics of the sound energy radiated by ice breaking in water were also studied experimentally for rod-shaped specimens. The initial parameters were the cross section S and the length l of the ice rods. Figure 2 shows a family of curves which plot the absolute sound pressure P in dB as a function of the cross section S. We see from the curves that the sound pressure significantly varies as the breaking surface area S increases and is not particularly sensitive to rod length for constant cross section.
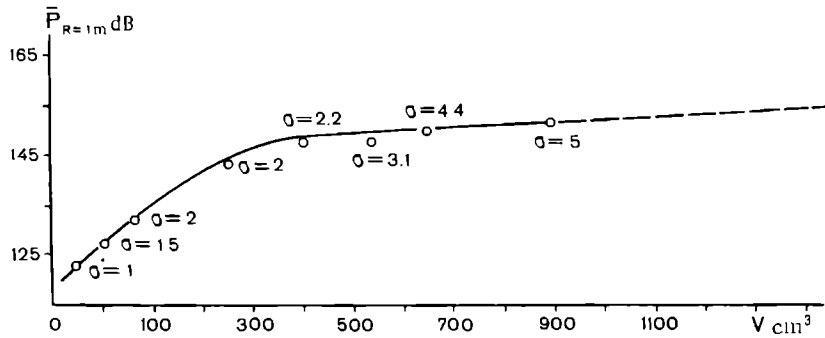

FIGURE 1. Sound pressure $P_{R=1\,m}$ vs. volume V of breaking specimen. σ is the rms deviation.

Another interesting fact is that as the rod length diminishes for $S = \text{const}$, the sound pressure increases, approaching that produced by cube of the same cross section.
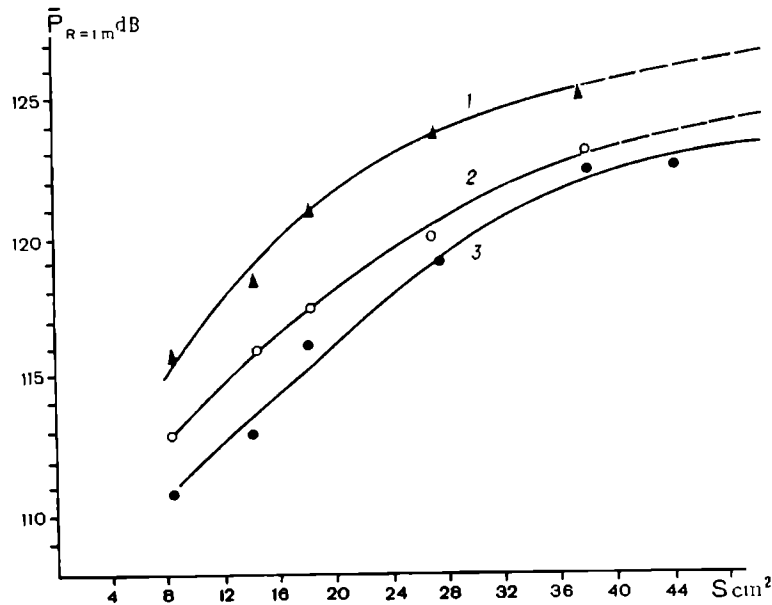

FIGURE 2. Sound pressure in water as a function of the geometrical dimensions of the ice rod (S is the cross section, l the length):

1) $l_1 = 15\,\text{cm}$; 2) $l_2 = 30\,\text{cm}$; 3) $l_3 = 50\,\text{cm}$.

135

The curves in Figure 3 indicate the dependence of the sound pressure on the elastic properties of ice, which are in their turn a function of temperature. Young's modulus E was computed using the propagation velocities of longitudinal (c_l) and transverse (c_t) waves in test specimens measured with an ultrasonic velocity meter UZIS-6 /3/. The measurement results are also shown in Figure 3. We see from the curves that between -2 and $-12°C$ (corresponding to E from 65 to 100 ton/cm^2) the change in sound pressure is insignificant, all other conditions being constant. A more substantial change in sound pressure is observed when breaking rods of weakened elastic characteristics, affected either by the "warm" temperature (around 0°C) or by the weakening of the mechanical structure of ice due to the formation of thermal cracks when low-temperature ice (at -15 to $-20°C$) is immersed in water above freezing.
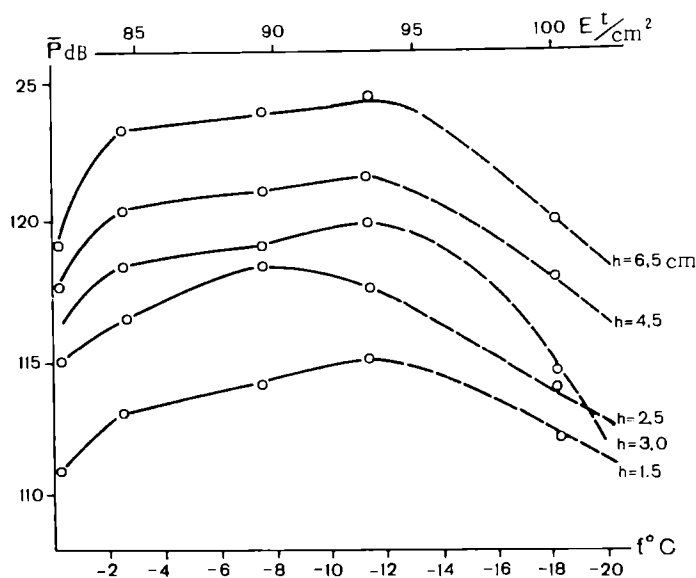

FIGURE 3. Sound pressure produced by breaking rods as a function of temperature. Constant length and width, h is the rod height.

Analysis of the experimental curves leads to the conclusion that the temperature in the relevant range has a relatively insignificant effect on sound pressure. The difference between maximum and minimum pressure for each curve is only about 5 dB.

Analysis of the breaking pulse oscillograms and spectra and examination of high-speed films of the breaking process indicated that the noise effect in water is associated at least with two factors. Besides linear oscillations of the ice fragments, associated with their geometry, ice breaking in water may also produce cavitation /2/.

The low-frequency ascent in the noise spectra (tens and hundreds of Hz) is attributed to the prevalent periodicity of the impact pulses produced by the process of hydrodynamic cavitation which is related to the frequency of the eddies forming as high-speed water jets flow past the ice fragments.

The frequencies were estimated using the relation $f = \mathrm{sh}\,\dfrac{v}{l}$, where sh is the Struhal number, equal to $0.19-0.24$ for a wide range of Reynolds

numbers /4/. The most probable size l of the ice fragments was $1-2$ cm in our experiments; the maximum recoil speeds of the ice fragments were $v \simeq 20$ m/sec (determined by high-speed filming). The high-frequency maximum (at $2-5$ kHz) in these spectra is apparently attributed to the pulsations of the system of air inclusions and vapor-gas caverns with their resonance frequencies. An indirect confirmation of the existence of shock waves generating the cavitation noise is provided by the invariably observed fall-off of the experimental spectra in proportion to the square of the frequency.

In addition to the natural vapor-air inclusions which always occur in water and in ice, Rayleigh cavitation caverns may form during the rapid breaking of ice. The collapse of these cavities is accompanied by generation of shock pulses, which apparently constitute still another physical factor for the development of cavitation effects accompanying ice breaking in water. *

Tentative calculations based on Hooke's law using experimental data on fragment sizes and the elastic constants of ice give $10^{-3}-10^{-2}$ cm for the diameter of the cavities. It was assumed in these calculations that the elastic oscillations of the fragments obey the equations of motion of linear acoustics. Then the breaking of ice rods (length $l = 1-2$ cm, cross sectional area $S \sim 5$ mm^2) in water should produce cavities with equivalent radii of the order of $10^{-2}-10^{-3}$ cm according to the relation $\sigma = \varepsilon E$ (where $\varepsilon = \frac{\Delta l}{l}$ is the relative deformation, $E = 100$ ton/cm^2 is Young's modulus, and $\sigma = 100$ kg/cm^2 is the breaking stress).

The lifetime τ of the cavities of these radii, estimated according to Rayleigh /6/, is $(3-30) \cdot 10^{-5}$ sec for sufficiently high negative pressures. The noise spectrum generated when a single cavity collapses is obtained by expanding the sound shock pulse in a Fourier integral. This noise spectrum has a maximum at a frequency which is approximately equal to the reciprocal of the bubble lifetime $\tau \left(f_{max} \simeq \frac{1}{\tau} \right)$. The spectral density of the acoustic energy decreases at a rate of 6 dB/octave /4/. The spectral maxima at $f \gtrsim 3$ kHz are close to the computed results. Experimentally obtained ice breaking pulses with duration of up to 0.2 sec may be treated as packets of shorter pulses with durations of the order of $(10-30) \cdot 10^{-5}$ sec.

In summing up, we come to the following conclusions.

1. During dynamic breaking of ice in a liquid, hydrodynamic cavitation is accompanied by "breaking cavitation", which is associated with the formation of Rayleigh cavities around breaking ice.

2. A nonlinear dependence of sound pressure on specimen volume was obtained experimentally (as distinct from the theoretical dependence, which predicts proportionality of the elastic energy to volume). The experimental sound pressures (135 dB) are somewhat higher than the calculated pressure (120 dB) for the same volumes. This is apprently due to additional nonlinear noise generation effects associated with the cavitation which accompanies ice breaking in a liquid.

---

* V. S. Grigor'ev called our attention to this fact.

Bibliography

1. Kheisin, D. E. Dinamika ledyanogo pokrova (The Dynamics of the
        Ice Cover). — Leningrad, Gidrometeoizdat. 1967.
2. Bogorodskii, V. V., V. P. Gavrilo, V. S. Grigor'ev, and
        A. V. Gusev. Zvukoobrazovanie pri razrushenii l'da v zhidkosti
        (The Acoustic Effect Accompanying Ice Breaking in a Liquid). —
        Doklad na VI Vsesoyuznoi akusticheskoi konferentsii, Moskva. 1968.
3. Bogorodskii, V. V. Impul'snyi ul'trazvukovoi metod issledovaniya
        fizicheskikh svoistv l'da (A Pulsed Ultrasonic Method of Measuring
        the Physical Properties of Ice). — Trudy seminara po fizike i
        primeneniyu ul'trazvuka, LETI. 1958.
4. Pernik, A. D. Problemy kavitatsii (Problems of Cavitation). —
        Leningrad, Sudpromgiz. 1966.
5. Vinogradov, S. D. Akusticheskie nablyudeniya protsessov razru-
        sheniya gornykh porod (Acoustic Observations of Rock Breaking
        Processes). — Moskva, Izdatel'stvo "Nauka." 1964.
6. Lord Rayleigh. On the Pressure Developed in Liquid during the
        Collapse of a Spherical Cavity. — Phil. Mag., pp. 94 — 98. 1917.

V. P. Gavrilo, A. V. Gusev, and A. P. Polyakov

ACOUSTIC RECORDING OF THE CRITICAL STATE OF STRESS IN ICE

A state of stress develops in ice during formation and breaking of the ice cover and when the ice conditions change on rivers, large water bodies, and seas. Compression of ice is produced during the motion of ice floes in seas and large water bodies, where they are driven by wind and subglacial currents and are subjected to thermal expansion.

One of the factors producing a state of stress in ice and often leading to its eventual breaking is the expansion and contraction of ice due to air temperature fluctuations and variations in insolation.

The temperature conditions of ice are determined by its position as an interface between two media with markedly different temperatures. On one side it is in contact with the water surface, whose temperature is highly stable. On the other side, it is in contact with air whose temperature is highly variable with time. As a result a vertical temperature gradient is set up in ice, even if the air temperature is stable, resulting in relatively high temperatures in the top part of the ice cover. A surface layer of snow also plays an important role in the temperature conditions of ice. Nonuniform surface distribution of the snow cover may produce a horizontal component of the temperature gradient and lead to a more complex stress pattern in the ice layer.

Mechanical measurements of the state of stress in ice meet with certain difficulties associated with the peculiar physicomechanical characteristics of ice /1/. In view of the very low elasticity limit of ice, the relationship between stress and relative strain is variable, depending on time, temperature, and other factors. Elastic deformations of ice may be obscured by its plasticity, so that conversion of the measured relative strains to pressures and stresses is not always feasible. This difficulty can be avoided with the aid of the "unloading method" /2/, but this approach unfortunately is time consuming and fails to produce automatic recording of the parameters. Seismoacoustic measurements were successfully applied to detection of compression processes in ice /1/. However, through fissures in the ice layer or even shallow thermal cracks in the ice surface will enhance the damping of elastic waves propagating from the source to the receiver. This effect will be particularly pronounced at high frequencies, reducing the amplitude of the measured signals for constant source energy.

Before proceeding with a description of the technique and the results of the measurements carried out in nature, let us consider some aspects related to thermophysical processes in ice.

Direct temperature measurements of polar sea ice in various seasons show that the vertical temperature distribution in old pack ice at the

beginning of autumn is virtually uniform, and its temperature is close to the temperature of water. The air temperature in this period is fairly stable and is close to the temperature of ice. The temperature field in ice starts changing as the autumn air temperature falls. Figure 1 plots the temperature variation curves of pack ice, obtained using thermosensors frozen in on various levels.

The vertical temperature distribution in ice for conditions of falling air temperature can be computed from considerations of convective heat exchange with the ambient air /3/. The following initial and boundary conditions are chosen for an ice layer of thickness h:

$$t\big|_{\tau=0}=t_0; \quad -\lambda_i\frac{\partial t}{\partial x}\Big|_{x=0}=a\,(t_\tau-t_{x=0});$$

$$t_\tau=t_0+\vartheta\tau; \quad t\big|_{x=h}=t_0, \tag{1}$$

where t is the temperature, t_0 is the initial temperature of ice, λ_i is the thermal conductivity of ice, W/m·deg, a is the thermal diffusivity of ice, m^2/hr, τ is time, t_τ is the air temperature, ϑ is the rate of change of air temperature.

The problem is solved along similar lines for the case of nonuniform vertical temperature distribution. In general, in the presence of a snow cover of thickness δ_s, the snow layer is replaced by an equivalent ice layer. The substitution is carried out so that the temperature variation in the ice layer is not affected /4/.

The Fourier criterion indicates that the thickness of the equivalent layer should be

$$h_e=\sqrt{\frac{a_i}{a_s}}\,\delta_s, \tag{2}$$

where a_i and a_s are the thermal diffusivities of ice and snow. As it is naturally desirable to operate with air temperatures, rather than the temperatures of the snow (or ice) surface which are not available unless special measurements are made, we have to additionally consider the transitional impedance from air to the snow or ice surface. This can be achieved by introducing a hypothetical layer of thickness

$$h_{ef}=\frac{\lambda_i}{a_a}, \tag{3}$$

where a_a is the heat exchange coefficient between the air and the snow or ice surface.

This is a well-known technique of the theory of heat transfer, and it may be applied only for sufficiently large values of the Biot number, i.e., when

$$B_i=\frac{ha_a}{\lambda_i}>2. \tag{4}$$

In our case, unfortunately, this criterion is not met. Therefore, in general computations of the temperature distribution in ice, the actual ice thickness should be replaced with $H=h+h_e+h_{ef}$ and the initial temperature of the ice cover t_0 should be replaced with the initial air temperature ϑ appropriately adjusted for the rate of change of air temperature ϑ.

In expression (3) it is assumed that the incoming heat flux reaching the snow (ice) surface is entirely supplied by the forced convection of air. The effect of the solar radiation heat flux R and the radiant losses S from the snow surface also can be taken into consideration. To this end, the true air temperature θ should be replaced by an effective temperature defined by the relation

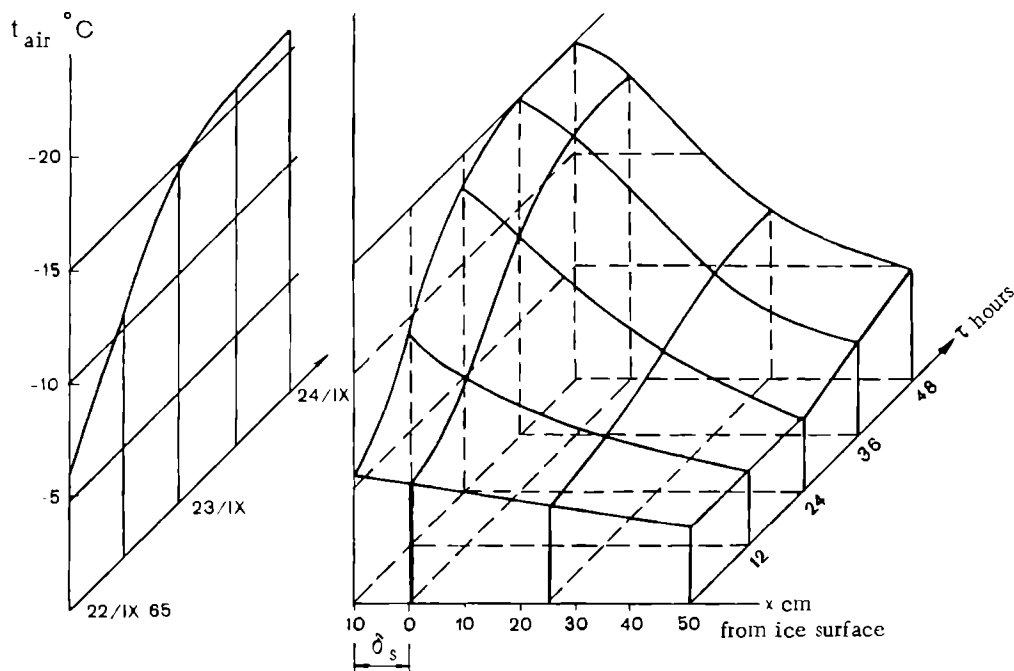$$\theta_{ef} \quad \theta + \frac{R-S}{a_a}. \tag{5}$$

FIGURE 1.

Note that in autumn, when the seasonal cooling of air just begins, the temperature distribution in the ice layer remains uniform. Temperature fluctuations are observed only in the top-most so-called active layer of ice. The bulk of the ice cover retains a constant temperature for a long time despite surface temperature fluctuations and the linear dimensions therefore do not change; the determination of the stresses in the active layer therefore can be reduced to a statically indeterminate problem of temperature stresses in a solid /5/. To simplify the solution, we may consider the problem on one of the coordinate planes only. Assuming that the active layer is isolated from the bulk of the ice cover, the change Δl in layer dimensions, proportional to the applied force, is equal to the temperature increment of linear dimensions Δl_t. Since

$$\Delta l \quad \frac{Pl}{EF} \quad \text{and} \quad \Delta l_t \quad = \alpha l\,(t_2 - t_1), \tag{6}$$

where α is the linear expansion coefficient of ice, we have

$$\frac{Pl}{EF} = \alpha l\,(t_2 - t_1) \quad \text{and} \quad \frac{P}{F} = \sigma = \alpha E\,(t_2 - t_1), \tag{7}$$

i.e., the stress produced by temperature variation in a layer of constant cross section depends only on the elasticity modulus of ice, its linear expansion coefficient, and the temperature difference; it is independent either of the length or the cross-sectional area. Ice is a complex physical object with elastoplastic properties. Its elastoplastic characteristics are highly dependent on temperature and the duration of load application: the lower the ice temperature, the higher the elasticity limit and the wider the range of stresses where Hooke's law applies. This conclusion is borne out by mechanical stress measurements. At −5°C, the linear dependence between stress and strain is observed only up to 8 kg/cm², whereas at −23°C the linear range extends up to 25 kg/cm² /8/. The surface layer of pack ice at temperatures below −5°C thus acts as an elastic material up to the tensile breaking stress. The tensile strength of the surface layer of pack ice is equal to that of sweet ice in a wide range of temperatures /7/, remaining close to 8−12 kg/cm². Young's modulus is also dependent on temperature. Its value for the surface layer of pack ice can be approximated by the following expression /6, 7/:

$$E_t = (52\,000 - 800t)\,\mathrm{kg/cm^2}. \tag{8}$$

Relation (8) is valid at ice temperatures below −3°C.

Thus using the average tensile strength of ice $\sigma = 10\,\mathrm{kg/cm^2}$ and applying relations (7) and (8), we can estimate the temperature differentials producing thermal cracks in the topmost ice layers. For example, at −5°C, the ice surface will crack under thermal stresses when the temperature differential in the layer is around −2.1°C. For an initial temperature of −20°C, cracking occurs as soon as the temperature differential approaches −1.7°C. These calculations are based on $\alpha = 8.5 \cdot 10^{-5}$ for the linear expansion coefficient /8/.

Since long-duration load will produce plastic flow of ice, the relatively gradual seasonal fall of temperature cannot have a marked effect on the phenomenon being considered. We are naturally dealing with sufficiently rapid changes in temperature conditions in the active surface layer. The upper boundary of this layer coincides with the real ice surface, whose temperature according to /4/ is

$$t_h = f_1(\eta_0) = \theta\eta_0 + \vartheta\tau\psi(F_0,\ \eta_0). \tag{9}$$

where τ is the time elapsing since the air temperature began falling;

$$\eta_0 = \frac{h}{H}. \tag{10}$$

$$F_0 = \frac{a_i\tau}{H^2}. \tag{11}$$

The temperature at the lower boundary of the active layer is given by the relation

$$t_k = f_1(\eta_k) = \theta\eta_k + \vartheta\tau\psi(F_0,\ \eta_k). \tag{12}$$

$\psi(F_0,\ \eta_0)$, $\psi(F_0,\ \eta_k)$, η_k are read off the graphs in /4/.

Equations (9) and (12) thus enable us to find the temperature differential between the top and the bottom boundaries of the active layer at any time after the measurements of the air temperature began.

Taking ~ 3 m for the average ice thickness and $\delta_s = 0.10$ m for the snow cover thickness, and remembering that the air—snow heat transfer coefficient is $a_a = 40 \, \text{kcal}/\text{m}^2 \cdot \text{hr} \cdot \text{deg}$, the thermal diffusivity of ice is $a_i = 0.004 \, \text{m}^2/\text{hr}$, the thermal diffusivity of snow is $a_s = 0.002 \, \text{m}^2/\text{hr}$, and the thermal conductivity of ice is $\lambda_i = 2 \, \text{kcal}/\text{m} \cdot \text{hr} \cdot \text{deg}$, we compute the temperature differentials in the active layer for various rates of air cooling and various relative air temperature changes.

Since the thickness of the equivalent snow layer is

$$h_e = \sqrt{\frac{a_i}{a_s}} \, \delta_s = \frac{0.004}{0.002} \cdot 0.1 = 0.14 \text{ m,}$$

and the thickness of the effective layer is

$$h_{ef} = \frac{\lambda_i}{a_s} = \frac{2}{40} = 0.05 \text{ m,}$$

we have

$$H = h + h_e + h_{ef} = 3 + 0.14 + 0.05 = 3.19 \text{ m,}$$
$$\eta_0 = \frac{h}{H} = \frac{3}{3.19} = 0.94.$$

The coefficient η_k, which fixes the lower boundary of the active layer, is equal to $0.85 - 0.9$ when temperature changes by a factor of 2 and more during a period of about 24 hours. Thus if the temperature changes from -5 to $-24°C$ in 12 hrs, we have $\vartheta = -1.6 \, \text{deg} \cdot \text{hr}$, and

after 6 hrs

$$t_h = \vartheta \eta_0 + \vartheta \tau \psi (F_0, \, \eta_0) = -5 \cdot 0.94 - 1.6 \cdot 6 \cdot 0.45 = -9°C,$$

$$t_k = \vartheta \tau_k - \vartheta \tau \psi (F_0, \, \eta_k) = -5 \cdot 0.9 - 1.6 \cdot 6 \cdot 0.12 = -5.7°C;$$

after 12 hrs

$$t_h = -5 \cdot 0.94 - 1.6 \cdot 12 \cdot 0.57 = -4.7 - 10.9 = -15.6°C,$$

$$t_k = -5 \cdot 0.9 - 1.6 \cdot 12 \cdot 0.24 = -4.5 - 4.8 = -9.4°C.$$

Thus, for the given rates of temperature variation, the temperature differential corresponding to cracking stresses is established in the active layer some $3 - 4$ hrs after the temperature begins falling. For a rate of change of 1 deg/hr and a cooling period of 12 hrs, with the temperature falling from -16 to $-28°C$, the stresses reach the breaking point in $6 - 7$ hrs.

Slow temperature variations at a rate of about 0.4 deg/hr reach the breaking strength after as long as $20 - 24$ hrs, assuming that the decrease in temperature persists. Slower variations in temperature apparently cannot produce breaking stresses, since the plastic properties of ice are felt over such long periods of time. Thermal cracking of the ice surface produces elastic vibrations in the ice layer which are transmitted across the ice—water interface and propagate through the water, where they can be picked up with hydrophones.

Subsequent increase of air temperature should not produce surface cracking, since the compressive strength of ice is several times higher than the tensile strength.

Experiments in nature studying the state of stress of ice involve measurements of the sound intensity generated in the subglacial water layer during thermal cracking of the top ice. Two one-hour measurement sessions were carried out daily. The acoustic signals were picked'up by a hydroacoustic channel comprising a sonic frequency receiver, an amplifier, an octave filter with 320 Hz average frequency, and a N-110 recorder. The particular frequency band was selected as being the most characteristic for various forms of ice cracking /9—11/. In parallel with sound measurements, the air temperature was recorded.
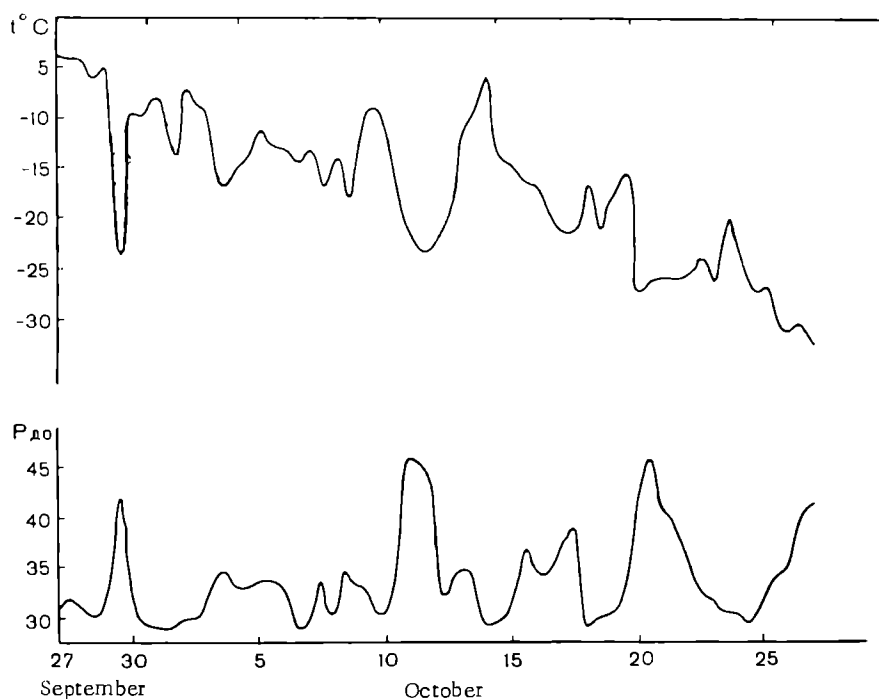

FIGURE 2.

Figure 2 shows curves of air temperature and sound intensity. We see from the curves that reduction of air temperature increases the sound intensity. This effect is observed mainly for abrupt temperature changes during 12—24 hrs. The sound intensity in these cases may exceed the background noise by 16 dB, i. e., by a factor of 6. The measurements mainly provide a qualitative characteristic of the phenomenon. Since crack formation relieves the thermal stresses in ice, the increased noise level naturally does not persist and it drops back to the background level as soon as fairly stable temperature is reached. Increase of air temperature has no effect on the noise level in water. To establish quantitative relations and obtain more detailed information about these effects, observations should be carried out more frequently than twice daily. It is moreover desirable to monitor continuously the temperature conditions of the ice surface, in order to collect preliminary data for establishing a statistical correlation between sound pressure and air temperature variation. The main advantage of listening to ice cracking noises in water is that, regardless of the particular stage of the process and its recurrence, the conditions of signal propagation

do not change, whereas in seismoacoustic measurements signal damping may increase as cracks multiply.

Bibliography

1. Berdennikov, V. P., N. A. Khaminov, and V. A. Shmatkov. Instrumental'noe izuchenie szhatiya ledyanogo pokrova Ozera Baikal (Instrumental Observations of the Compression of the Ice Cover on Lake Baikal).— Trudy GGI, No. 159. 1968.
2. Slobodov, M. A. and V. M. Barkovskii. Burovaya i izmeritel'naya apparatura dlya opredeleniya szhatiya gornykh porod (Boring and Measuring Equipment for Compressive Measurements of Rocks).— Gornye Mashiny i Avtomatika, No. 9. 1967.
3. Pekhovich, A. I. and V. M. Zhidkikh. Raschety teplovogo rezhima tverdykh tel (Calculations of Thermal Conditions of Solids).— Izdatel'stvo Energiya. 1968.
4. Pekhovich, A. I. Raschet statisticheskogo davleniya l'da (Calculation of the Statistical Pressure of Ice).— Izvestiya VNIIG, Vol. 49. 1953.
5. Belyaev, N. M. Soprotivlenie materialov (Strength of Materials).— Izdatel'stvo tekhnicheskoi literatury. 1940.
6. Bogorodskii, V. V. Uprugie kharakteristiki l'da (Elastic Properties of Ice).— Akusticheskii Zhurnal, Vol. 4, No. 1. 1958.
7. Lavrov, V. V. Voprosy fiziki i mekhaniki l'da (Problems of Ice Physics and Mechanics).— Trudy AANII, Vol. 247. 1962.
8. Peschanskii, I. S. Ledovedenie i ledotekhnika (Ice Physics and Ice Technology).— Leningrad, Gidrometeoizdat. 1967.
9. Bogorodskii, V. V., V. P. Gavrilo, V. S. Grigor'ev, and A. V. Gusev. Zvukoobrazovanie pri razrushenii l'da v zhidkosti (Acoustic Effects Accompanying Ice Breaking in a Liquid).— Doklad na VI Vsesoyuznoi akusticheskoi konferentsii, Moskva. 1968.
10. Arabadzhi, V. I. O zvuke voznikayushchem pri droblenii l'da (Acoustic Effects Accompanying Ice Fragmentation).— Akusticheskii Zhurnal, Vol. 14, No. 3. 1968.
11. Milne, A. R., I. H. Ganton, and D. I. Macmillan. Ambient Noise under Sea Ice and Further Measurements of Wind and Temperature Dependence.— IPSA, Vol. 41, No. 42. 1967.

V. V. Bogorodskii, S. A. Smirnov, and V. L. Sinitsyn

SIMULATION OF THE SCATTERING OF UNDERWATER SOUND BY SWEET ICE SPECIMENS IMMERSED IN ARTIFICIAL SEA WATER

The acoustic methods are widely used for probing icebergs, i. e., sweet-ice formations floating on the sea surface. So far, the acoustic method is the only one suitable for observing the submerged part of the iceberg from a distance and for measuring the displacement, the shape, and the mass of the submerged part. Simulation measurements are particularly important in this respect, in view of the very limited opportunities for a comparison of the acoustic results with objective physical characteristics of icebergs. This difficulty is further aggravated by the considerable variety of iceberg shapes, the differences in the conditions of their existence, and the diversity of structure and micro- and mesotopography of the submerged part. Experiments using models /1/ make it possible to alter temperature and other conditions and to correlate the measurement results with the experimental conditions, while keeping the size and shape of ice fragments constant. These model measurements constitute an integral part of iceberg research.

The experiment described in this paper was carried out in July 1966 in the sea-water pool of the AANII using special technique and equipment. The measurements were carried out for spherical, cubic, and cylindrical ice specimens, prepared by freezing fresh water in containers of appropriate shape at $-15°C$.

The spherical specimen was 16 cm in diameter; the ice cube measured $30 \times 30 \times 30$ cm, and the cylindrical specimen was 12 cm in diameter and 35 cm long. The pool ($15 \times 3 \times 2$ m) was filled with artificial sea water containing 35 per mill of NaCl; the ambient temperature was controlled between 0 and $-15°C$.

The ice specimen, sound detector, and acoustic transceiver antenna were attached to two bridges, one of which could be moved along the pool. The rod holding the ice specimen was so designed that the specimen could be rotated in horizontal plane and, if necessary, submerged deeper in water. The sound detector was attached to a rotary bracket and could be fixed at the required depth at a specified angle in the horizontal plane. The rotation angles of the specimen and the detector were read off suitable scales. The transmitting and receiving antenna was held on an arm, so that it could be lowered to a desired depth and the angle of incidence of the acoustic beam could be changed from $-5°$ to $+70°$. The distance between the bridges was fixed in accordance with the required antenna— specimen separation.

The calibration of the reflected signal intensities was carried out using a rigid metallic sphere 4 cm in diameter ($R_0 = 2$ cm) which was suspended next to the specimen.

APPARATUS

The measuring apparatus comprised a control panel and a precision oscilloscope with calibrated sweeps. A timing unit fixed the repetition sequence ($1-10\,\text{Hz}$) and the width of the pulses ($3-50\,\mu\text{sec}$); it also synchronized the oscilloscope. The oscillator generated a radio pulse with recurrence frequency adjustable between 0.8 and 10 MHz; the pulse power of the source was 5 watt. The receiver picked up signals in a 200 kHz band between 0.8 and 10 MHz and had a dynamic range of 66 dB. A receive-send diode switch switched the antenna between the oscillator for sending and the receiver for rest of the time, without using any additional contacts. The oscilloscope screen displayed the time of arrival, the amplitude, and the shape of the reflected signals. To permit observing the signals picked up by the sound detector, the receiver input could be switched to the sound detector.

MODEL COMPUTATIONS

Assuming $200-300\,\text{m}$ to be the commonest vertical dimension of an iceberg, we chose to work with $20-30\,\text{cm}$ specimens and a 1:1000 similarity ratio; obsevation distances of $1-2\,\text{m}$, readily attainable in the pool, thus correspond to distances of $1-2\,\text{km}$ in practice.

Let us determine the magnitude of an echo signal reflected from a target whose properties are characterized by an equivalent radius R_e. The intensity of an echo signal from a target distant r from the antenna is expressed by the equality

$$J = \frac{P_a \gamma R_e^2}{16\pi r^4} \cdot 10^{-0.2\beta r},$$

where P_a is the acoustic power of the transmitted pulse; β is the damping coefficient of sound in sea water, dB/m; and γ is the antenna concentration coefficient.

The echo-signal voltage at the antenna output is

$$U = \nu \frac{R_e}{r^2} \sqrt{\frac{P_a \gamma}{16\pi} \rho c} \cdot 10^{-0.1\beta r},$$

where ν is the antenna sensitivity $\mu\text{V}/\text{bar}$; ρc is the acoustic impedance of sea water.

Calculations show that for $P_a = 1$ watt, $\nu = 50\,\mu\text{V}\cdot\text{m}^2/\text{N}$, $r = 2\,\text{m}$, and $R_e = 0.02\,\text{m}$, a signal/noise ratio of 10 for $U_n = 4\,\mu\text{V}$ is attained at frequencies not exceeding $4-5$ MHz. With allowance for the similarity coefficient of 1:1000, this corresponds to frequencies between 4 and 5 kHz. Further increase of working frequency is limited by power requirements, which are unattainable with antennas $10-20\lambda$ in diameter. Our tests were carried out at 3.6 MHz, which corresponds to simulation of 3.6 kHz frequency. The antenna diameter was 9 mm. The beam width between -3dB points was close to 3°.

INTERACTION OF ICE SPECIMENS WITH
THE ENVIRONMENT

Immersion of sweet ice specimens at −15°C into sea water supercooled to −2°C resulted in the formation of a layer of sea ice crystals on the specimen surface. The layer thickness gradually increased, and the fastest rate of growth of the sea ice crystals was noted in the "waist" area of the specimen, i.e., the part adjoining the air−water interface. The rate of growth of sea ice crystals diminished when the air temperature increased, and no crystals formed at 0°C. The structure of these crystals was typical of the "lacy" young sea ice. Crystals were in the form of isolated platelets with water interlayers between them; they were aligned at right angles to the ice surface. The sea ice crystals are readily chipped off the specimen surface by applying a slight longitudinal force along the surface.

The growth of sea ice crystals on the submerged part of the specimens is attributable to heat transfer between sea water and ambient air through the heat-conducting sweet ice specimen. The growth of crystals thus reaches maximum intensity in the part of the specimen where the resistance to heat conduction is minimum, i.e., in the top area of the submerged part. For air temperatures of 0°C and higher, the specimen surface suffered from thawing; vertically oriented grooves formed on the surface, which probably coincided with the direction of stratification of the water mass around the specimen. In one day, the groove depth reached 3 mm; the spacing between the channels was on the average about 2 cm.

This phenomenon indicates that, depending on the hydrometeorological conditions, noticeable changes may occur in the structure, morphology, and physicomechanical properties of the part of the iceberg near the water surface, leading to certain changes in the acoustic characteristics of the submerged part of the iceberg.

MEASUREMENTS OF SOUND DAMPING IN THE
ARTIFICIAL SEA WATER IN THE POOL

Damping of sound at 3.6 MHz in the sea-water pool was measured by comparing the echo signals from a standard metallic sphere, measured for various antenna−sphere separations ranging from 0.5 to 1.5 m. The sound damping coefficient in water was determined from the equality

$$\beta = \frac{1}{r_2 - r_1} \cdot 20 \log \frac{U_1 r_1}{U_2 r_2} \ \text{dB/m},$$

where U_1 and U_2 are the amplitudes of the signals corresponding to distances r_1 and r_2.

The damping coefficient obtained after averaging of several experimental figures was $\beta = 4.08$ dB/m, which is higher than the theoretical figure $\beta = 2.84$ dB/m /1/. The divergence between experimental and theoretical values may be explained as follows: the pool water at −5°C ambient air temperature contains numerous ice crystals, which introduce additional damping and scattering of acoustic energy. The experimental value of the damping coefficient was used in all further processing.

EQUIVALENT TARGET RADIUS OF ICE SPECIMENS

Measurements of the equivalent target radius of the ice specimens show that it depends on the shape and the foreshortening of the specimen, on whether the specimen floats on the surface or is completely submerged, and also on the degree of its coverage by sea ice crystals.

The equivalent radius of the specimens was measured by recording the echo signals with the specimens submerged to a depth of $20-30$ cm.

By submerging the entire specimen, we eliminated the effect of the water surface on the intensity of the echo signal; specimens without any ice crystals on their surface were used in measurements. For a probing pulse of $\tau = 5\,\mu\text{sec}$, the ice sphere was found to have an equivalent target radius $R_e = 4.5$ cm (average value), whereas the ice cube had $R_e = 5.6$ cm. When the pulse duration was doubled, the echo signal increased in intensity until the spatial duration of the sound pulse became equal to the dimensions of the rayed part of the specimen. Thus for the ice sphere, the equivalent target radius for $\tau = 10\,\mu\text{sec}$ increased to $R_e = 8$ cm. This indicates that the ice sphere should be treated not as a reflector, but rather as a sound scattering center. This conclusion is borne out by the fact that large fluctuations of the echo signal are observed when the sphere is rotated about its vertical axis; these fluctuations are impossible unless the sphere is made up of numerous scattering centers. The variation coefficient of the echo signal from the different specimens reached on the average about 40%.
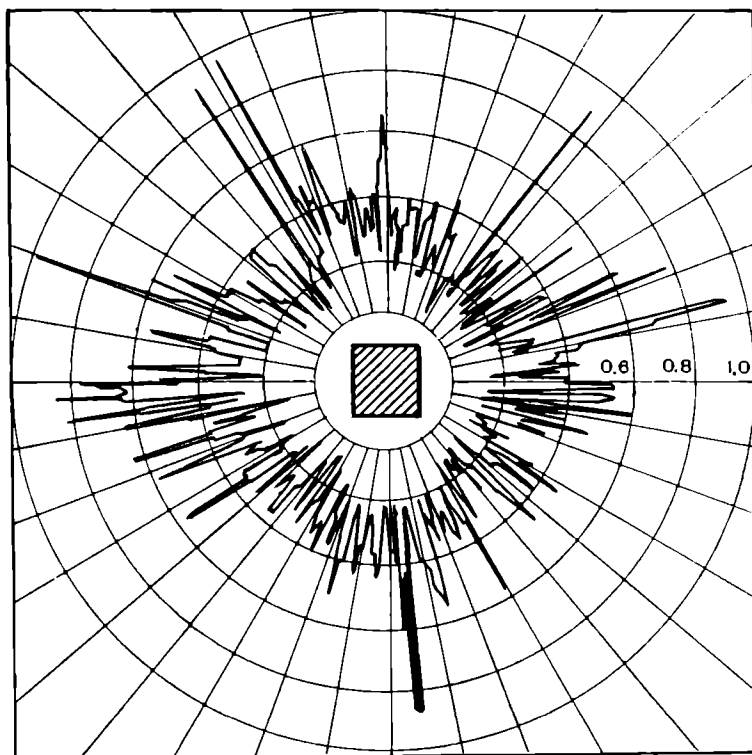

FIGURE 1. Angular diagram of the target intensity for a cubic specimen (linear scale).

For an object of irregular shape, a better characteristic of its reflecting properties is provided by the dependence of the target intensity on the rotation angle of the object. Figure 1 plots this dependence for a cubic specimen. The horizontal axis gives the normalized amplitude of the scattered signal.

The spatial distribution of energy scattered by an ice sphere and by a cubic face is shown in Figures 2 through 4. The intensity of the scattered signals was measured with a sound detector which was moved around the specimen at a distance of 40 cm from the center of the scattering test area. The plots in Figures 2 through 4 point to a diffuse nature of scattering. The dip at angles close to the primary incidence line in Figure 2 is attributed to the shadowing of the ice specimen by the detector. Figures 3 and 4 show that the maximum scattering intensity corresponds to the direction of mirror reflection; for oblique incidence of sound on a plane face of the specimen surface, the specular component is more pronounced. The ratio of the mirror reflection component to the primary incident pulse was used to compute the sound reflection coefficient; the dependence of the pressure reflection coefficient on the angle of incidence is illustrated by the data below:

β	0°	23°	63°
K	0.4	0.64	0.7

The increase of the reflection coefficient at higher incidence angles indicates that a substantial fraction of the acoustic energy incident on the ice surface at small grazing angles undergoes mirror reflection.

We see from the above data that mirror reflection, i.e., the scattered intensity in the direction of mirror reflection, increases as the grazing angle diminishes. Correspondingly, as the grazing angle diminishes, the fraction of diffusely scattered energy diminishes; this is also evident from the smaller scattered intensity in Figure 4 compared to Figure 3. The angular dependence of scattering for both the spherical specimen and the face of the ice cube is close to the Lambertian function. The coexistence of diffuse scattering with mirror scattering accounts for the increase of the equivalent target radius of the specimens when they are lifted closer to the surface of water. The equivalent target radius of the spherical specimen when freely floating on the surface is 1.5 times the equivalent target radius of the same specimen submerged at 30 cm. This effect is due to multiple reflections of sound energy incident on the top part of the specimen between the specimen surface and the water surface; each reflection naturally involves scattering of some of the energy by the ice surface. The effect of the air — water interface on the target intensity of the spherical ice specimen was further illustrated by an additional experiment, in which the top part of a freely floating specimen was covered by a screen. The echo signal intensity in this case dropped not to 1/2, as for the submerged specimen, but to 1/3 — 1/5 of the earlier value. It was further established that the target intensity of specimens overgrown with a 1 — 2 mm layer of sea ice crystals is substantially lower (by a factor of 2 — 2.5). When the sea ice crystals are removed from the surface of the specimen, the original target intensity is restored. Since the general spatial distribution of scattered energy does not change, it seems that sea ice crystals only cause additional damping of the ultrasonic energy incident on the specimen surface, e.g., by viscous absorption or other dissipative mechanisms.
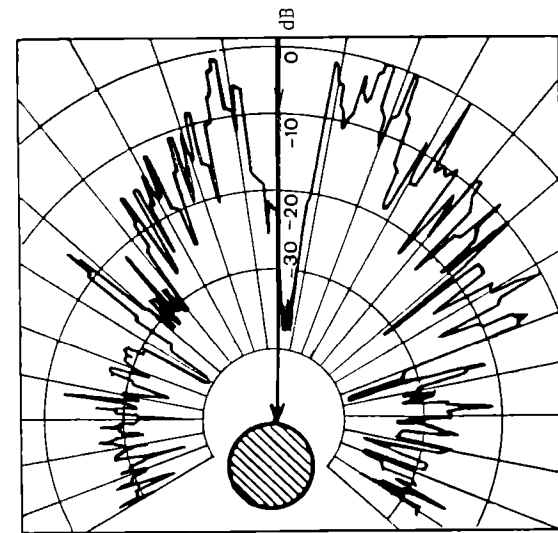
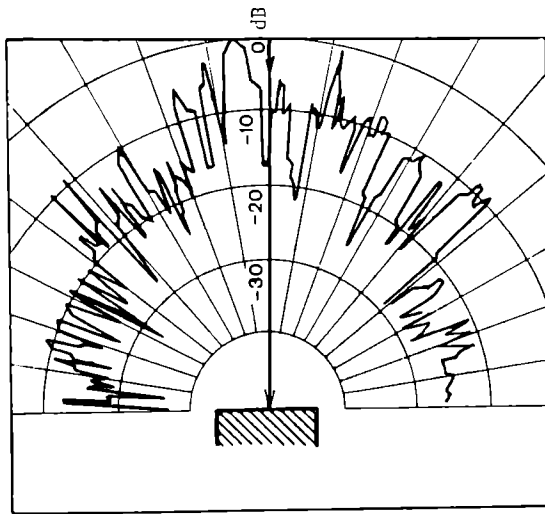FIGURE 2. Scattering diagram of ultrasound by an ice sphere.

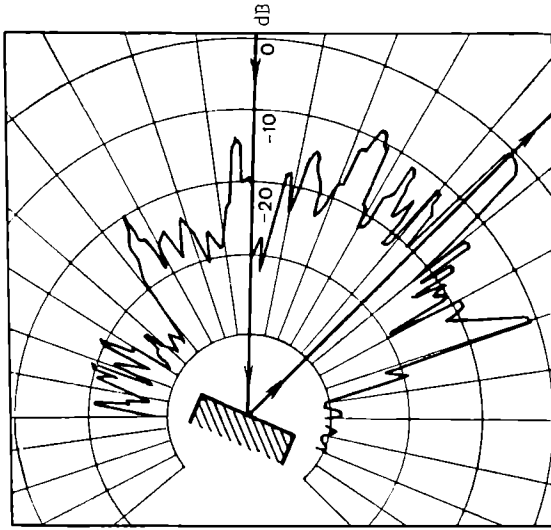FIGURE 3. Scattering diagram of ultrasound by a face of a cubic specimen (normal incidence).

FIGURE 4. Scattering diagram of ultrasound by a face of a cubic specimen (oblique incidence).

151

CONCLUSIONS

1. Model measurements of the propagation of acoustic waves in the sea in the presence of icebergs and the reflection of sound from an iceberg model are described

2. Ice acts as a diffuse scatterer of ultrasound; the scattered radiation, however, contains a mirror reflection component, and the reflection coefficient depends on the angle of incidence: for $\beta = 0 - 63°$, $K = 0.4 - 0.7$; at the same time the back-scattering coefficient for $\beta = 0 - 45°$ decreases by $6 - 12$ dB.

3. The target intensity of a floating ice formation depends on its size and shape and on the state of the sea surface. On the whole, the equivalent target radius is $1.5 - 2$ times less than the geometrical size of the scattering surface.

4. The surface of sweet ice becomes overgrown with sea ice crystals when immersed in artificial sea water if the air and the water are at temperatures below freezing.

5. Echo signals from an iceberg are random variables; signal intensity reveals large fluctuations because of the relative motion of the iceberg and the detector.

Bibliography

1. Barkhatov, A. N. Modelirovanie v gidroakustike (Simulation in Hydroacoustics). — Izdatel'stvo Gor'kovskogo Gosudarstvennogo Universiteta. 1964.
2. Warren Horton, J. Fundamentals of Sonar, 2nd edn. — Annapolis, U. S. Naval Institute. 1959.

V. P. Gavrilo

SUBGLACIAL NOISE ACCOMPANYING FORMATION
OF THERMAL CRACKS IN ICE

Acoustic waves generated by the formation of thermal cracks in ice constitute a characteristic source of natural subglacial noise. The cracks form in the ice cover due to internal stresses produced by large vertical temperature gradients. A large temperature differential in ice is generally observed in winter. Formation of thermal cracks has been often noted, both visually and audibly, by expeditions working on drifting ice floes. Short sound pulses of varying intensity were reported, reminiscent of nearby rifle shots. Thermal cracks in ice fragments of very low temperature which hit warmer water and undergo dynamic deformation constitute another source of noise.

Several experiments in a fresh-water pool were carried out in order to investigate the acoustic characteristics of this ice cracking noise.

The ice cracking pulses were picked up by hydrophones at a distance of about 1 m from the source. Before immersion in water, the ice specimens were left at an air temperature of about $-25°C$. The specimens were plate-shaped, with the dimensions listed in the table.

Series No.	Dimensions $(a \times b \times h)$, cm	Area $(a \times b)$, cm^2	Remark
I	20 × 20 × 10	400	All specimens prepared
II	30 × 30 × 10	900	from sweet ice formed
III	25 × 40 × 6	1000	under natural conditions
IV	9 × 30 × 10	2700	on the surface of the
V	100 × 20 × 10	2000	reservoir
VI	80 × 50 × 10	4000	

The number of pulses exceeding the level of constant background noise reached about 50 — 100 during the recording session (15 — 20 sec). The exact number of cracking shots depended on the surface area of the specimen in contact with the surrounding medium.

The acoustic noise in this effect constitutes a random succession of pulses of various amplitudes and widths /1/. The experimental statistical characteristics of noise, presented in the form of distribution curves of pulse widths, amplitudes, and recurrence frequencies (periods), indicate that pulses of 0.03 — 0.04 sec duration are the most probable. All other conditions being equal (specimen volume, shape, etc.), formation of thermal cracks in ice specimens at progressively lower temperatures produces

progressively shorter noise pulses. No dependence of pulse duration on crack wall area could be established. However, comparison of the pulse amplitudes obtained for one of the specimens indicates that larger thermal cracks produce pulses of larger amplitude. The pulse amplitude distribution closely follows the Rayleigh function.

The pulse recurrence frequencies range from a few Hz to several tens of Hz.

Thermal crack formation is a damped process. For specimens of a given size, thermal cracks will only form during a certain length of time. This length of time in our experiments was around 15 — 25 sec. As any impulse process /1/, subglacial noise associated with thermal crack formation is characterized by the mean pulse density in unit time $\overline{n_0}$. The time variation of this parameter shows that the process of crack formation in larger specimens may take a longer time than the same process in small specimens. The coefficient characterizing the rate of decline of the number of pulses in unit time is about 0.4 pulses per $\sec^2$.

The experimental results indicate that $\overline{n_0}$ is a function of the specimen area (volume) $s(v)$

The pulses generated by thermal cracks are in the form of a damped sine curve. Narrow-band analysis of these pulses yielded the spectral levels of sound pressure. The dashed curves in Figure 1 mark the region where the experimental spectra lie. The solid line is the spectrum obtained by a Fourier transformation of a damped sine pulse with the characteristic parameters of thermal cracks $\alpha = 70$ and $f_0 = 125$ Hz (α is the damping coefficient, f_0 is the recurrence frequency).

We see from these spectra that almost the entire pulse energy is restricted to the range of frequencies up to 1 kHz. Measurements of the subglacial noise from fast ice in the Canadian Archipelago /2/ show that the noise energy generated by thermal cracks in ice is generated at frequencies below 2 kHz.
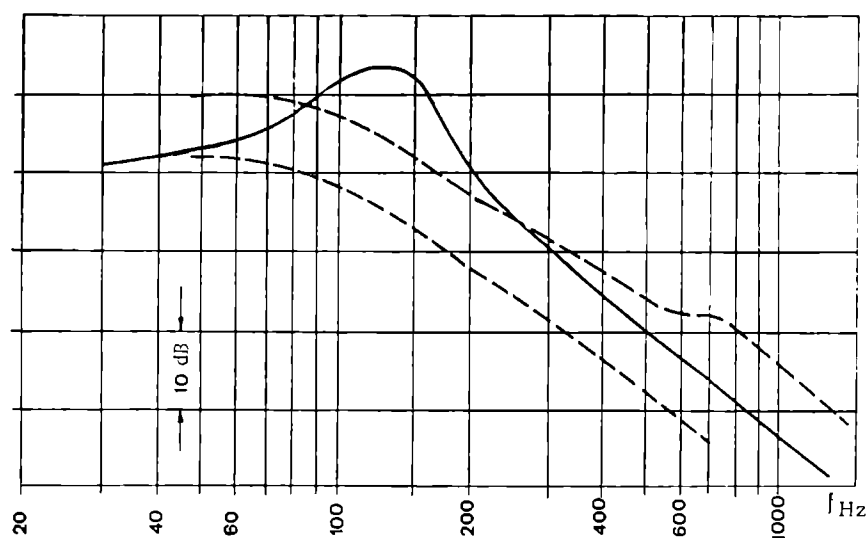

FIGURE 1. Spectra of sound pressure generated in water during thermal crack formation in floating ice.

Our results regarding the physics of the acoustic effect which accompanies ice cracking thus lead to the following conclusions:

1) the statistical properties of subglacial noise generated during thermal crack formation in ice can be described in terms of a random impulsive process;

2) according to experimental data and using the results of /2/, we conclude that the elastic pulses generated by the thermal cracks are best recorded with hydroacoustic equipment at frequencies around 200 − 400 Hz.

Bibliography

1. Levin, B. R.   Teoriya sluchainykh protsessov i ee primenenie v radiotekhnike (Theory of Random Processes and its Application to Radio Engineering). — Moskva, Izdatel'stvo "Sovetskoe Radio." 1969.

2. Ganton, I. H. and A. R. Milne.   Temperature and Wind-Dependent Noise under Midwinter Pack Ice. — i. A. S. A., 38:406 − 411. 1965.

V. V. Bogorodskii, G. V. Trepov, B. A. Fedorov,
and G. P. Khokhlov

RADAR PROBING OF FRESH WATER

The feasibility of radar probing in fresh water was demonstrated in another paper in this collection. The present paper deals with the experimental results of radar probing in a fresh-water reservoir, carried out while this collection was going to press.

Experimental probing was first carried out on Lake Krasnoflotskoe near Leningrad in August 1969. A pulsed radar unit designed at the AANII was used, having the following specifications:

Carrier frequency	45 MHz
Pulse power	1 watt
Pulse duration	0.1 μsec
Pulse repetition frequency	100 kHz
Receiver passband	10 MHz
Indicator — S1—20 oscilloscope	
Receiving and transmitting antennas —half-wave dipoles with metal sheet reflectors	

To prevent attenuation of the radar signal through reflection at the air — water interface, it is recommended to work with submerged antennas. In antennas designed for submerged conditions, the dipole length and the dipole — reflector distance were reduced by a factor of $\sqrt{\varepsilon_w}$ compared to the corresponding dimensions of antennas operating in air (ε_w is the relative permittivity of water, approximately equal to 80 /1/).

In actual experiments, the equipment and the power packs were mounted on a motor launch, and the antennas were moored below the surface of water at a distance of 1.5 m from each other; when the launch moved, it towed the antennas.

The receiving antenna picked up signals reflected from an artificial target and from the bottom of the lake, for various depths up to the maximum, which was 15 m in this case. The bottom constitution was fairly varied in this lake: silt, sand, stone boulders.

A $1.2 \times 1.2 \, m^2$ duralumin sheet was used as the artificial target; during the experiments it was held under the antennas at various depths, ranging from 3 to 15 m. The delay time of the signals reflected from the sheet (t) and the amplitude of the reflected pulses in millimeters on the oscilloscope screen (U) and in decibels relative to the amplitude for 15 m depth (N) * are

* For constant receiving channel gain.

given below for various submergence depths of the sheet in meters (H):

H, m	3	6	9	12	15
t, μsec	0.18	0.32	0.50	0.70	0.86
U, mm	60	40	20	6	3
N, dB	26	22	16	6	0

From the experiments with the artificial target it follows, in particular, that the velocity of radio pulse propagation in water is 33 m/μsec, which corresponds to $\epsilon_w = 81$, in good agreement with the accepted figure. It should be specially stressed that the receiver operated with an ample response margin in these measurements.

Measurements along several traverses across the lake made it possible to perform continuous logging of the bottom by detecting the signal reflected from the bottom and using the propagation velocities from the control experiments with the duralumin sheet. The depth readings obtained by the radar method were verified by direct measurements at several points in the lake. The bottom-reflected signal could be received everywhere in the lake, but over silty bottom areas about 12 m deep the amplitude of the reflected signal was on the average 10 dB less than the amplitude of the signal reflected from the reference sheet at the same depth. Amplitude fluctuations of the signal reflected from silty bottom reached 6 − 10 dB. The amplitude of the signals reflected from stone boulders in some cases exceeded the reference amplitude. Over rocky bottom areas (especially where a pronounced depth differential was noticeable) the amplitude fluctuations exceeded 10 dB.

Using the experimental dependence of the signal attenuation on depth and correcting for the geometrical losses (which go as $1/H^2$ for the sheet), we estimated the attenuation of electromagnetic waves in water due to dielectric losses. It was found to be 1.4 dB/m. Calculations based on laboratory measurements of the electrical parameters of water samples from the same lake gave a similar attenuation value (2 dB/m).

It clearly follows from the preceding that radar probing has great potential in application to fresh-water reservoirs. Electromagnetic fields make it possible to assess the electrical parameters of water and their variation in situ, under any natural conditions. If the water characteristics are known, the shape of the reflected signals provides an indication of the physicomechanical properties of the bottom.

Our results prove the feasibility of depth logging of fresh-water reservoirs and detection and ranging of submerged objects with electromagnetic properties differing from those of water.

Bibliography

1. Bogoroditskii, N. P. and V. V. Pasynkov. Materialy v radio-elektronike (Materials in Radio Electronics). — Moskva, Gosenergoizdat. 1965.